POLITECNICO DI MILANO

FACULTY OF INDUSTRIAL ENGINEERING

DEPARTMENT OF AEROSPACE SCIENCE AND TECHNOLOGY

MASTER COURSE IN SPACE ENGINEERING

OPTIMAL DEFLECTION OF RESONANT NEAR-EARTH OBJECTS USING THE B-PLANE

JULY 25, 2018

Advisor:

Prof. Camilla Colombo

Candidate:

Mathieu Petit

862691

A.A. 2017 - 2018

Table of Contents

List of Figures

List of Tables

Abstract

A very large number of asteroids populates our Solar System; some of these are classified as Near Earth Objects (NEO), celestial bodies whose orbit lies close to or even intersects our planet's, a few of which are believed to pose a potential threat for Earth. Their hazardous nature has caught the eye of both the public and the scientific community and the concern has grown over the past decades, followed by a multitude of studies on the different aspects that characterise this problem.

The most common solution that has been proposed in order to face a potential impact situation is the deflection of incoming asteroids in such a way that their encounter with the Earth is avoided or modified to an extent that it does not pose a threat.

The present dissertation will expand on previous works in this sector, with the aim of defining an optimal deviation strategy with the objective of not only avoiding the incumbent close-encounter, but to also reduce the risk of a future return of the NEO to the Earth. To this purpose, the effect of the deflection will be studied by means of the b-plane, a very powerful reference frame used to characterise an encounter between two celestial bodies, to determine a deflection strategy that will avoid the conditions corresponding to a resonant return of the asteroid to the Earth.

The results presented in this work feature an analytical correlation between the deflection action and the resulting displacement along the axes of the b-plane and the description of optimal deflection techniques based on the aforementioned formulas.

Un grande numero di asteroidi popola il nostro sistema solare; alcuni di questi sono classificati come Near-Earth Objects (NEO), ossia corpi celesti la cui orbita giace vicino o addirittura interseca quella del nostro pianeta, alcuni dei quali sono ritenuti potenzialmente pericolosi per la Terra. La natura pericolosa di questi asteroidi ha attirato l'attenzione del pubblico quanto quella della comunità scientifica e la preoccupazione in merito al rischio dovuto ad un potenziale impatto è cresciuta nell'arco degli ultimi decenni, seguita da una moltitudine di studi sui diversi aspetti che caratterizzano questo problema.

La soluzione più comunemente proposta per far fronte ad una situazione di questo genere è la deflessione dell'orbita dell'asteroide in rotta di collisione con la Terra, in modo tale da evitare completamente l'incontro tra i due corpi celesti o da modificarlo per renderlo innocuo.

La presente tesi continuerà gli studi effettuati in questo settore con lo scopo di definire una strategia di deviazione ottimale mirata non solo ad evitare l'incontro incombente, ma anche a ridurre il rischio di un futuro

ritorno del NEO alla Terra. A questo fine, l'effetto della deflessione sarà analizzato nell'ambito del b-plane, un sistema di riferimento particolarmente interessante per analizzare gli incontri tra due corpi celesti, per determinare le caratteristiche di una deflessione che eviti le condizioni corrispondenti ad un ritorno per risonanza dell'asteroide alla Terra.

Tra i risultati presentati in questo elaborato sono presenti una correlazione analitica tra l'azione di deflessione e il risultante spostamento lungo gli assi del b-plane e la descrizione di strategie di deflessione ottimali basate su tali formule.

1 Introduction

1.1 Background

Asteroids and comets are celestial bodies mainly composed by rocks and ice respectively; while the first have formed in the region of space located between Mars and Jupiter, the latter originated in the farther reaches of our Solar System. It is believed that, around 4.6 billion years ago, the inner rocky planets were formed through an agglomeration of asteroids, whereas the outer gas giants were the result of the agglomeration of comets [1]. While comets feature highly-elliptical orbits that cause their traversal of a large portion of the Solar System, most asteroids still orbit the Sun in the belt located between Mars and Jupiter. It can however happen that some asteroids are nudged from their original position and placed on an orbit passing near the Earth.

These celestial bodies are very interesting from a scientific point of view, as their properties are largely unchanged since the time of the planets' formation. This is the main reason for the scientific missions devoted to the study of both asteroids and comets, such as JAXA's Hayabusa, ESA's Rosetta and NASA's Deep Impact [2].

However, these celestial bodies can present a very significant danger for life on Earth in the form of an impact on the surface of our planet. The objects that could pose such a threat belong to the Near-Earth Object (NEO) family, defined as asteroids and comets with a perihelion distance of less than $1.2\ \mathrm{AU}$ [1]. Most NEOs are asteroids, referred to as Near-Earth Asteroids (NEAs), and a set of subcategories exist to distinguish them: Atiras (NEAs whose orbits are contained within the Earth's, thus featuring a semi-major axis $a < 1\ \mathrm{AU}$ and apohelion distance $r_a < 0.983\ \mathrm{AU}$), Atens (Earth-crossing asteroids with a semi-major axis smaller than our planet's; $a < 1\ \mathrm{AU}$, $r_a > 0.983\ \mathrm{AU}$), Apollos (NEAs featuring an Earth-crossing orbit with a semi-major axis $a > 1\ \mathrm{AU}$ and a perihelion distance $r_p < 1.017\ \mathrm{AU}$) and Amors (asteroids whose orbits are comprised between the Earth's and Mars'; $a > 1\ \mathrm{AU}$, $1.017\ \mathrm{AU} < r_p < 1.3\ \mathrm{AU}$). The most dangerous NEAs also belong to the class of Potentially Hazardous Asteroids (PHAs), which feature a Minimum Orbit Intersection Distance (MOID), the minimum geometric distance between two orbits, of less than $0.05\ \mathrm{AU}$ and an absolute magnitude of 22.0 or brighter [1]. Of the over than 600 000 known asteroids, more than 16 000 are classified as NEOs, of which in turn around 10% fall in the category of PHAs [3]. Despite the seemingly high numbers, the probability of an impact is low, but the damage it could produce is very significant [4].

Another aspect of this threat is represented by the possibility of a NEO which has already flown close to the Earth to return to our planets a few years down the line. This phenomenon is known as a resonant return and is determined by the possibility of a first close approach to deviate a small body's orbit in such a way that the new orbit will lead to a future encounter. A notable case of this effect is represented by asteroid 2010 RF_{12}, a PHA

discovered during a close approach in 2010, which will return to our planet several times in the future. The closest of these encounters is predicted around the 6th of September 2095, where it will approach the Earth as close as $1.209 \cdot 10^{-4}$ AU [5].

The concern generated by this problem has raised the interest of the major space agencies, which have established units devoted to the observation of NEOs, as well as proposing strategies to face an imminent impact, were it to be expected. Furthermore, international efforts have come to exist, involving both the cooperation between the agencies themselves and the institution of the UN-mandated Space Mission Planning Advisory Group (SMPAG) [6], in order to coordinate the work aimed at preparing for such a threat.

On a final note about the background of the problem, man-made objects could also pose an impact-related threat for Earth. This is especially true for spacecraft and launchers used for interplanetary missions, which could involuntarily be inserted on an orbit coming back to Earth or impacting another planet. This has been the case for the third stage of Apollo 12 and object WT1190F, believed to belong to another lunar exploration mission [7].

1.2 Deflection Methodologies

Several techniques for the deflection of potentially hazardous asteroids have been conceived throughout the years and they can be catalogued depending on the type of interaction they have with the asteroid. The first category is based around a single impulsive change in the linear momentum of the asteroid, which can be achieved through the likes of a kinetic or nuclear impactor. A second class of methods features multiple impulsive changes in the NEO's linear momentum, usually obtained with a mass driver. The last two categories trade the impulsive nature of the first two for a continuous low thrust; the first of these actively produces the thrust, through techniques such as attached propulsion, while the last passively deflects the asteroid by means of induced thermo-optical changes of the celestial body's surface [8].

The simplest technology that can be applied to deflect an asteroid is the use of a kinetic impactor. It involves hitting the NEO with a spacecraft at a high relative speed. The nuclear impactor features the same goal of an impulsive momentum change as the kinetic one, but aims to achieve it through a nuclear explosion instead of through an impact. The explosion can be produced at close distance from the asteroid, on its surface or underneath it with differences in mass ejection and robustness of the deviation effect. These technologies can be aimed at either deviating the asteroid or at breaking it up into smaller pieces. This last eventuality could however not be sufficient to avoid the impact and could even produce more damage than what would have been caused if the asteroid was not fragmented [8]. Furthermore, the use of nuclear explosions in space is banned by the Outer Space Treaty [9].

Mass drivers are based on the idea of extracting material from a NEO and ejecting it using resources from the asteroid surface itself as propellant to produce a change in the asteroid's momentum. Similarly, in-situ low-thrust propulsion systems aim at changing the celestial body's trajectory by means of engines attached to the NEO's surface. Other low-thrust systems are the gravity tractor, consisting of a spacecraft hovering close to the asteroid to slowly pull it away from its nominal trajectory, the modification of the object's albedo through a coating of its surface [10], ablation of the NEO's surface by means of a laser or the focusing of the Sun's radiation through a system of mirrors and lenses, in order to produce thrust through the ejection of vapours from the surface [11] and ion beaming, a technique based on displacing an asteroid by mean of a quasi-neutral ion beam generated by a nearby spacecraft [12]. These classes of techniques are generally more complex to implement and the deflection thrust they produce is smaller compared to the impulsive alternatives, especially for large asteroids, thus requiring a longer active time window [8].

For the scope of the present dissertation, only the kinetic impactor will be considered as the applicable deflection technique in awe of its relative simplicity and ease of correlation with the obtained deflection. This is in line with the SMPAG's statement defining the kinetic impactor as the most viable deflection technique at this stage [13]. Furthermore, its modelling will be carried out in a simplified manner, neglecting effects due to momentum dissipation and non-uniform composition of the target, as well as the effect of a possibly uneven geometry paired with a rotation of the body.

1.3 Current and Planned Missions

The first mission involving the deflection of an asteroid through kinetic impact is a joint effort of NASA and ESA in the form of the Asteroid Impact & Deflection Assessment Mission (AIDA), currently under development [14]. This mission will be composed by two independent spacecraft which will be sent to the binary asteroid Didymos. The NASA Double Asteroid Redirection Test (DART) mission will launch between December 2020 and May 2021 to impact Didymoon, Didymos' secondary body, in October 2022, at the time of the NEO's close approach with the Earth [15]. ESA's Asteroid Impact Mission (AIM) is scheduled for launch in October 2020 and will be tasked with closely observing DART's impact with the asteroid. Given the relative proximity of the Earth to the NEO at the time of the impact, useful observation will be possible through ground-based telescopes as well. AIM will analyse the structure of the small body after the fly-by to compare it with the pre-encounter conditions, as well as observing the ejecta plume caused by the impact and the result of the deflection on the asteroid's orbit. This data will allow us to better understand and model this technique in case it were needed for a real threat scenario [14]. The AIDA mission replaced a previous prototype mission under development at ESA, the Don Quijote Mission, which also featured two spacecraft: an impactor and and orbiter [16].

1.4 Close Encounters and Resonant Returns

The nature of the close encounters of minor bodies with the planets is key in understanding the current configuration of the Solar System. It is in fact responsible for the accumulation of planetesimals in the early stages of the system's formation and still plays an important role in shaping the surface of all the celestial bodies with a solid outer layer [17].

Given the relevance of this phenomenon in the motion of objects in space, several studies have been carried out throughout the years to better characterise the fly-bys of small celestial bodies. Amongst the first is Tisserand's criterion, dating back to 1889, used to identify a comet after a close approach, which was rendered difficult because of the rapid change in its orbital parameters [18]. The result obtained by the French astronomer is still widely used today in the framework of the Circular Restricted Three-Body Problem (CR3BP). A second and more recent study is the one carried-out by Öpik between 1951 and 1976, aimed at predicting post-encounter properties of small bodies featuring a close approach of a planet. Even though Öpik's modelling of the gravitational forces involved in the fly-by is limited to a two-body Keplerian motion, the results that can be obtained through its application are still relevant in the modern age [17] [19]. Finally, the idea of resonant returns, the property of a fly-by to insert the small body on an orbit leading back to the planet, born in Lexell and Le Verrier's work on Lexell's comet at the end of the 18th century, was initially used for spacecraft navigation purposes in the '70s and made its return to close-approach applications in the late '90s [19]. All of these studies contribute to the basis upon which this thesis work is built.

1.5 Thesis Objectives

This thesis work is aimed at finding a deflection strategy for incoming asteroids that will not be limited to the deflection of the hazardous NEO in the scope of the immediate encounter, but will instead look at providing a technique to reduce the likelihood of an impact of the asteroid on the Earth in its future encounters with our planet. The desired displacement of the asteroid will be sought on the b-plane (also known as the "target plane"), a reference system often used to characterise an encounter between two bodies in space, which has been the subject of extensive research, since its introduction by E. J. Öpik in 1951; most notably by Carusi et al. [17], Milani et al. [20] and Valsecchi et al. [19], who have started to study and expand the original theory in the late '90s. The objective of the present dissertation is to expand on previous work taking advantage of the b-plane, such as Bourdoux's [21] and Vasile and Colombo's [22], to not simply maximise the distance of the NEO from the Earth on the b-plane, but to define specific deflection strategies in order to avoid resonance conditions caused by the asteroid's flyby of our planet. To this purpose, the determination of an analytical technique to correlate the

required deviation on the b-plane with the deflection action necessary to obtain it would go a long way towards providing a convenient procedure to determine the optimal deviation strategy.

1.6 Dissertation Structure

The present final report is organised as follows: the first chapter will concern the b-plane, as it represents the foundation of the work, the underlying theory will be detailed and some results will be displayed to analyse its crucial properties for the later stages. This section will be followed by a chapter on the modelling of the deviation action considered for the problem, which will in turn feature a description of the formulation and some important results obtained in the framework of the optimal deflection strategy. Each of these chapters contains the theory applied to each case, the new theory and algorithms developed for each section and the results that have been obtained in the framework of each subject. Finally, a section containing the results of this work analysing the problem as a whole will precede the conclusion, featuring some considerations on what has been accomplished so far and what could be the future developments of the presented dissertation. The main contributions of the present dissertation are the determination of an analytical theory connecting the displacement along the b-plane axes at the encounter with the deflection action performed on the asteroid, the description of analytical techniques to maximise the deviation along the b-plane axes based on the aforementioned correlation and the application of an optimal deflection technique aimed at reducing the probability of a resonant return to the 2095 encounter of 2010 RF_{12} with the Earth.

2 The B-Plane

This chapter is aimed at describing the b-plane and its properties. As it has been stated in the introduction, the b-plane is a very powerful tool to characterise fly-bys; the qualities that determine its advantages will be illustrated in section 2.2, following the derivation of the formulas upon which it is based. Some considerations on the properties of this reference frame will then precede a section containing the obtained results inherent to resonant returns, as determined through the b-plane itself.

2.1 Fly-by Models

Every time an object in the Solar System, such as a comet or an asteroid, passes close to a planet, its heliocentric trajectory is modified. This is due to the gravitational pull of the planet playing an important role in determining the small body's orbit when performing a fly-by. In fact, a region of space in which the attraction of a body dominates over the one of the Sun can be determined; it is known as the Sphere of Influence (SOI).

The present section details some general properties concerning the fly-by of a small body around a planet. The formulas featured in this chapter will be used throughout the following steps of this dissertation to obtain some of the equations defining the b-plane.

2.1.1 Restricted Two-Body Problem Fly-by Model

Considering the classic two-body problem relation

$$r = \frac{p}{1 + e\cos\theta}$$

which expresses the distance of the minor body with respect to the major one in the perifocal reference frame, we can compute the direction of the asymptotes of a hyperbolic flyby with respect to the perigee direction as

$$\theta_\infty = \arccos\left(-\frac{1}{e}\right)$$

where r is the distance between the two bodies, p and e are the hyperbolic orbit's semi-latum rectum and eccentricity respectively and θ is the true anomaly (θ_∞ is its value when the distance goes to infinity).

The other involved angles will therefore be

$$\beta = \pi - \theta_\infty$$

$$\delta = 2\theta_\infty - \pi = \arcsin\left(\frac{1}{e}\right)$$

δ is the turn angle, which provides information circa the degree of rotation during the fly-by, whereas β is the complementary angle to θ_∞ [23].

From Figure 2.1, which expresses the fly-by geometry, we can derive

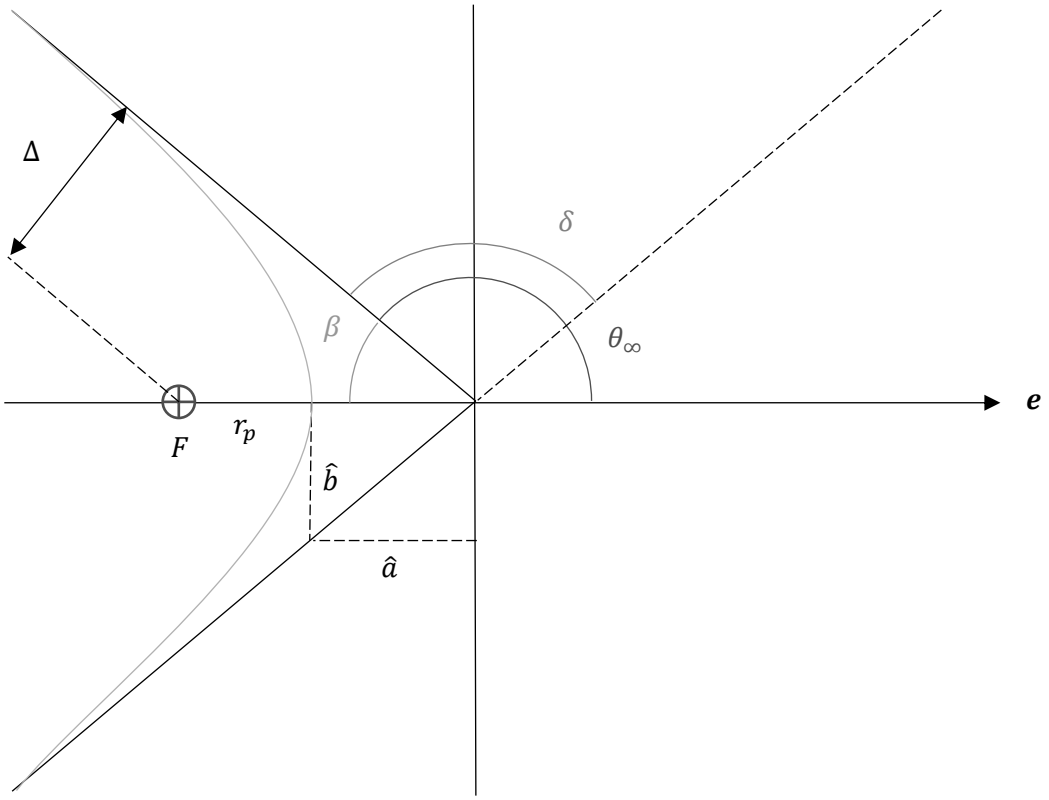

Figure 2.1: Fly-by geometry.

$$\hat{b} = \hat{a} \tan \beta$$

$$\Delta = \left(r_p + \hat{a}\right) \sin \beta$$

By introducing the formulation of β derived above, we obtain the impact parameter (also known as the aiming radius) [18] as

$$\hat{b} = \Delta = \hat{a}\sqrt{e^2 - 1}$$

Equation 2.1

where $\hat{a}$ is the semi-major axis of the hyperbola after a sign change and r_p is the pericentre radius.

The energy conservation equation applied for the distance going to infinity can be used to obtain the modulus of the planetocentric velocity of an object leaving a planet on a hyperbolic trajectory

$$U = \sqrt{\frac{\mu_P}{\hat{a}}}$$

Equation 2.2

where μ_P is the gravitational constant of the planet.

2.1.2 Restricted Three-Body Problem Fly-by Model

The restricted three-body problem features two main bodies of masses m_1 and m_2 rotating around the centre of mass of the system with a fixed angular velocity. The motion of a third body characterised by an infinitesimal mass around the barycentre can be studied in this framework to obtain some very useful results [18].

2.1.2.1 *Tisserand's Criterion*

Tisserand's criterion identifies a quantity of a body which is a constant function in the three-body problem and therefore does not vary in the case of a flyby. This property is very useful when trying to determine whether a Near-Earth Object (NEO) that is being observed is actually the same object that has been seen during a previous close approach with the Earth [18]. Furthermore, it also allows to write a convenient formula for the planetocentric velocity of an object at the moment of its encounter with a planet's sphere of influence, as will be shown in the next paragraph.

2.1.2.1.1 Kinematics

In the framework of the restricted three-body problem, we can define

$$\boldsymbol{r}^* = \boldsymbol{R}\boldsymbol{r}$$

$$\boldsymbol{v}^* = \boldsymbol{R}\boldsymbol{v}$$

$$\boldsymbol{a}^* = \boldsymbol{R}\boldsymbol{a}$$

where $\boldsymbol{r}$, $\boldsymbol{v}$ and $\boldsymbol{a}$ are the position, velocity and acceleration vectors with respect to the centre of mass of the two main bodies along the rotating frame respectively (see Figure 2.2), $\boldsymbol{r}^*$, $\boldsymbol{v}^*$ and $\boldsymbol{a}^*$ are the same vectors along the fixed axes and $\boldsymbol{R}$ is the rotation matrix expressing the orthogonal transformation from the rotating frame to the inertial one. The inertial reference frame $\{x^*, y^*, z^*\}$ and the rotating frame $\{x, y, z\}$ have the respective x and y axes on the plane containing the motion of the two main bodies, leaving the z-axis, which coincides between the two frames, to represent the consequent out-of-plane direction. In the case of the inertial frame, the x^* and the y^* directions are fixed in space, whereas the x-axis of the rotating frame is defined by the line passing through the two major bodies and the y-axis precedes it by $90°$.

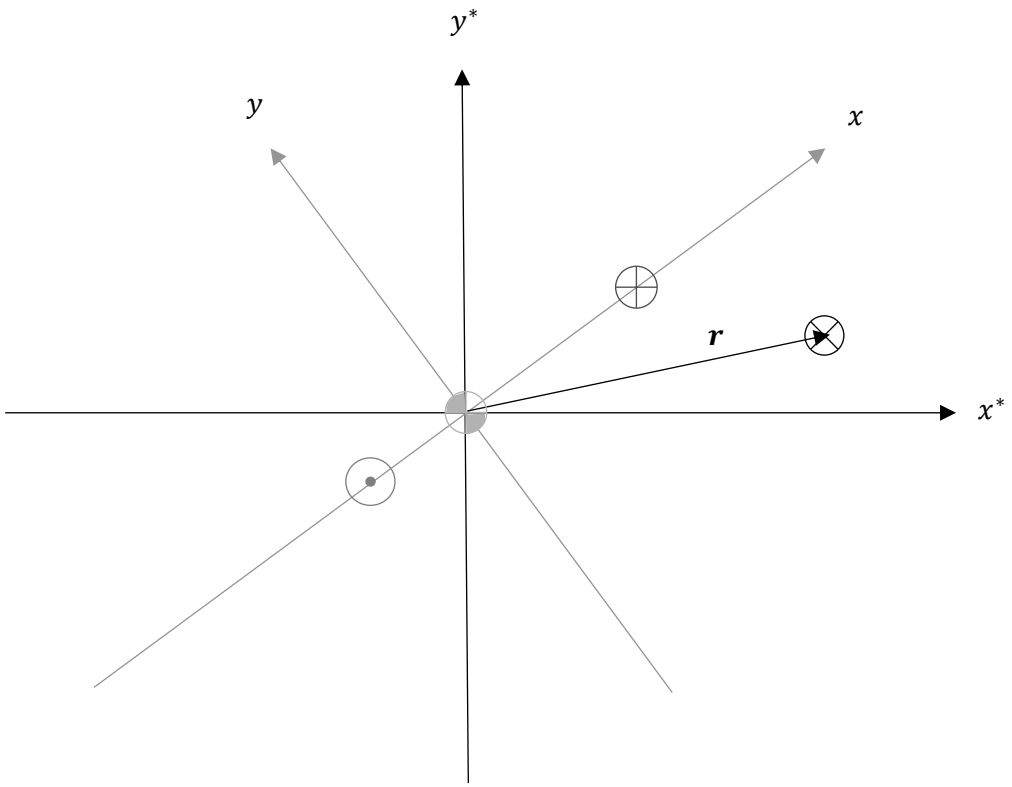

Figure 2.2: Reference frames.

By deriving the position and velocity relations, we have [18]

$$\boldsymbol{v}^* = \frac{d\boldsymbol{r}^*}{dt} = \boldsymbol{R}\left(\frac{d\boldsymbol{r}}{dt} + \boldsymbol{\Omega r}\right) = \boldsymbol{R}(\boldsymbol{v_{rel}} + \boldsymbol{\Omega r})$$

Equation 2.3

$$\boldsymbol{a}^* = \frac{d\boldsymbol{v}^*}{dt} = \boldsymbol{R}\left[\frac{d^2\boldsymbol{r}}{dt^2} + 2\boldsymbol{\omega} \times \frac{d\boldsymbol{r}}{dt} + \frac{d\boldsymbol{\omega}}{dt} \times \boldsymbol{r} + \boldsymbol{\omega} \times (\boldsymbol{\omega} \times \boldsymbol{r})\right] = \boldsymbol{R}\left[\boldsymbol{a_{rel}} + 2\boldsymbol{\omega} \times \frac{d\boldsymbol{r}}{dt} + \frac{d\boldsymbol{\omega}}{dt} \times \boldsymbol{r} + \boldsymbol{\omega} \times (\boldsymbol{\omega} \times \boldsymbol{r})\right]$$

where $^{d}\blacksquare/_{dt}$ expresses the derivation in time, × expresses the vector product, $\boldsymbol{v_{rel}}$ is the velocity in the rotating frame excluding the component due to the rotation of the frame itself and $\boldsymbol{\Omega}$ is a skew-symmetric matrix which describes the rotation of the rotating frame with respect to the inertial one, defined as

$$\boldsymbol{\Omega} = \boldsymbol{R}^{\boldsymbol{T}} \frac{d\boldsymbol{R}}{dt}$$

and, as such, can be written in the form

$$\boldsymbol{\Omega} = \begin{bmatrix} 0 & -\omega_z & \omega_y \\ \omega_z & 0 & -\omega_x \\ -\omega_y & \omega_x & 0 \end{bmatrix}$$

The rotation can be expressed through the vector $\boldsymbol{\omega}$ defined in the rotating frame, whose components along the moving axes are $\omega_x, \omega_y, \omega_z$ and we can therefore rewrite the relation (Equation 2.3) as

$$\boldsymbol{v}^* = \boldsymbol{R}\left(\frac{d\boldsymbol{r}}{dt} + \boldsymbol{\omega} \times \boldsymbol{r}\right)$$

Finally, the last two quantities can be defined with respect to the fixed frame, obtaining

$$\boldsymbol{\Omega}^* = \boldsymbol{R}\boldsymbol{\Omega}\boldsymbol{R}^T$$

Equation 2.4

$$\boldsymbol{\omega}^* = -\boldsymbol{\omega}$$

2.1.2.1.2 Jacobi's Integral

Jacobi's integral is a constant of the motion in the restricted three-body problem and it is defined as

$$J = \frac{1}{2}\omega^2(x^2 + y^2) + \frac{Gm_1}{\rho_1} + \frac{Gm_2}{\rho_2}$$

Equation 2.5

where G is the universal gravitational constant equal to $6.67408 \cdot 10^{-11}\ \mathrm{m^3/kg \cdot s^2}$, ω is the angular velocity of the finite masses m_1 and m_2, which is constant and equal to [18]

$$\omega^2 = \frac{G(m_1 + m_2)}{\rho^3}$$

and ρ_1, ρ_2, ρ are the distances of the object from the primary masses and the distance between the masses themselves respectively.

The equation of motion of the small body can be expressed in terms of the Jacobi constant by considering the gradient of J, denoted by the operator $\boldsymbol{\nabla}$ in the following formulation

$$\frac{d^2\boldsymbol{r}}{dt^2} + 2\boldsymbol{\omega} \times \frac{d\boldsymbol{r}}{dt} = \boldsymbol{\nabla}J$$

Equation 2.6

By performing a scalar multiplication of the terms of Equation 2.6 by the relative velocity $\boldsymbol{v_{rel}}$ we have

$$\frac{d^2\boldsymbol{r}}{dt^2}\cdot\frac{d\boldsymbol{r}}{dt}+2\left(\boldsymbol{\omega}\times\frac{d\boldsymbol{r}}{dt}\right)\cdot\frac{d\boldsymbol{r}}{dt}=\boldsymbol{\nabla}J\cdot\frac{d\boldsymbol{r}}{dt}$$

The definition of the constant C is subsequently obtained through an integration as

$$J=\frac{1}{2}\frac{d\boldsymbol{r}}{dt}\cdot\frac{d\boldsymbol{r}}{dt}+C$$

Equation 2.7

The aforementioned C constant does not vary along the trajectory of the small body in the restricted three-body problem framework and allows to define surfaces in the rotating reference frame corresponding to $|\boldsymbol{v_{rel}}|=0$, which confine the motion of the small body to one side of the curves [18].

By combining Equation 2.5 and Equation 2.7, we have the following formulation of the relative velocity, which will be used to determine Tisserand's parameter in section 2.1.2.1.3

$${v_{rel}}^2=\omega^2(x^2+y^2)+\frac{2Gm_1}{\rho_1}+\frac{2Gm_2}{\rho_2}-C$$

Equation 2.8

that can also be written as

$${v_{rel}}^2=-\boldsymbol{r}\cdot\boldsymbol{\omega}\times(\boldsymbol{\omega}\times\boldsymbol{r})+\frac{2Gm_1}{\rho_1}+\frac{2Gm_2}{\rho_2}-C$$

Equation 2.9

2.1.2.1.3 Tisserand's Parameter

Equation 2.3 can be re-formulated, considering the definition (Equation 2.4), to express $\boldsymbol{v_{rel}}$ as

$$\boldsymbol{v_{rel}}=\boldsymbol{R^T}(\boldsymbol{v}^*+\boldsymbol{\Omega}^*\boldsymbol{r}^*)$$

where $\boldsymbol{v_{rel}}$ is the velocity of the small body in the rotating frame excluding the component due to the rotation of the frame itself and $\boldsymbol{v}^*$ is its complete velocity along the inertial frame, and therefore

$$\boldsymbol{v_{rel}}^{\boldsymbol{T}}\boldsymbol{v_{rel}}={v_{rel}}^2={v^*}^2-2\boldsymbol{\omega}\cdot(\boldsymbol{r}^*\times\boldsymbol{v}^*)-\boldsymbol{r}\cdot\boldsymbol{\omega}\times(\boldsymbol{\omega}\times\boldsymbol{r})$$

Equation 2.10

By comparing Equation 2.9 and Equation 2.10, it is apparent that

$$v^{*2} = 2\boldsymbol{\omega} \cdot (\boldsymbol{r}^* \times \boldsymbol{v}^*) + \frac{2Gm_1}{\rho_1} + \frac{2Gm_2}{\rho_2} - C$$

Equation 2.11

Now, by assuming m_1 to be the mass of the Sun and m_2 to be the mass of the planet around which the fly-by is performed, we can approximate the angular velocity ω as

$$\omega^2 \cong \frac{Gm_1}{\rho^3} = \frac{\mu}{\rho^3}$$

Equation 2.12

where μ is the gravitational constant of the Sun.

Given the planar nature of the heliocentric motion of the small body, we can write

$$\boldsymbol{\omega} \cdot (\boldsymbol{r}^* \times \boldsymbol{v}^*) = \omega h \cos i = \omega \sqrt{\mu a (1 - e^2)} \cos i$$

Equation 2.13

where h, a, e and i are the small body's heliocentric angular momentum, semi-major axis, eccentricity and inclination respectively.

By considering Equation 2.12 and Equation 2.13, as well as the vis viva equation

$$v^{*2} = \mu \left(\frac{2}{\rho_1} - \frac{1}{a} \right)$$

and neglecting the term relative to the gravitational attraction of m_2, Equation 2.11 can be re-written as

$$\mu \left(\frac{1}{a} + 2 \sqrt{\frac{a(1 - e^2)}{\rho^3}} \cos i \right) = C$$

Equation 2.14

where C is the dimensional version of the Tisserand parameter [24].

2.1.2.2 *Velocity of the Object at the Entrance of the Planet's Sphere of Influence*

The aim of the present section is to determine a formulation for the planetocentric velocity of an object at the beginning of its fly-by of a planet, which will be required in the definition of the resonance conditions on the b-plane (see section 2.3.2).

By introducing the value of the Tisserand parameter C, determined in the previous section (Equation 2.14), in Equation 2.8 and neglecting the gravitational term due to the planet, as done for Equation 2.14 , we have that

$$U^2 = \mu\left(\frac{3}{\rho} - \frac{1}{a} - 2\sqrt{\frac{a(1-e^2)}{\rho^3}}\cos i\right) = \frac{3\mu}{\rho} - C$$

Equation 2.15

as

$$\boldsymbol{v_{rel}} = \boldsymbol{v} - \boldsymbol{\omega} \times \boldsymbol{r} = \boldsymbol{v} - \boldsymbol{v_P} = \boldsymbol{U}$$

where μ is the gravitational constant of the Sun, $\boldsymbol{U}$ is the relative velocity of the object with respect to the planet (planetocentric velocity) and $\boldsymbol{v_P}$ is the velocity of the planet around the system barycentre.

2.1.2.3 *Normalised Formulation*

A normalised version of the Tisserand parameter $\overline{T}$ is quite commonly employed [19] and is defined as

$$\overline{T} = \frac{C}{{v_P}^2}$$

Assuming the planet to be on a circular orbit around the Sun, we have

$$v_P = \sqrt{\frac{\mu}{\rho}}$$

$$\overline{T} = \rho\left(\frac{1}{a} + 2\sqrt{\frac{a(1-e^2)}{\rho^3}}\cos i\right) = \frac{\rho}{a} + 2\sqrt{\frac{a(1-e^2)}{\rho}}\cos i = \frac{1}{\overline{a}} + 2\sqrt{\overline{a}(1-e^2)}\cos i$$

$$\overline{U}^2 = 3 - \overline{T}$$

where

$$\overline{U}^2 = \frac{U^2}{{v_P}^2}$$

$$\overline{a} = \frac{a}{\rho}$$

are the non-dimensional relative velocity of the small mass with respect to the planet and semi-major axis respectively [25].

2.2 B-Plane Definition

The b-plane is a planetocentric reference frame $\{\xi, \eta, \zeta\}$, such that ξ and ζ are coordinates on the b-plane and η is normal to the aforementioned plane. The direction of the η-axis is identified by the planetocentric velocity vector $\boldsymbol{U}$, whereas the ζ-axis is directed in the opposite direction as the projection of the planet's velocity vector on the b-plane and the ξ-axis completes the right-handed reference frame [26]. The impact parameter is the intersection of the incoming hyperbola asymptote with the b-plane and is therefore defined as

$$b = \sqrt{\xi^2 + \zeta^2}$$

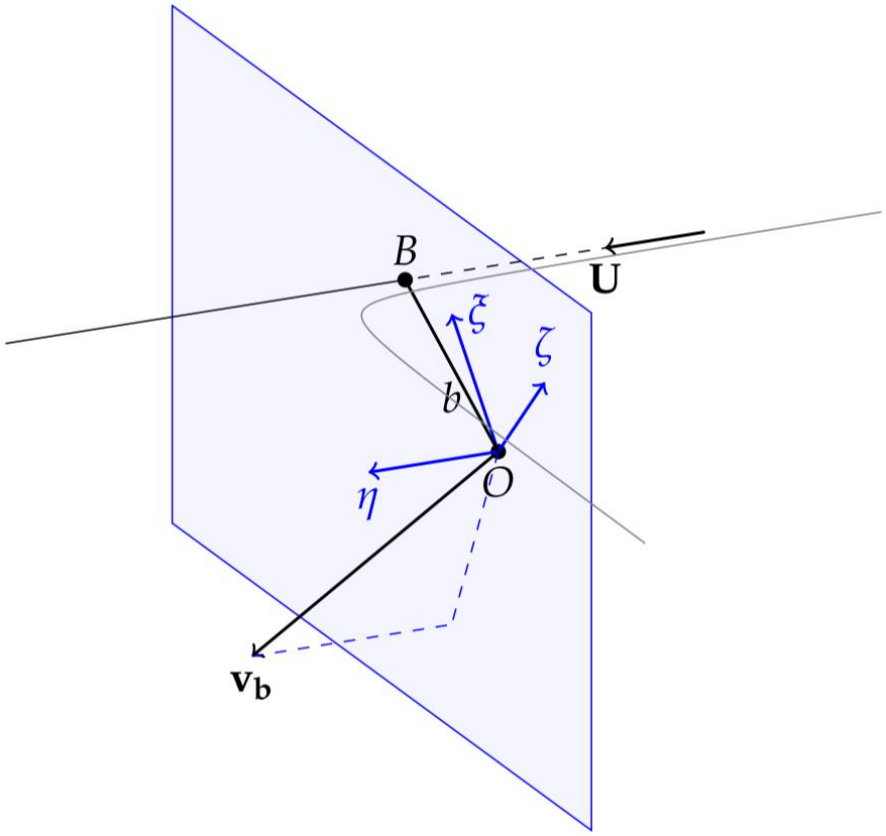

Figure 2.3: B-plane geometry [27].

The b-plane has the very useful property to conveniently characterise close approaches between an object and a planet, as it decouples the two main parameters that describe the encounter: the geometric distance and the timing of the close-approach. It can be shown that the ξ-axis represents the geometric distance between the two bodies' orbits at the encounter, whereas the ζ-axis represents a shift in the time of arrival of the object at the planet [19]; a positive value of ζ represents a delay and vice-versa for a negative value of the coordinate. The

aforementioned properties are based on the approximation that, at the time of the encounter, the two orbits are straight lines [21].

Two different b-planes can be drawn for an encounter when considering a liked-conics approach: the one referred to the incoming asymptote of the hyperbola and the one relative to the outgoing one. Given the definition of the b-plane reference frame, the value of the η coordinate is negative before the close-approach and positive when the fly-by has already happened [22].

2.2.1 Impact Region

The impact region is the locus of the points on the plane tangent to the small body's entry point in the planet's Sphere of Influence (SOI) that will lead to an impact (see Figure 2.4). The size of the region depends on both the planet and the body approaching it, as it takes the effect of the celestial body's gravitation into account, as well as the small body's planetocentric velocity.

The intersection of the impact region with the b-plane corresponds to a circle with a radius equal to

$$b_{IR} = r_P \sqrt{1 + \frac{2\mu_P}{r_P U^2}}$$

where r_P is the radius of the planet, μ_P is its gravitational constant and U is the object's relative approach velocity at the entrance of the SOI [28].

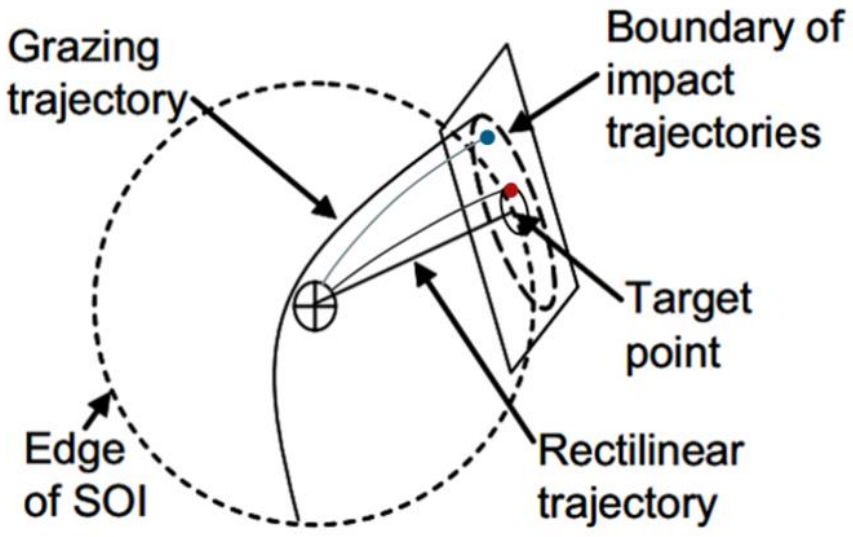

Figure 2.4: Impact region [27].

2.3 Öpik's Theory

Öpik's theory for planetary encounters is based on a linked two-body approach. The object is considered to be on an elliptical heliocentric orbit until its encounter with the planet, where it transitions to a hyperbolic orbit under the sole attraction of the planet and finally returns to a different heliocentric elliptical orbit. In the framework of the linked-conics, the planet's SOI is considered infinitesimal when viewed from the Sun's perspective and infinitely large when performing the fly-by under the planet's sole attraction. As the effect of the encounter is considered to be an instantaneous deflection of the object's velocity vector from its incoming asymptote to its outgoing one, Öpik's theory is more accurate for deep encounters. This is due to the planetocentric velocity of the object being higher, thus better approximated by the point-like interaction; $\overline{T} < 3$ is the necessary condition to have a hyperbolic flyby [29] and lower values are preferred as they correspond to higher velocities. Furthermore, the theory is exact in the case when in which the two bodies feature a miss-distance equal to zero [19].

An extension of the theory has been formulated by Valsecchi et al. [19] allowing for its use in the case of near misses (see section 2.5).

2.3.1 Planetocentric Reference Frame

The following planetocentric reference frame (see Figure 2.5) is central to the discussion of Öpik's theory; it is based on the hypothesis of the planet being on a circular orbit around the Sun and is defined as follows:

- X-axis directed along the position vector of the planet with respect to the Sun (the same direction of the x-axis of the rotating reference frame of chapter 2.1.2)
- Y-axis in the direction of the planet's velocity vector (the same direction as $\boldsymbol{v_P}$, the planet velocity vector, of section 2.1.2.2)
- Z-axis completing the right-handed frame

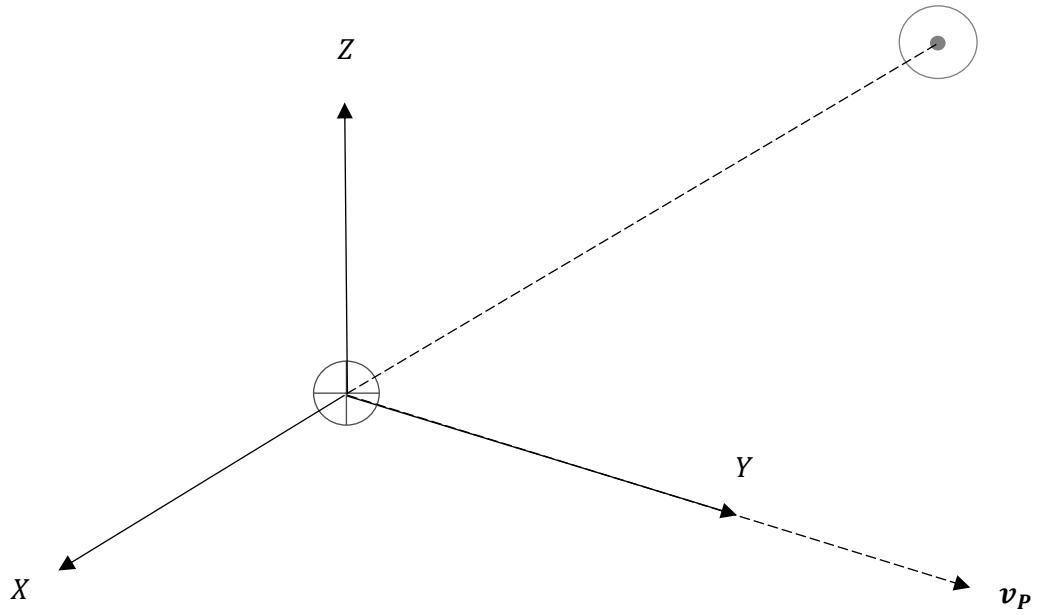

Figure 2.5: Planetocentric reference frame.

Vectors in the planetocentric reference frame are described by means of the angles Θ and ϕ, represented in Figure 2.6.

The angle Θ can take values between 0 and π, whereas we have $-\pi/2 < \phi < \pi/2$ for encounters at the ascending node and $\pi/2 < |\phi| < \pi$ for encounters at the descending node [17], as ϕ describes the inclination of the velocity vector with respect to the orbital plane of the planet. These excursions allow for the description of all the possible orientations of $\boldsymbol{U}$.

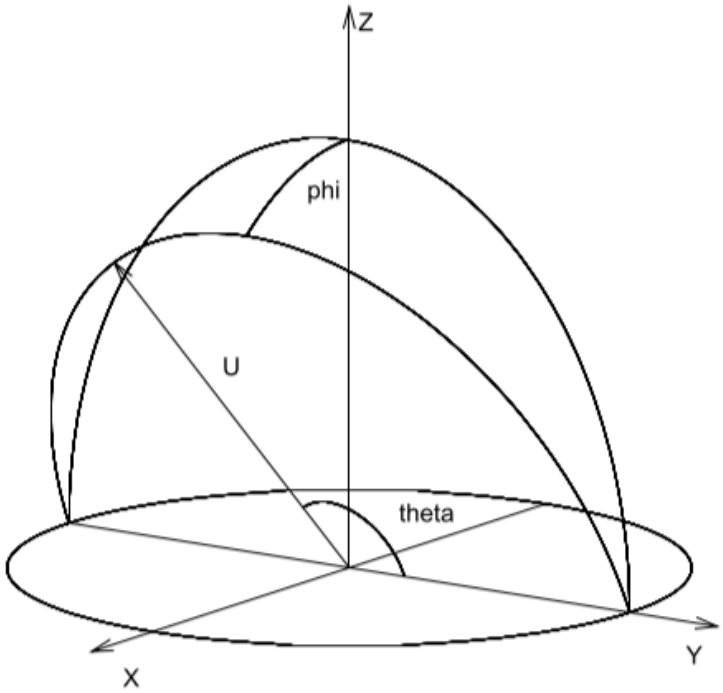

Figure 2.6: Planetocentric reference frame angles [19].

The following transformation can be applied to express the coordinates of vectors originally in the planetocentric reference frame in the b-plane. In other words, Equation 2.16 allows transforming a vector $\{X, Y, Z\}'$ expressed in the planetocentric reference frame (i.e. the rotating frame of the Restricted Three-Body Problem centred in the planet) into the same vector $\{\xi, \eta, \zeta\}'$ expressed in the b-plane.

$$\begin{Bmatrix} \xi \\ \eta \\ \zeta \end{Bmatrix} = \begin{bmatrix} 1 & 0 & 0 \\ 0 & \cos\Theta & \sin\Theta \\ 0 & -\sin\Theta & \cos\Theta \end{bmatrix} \begin{bmatrix} \cos\phi & 0 & -\sin\phi \\ 0 & 1 & 0 \\ \sin\phi & 0 & \cos\phi \end{bmatrix} \begin{Bmatrix} X \\ Y \\ Z \end{Bmatrix}$$

Equation 2.16

A very important consideration to make is that Öpik's theory cannot be used in the case of exactly tangent and coplanar orbits and the results become unreliable for orbits approaching these conditions, corresponding to $\sin\Theta \cong 0$ [19]; [29].

The theory can be extended to the case of an elliptical planetary orbit by defining the angles Θ and ϕ in function of the Y-axis, which would therefore not be perpendicular to the Sun-planet direction at all times [19].

2.3.2 Planetocentric Velocity of the Object

From Equation 2.15, we have

$$U = \sqrt{\mu\left(\frac{3}{\rho} - \frac{1}{a} - 2\sqrt{\frac{a(1-e^2)}{\rho^3}}\cos i\right)}$$

As can be observed in Figure 2.6 the components of the planetocentric velocity in the planetocentric reference frame are

$$\begin{cases} U_X = U\sin\Theta\sin\phi \\ U_Y = U\cos\Theta \\ U_Z = U\sin\Theta\cos\phi \end{cases}$$

from which, we can write

$$\begin{cases} \cos\Theta = \dfrac{U_Y}{U} \\ \tan\phi = \dfrac{U_X}{U_Z} \end{cases}$$

As the planet is considered to be on a circular orbit around the Sun on the ecliptic plane, in order to have an encounter between the object and the latter, the following condition must be satisfied

$$\cos\theta = \frac{1}{e}\left(\frac{p}{r_P} - 1\right)$$

This is equivalent to imposing that the small body is at a distance from the Sun which is equivalent to the planet's.

Through the formulas for the radial and transversal components of the velocity in the case of a two-body problem, we can derive

$$\begin{cases} U_X = \pm\sqrt{\dfrac{\mu}{\rho}\left[2 - \dfrac{1}{\overline{a}} - \overline{a}(1-e^2)\right]} \\ U_Y = \sqrt{\dfrac{\mu}{\rho}\overline{a}(1-e^2)}\cos i - \sqrt{\dfrac{\mu}{\rho}} \\ U_Z = \pm\sqrt{\dfrac{\mu}{\rho}\overline{a}(1-e^2)}\sin i \end{cases}$$

Equation 2.17

and therefore

$$\cos\Theta = \frac{1}{2\overline{U}}\left(1 - \frac{1}{\overline{a}} - \overline{U}^2\right)$$

Equation 2.18

$$\tan\phi = \sqrt{\frac{2 - {}^1/_{\overline{a}}}{\overline{a}(1-e^2)} - 1}\,\frac{1}{\sin i}$$

It should be noted that the components of the planetocentric velocity, as described in Equation 2.17, are based on the assumption that the positions of the small body and the planet during the encounter coincide with respect to the Sun (i.e. linked conics method), as stated at the beginning of chapter 2.3. This assumption will not be considered in the numerical study of the close-approach characterisation in this thesis, as it would not allow to properly distinguish impact and miss conditions. The results based on this assumption will be replaced by numerical computations, as will be discussed in section 2.8.

2.4 Fly-by in the B-Plane

2.4.1 Rotation of the Planetocentric Velocity Vector

As described by Valsecchi et al. [19], when the object performs its fly-by, its planetocentric velocity vector is rotated to match the direction of the outgoing asymptote, while its modulus is kept constant.

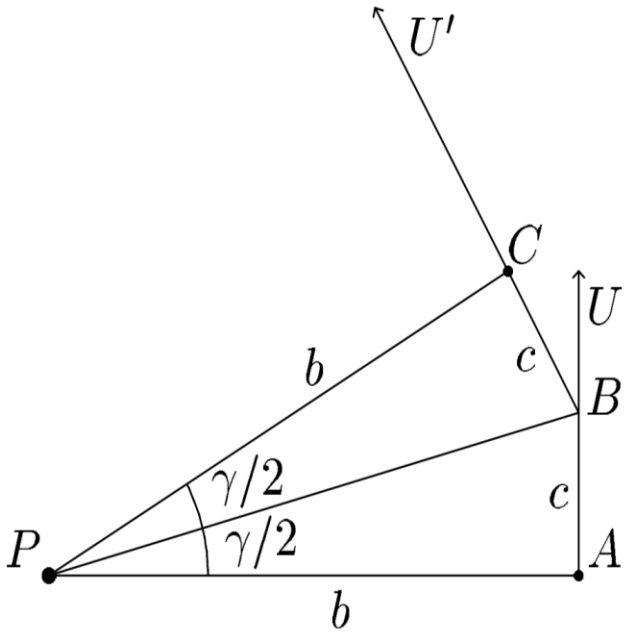

Figure 2.7: Fly-by effect on the planetocentric velocity [19].

From Figure 2.7, we can write

$$\tan\left(\frac{\gamma}{2}\right) = \frac{c}{b}$$

where γ is the turn angle, b is the impact parameter and c is the length of the segment connecting the point of interception between the asymptotes with their interception with the respective b-plane (i.e. incoming and outgoing).

Given Equation 2.1 and Equation 2.2, the previous formulation can be re-written as

$$\tan\left(\frac{\gamma}{2}\right) = \frac{\mu}{bU^2}$$

thus allowing the derivation of the following formulations

$$\sin\gamma = \frac{b^2 - c^2}{b^2 + c^2}$$

$$\cos\gamma = \frac{2bc}{b^2 + c^2}$$

which describe the turn angle as a function of the impact parameter b and the c parameter, as described above.

We can define the angle ψ as

$$\begin{cases} \xi = b\sin\psi \\ \zeta = b\cos\psi \end{cases} \Longrightarrow \psi = \arctan\left(\frac{\xi}{\zeta}\right)$$

and introduce it in the planetocentric reference frame representation of the relative velocity before and after the flyby (see Figure 2.8). The quantities after the fly-by are denoted by an apex symbol.

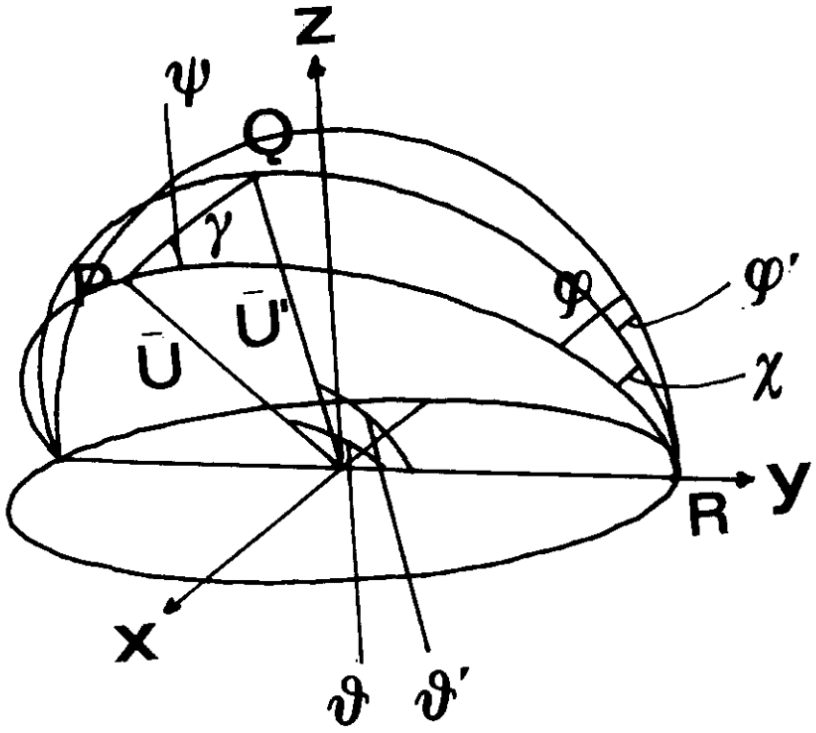

Figure 2.8: Rotation of the planetocentric velocity vector in the planetocentric reference frame [17].

The quantity $\overline{U}$ portrayed in Figure 2.8 is the normalised counterpart to the planetocentric velocity vector, as described in section 2.1.2.3, which shares its direction with the dimensional vector.

The problem of determining the values of the Θ and ϕ angles after the fly-by can be solved through the spherical triangle formulas, imposing $\chi = \phi - \phi'$ to obtain

$$\cos\Theta' = \cos\Theta\cos\gamma + \sin\Theta\sin\gamma\cos\psi$$

Equation 2.19

$$\sin\chi = \frac{\sin\gamma\sin\psi}{\sin\Theta'}$$

$$\cos\chi = \frac{\sin\Theta\cos\gamma - \cos\Theta\sin\gamma\cos\psi}{\sin\Theta'}$$

$$\tan\chi = \frac{\sin\gamma\sin\psi}{\sin\Theta\cos\gamma - \cos\Theta\sin\gamma\cos\psi}$$

$$\tan\phi' = \frac{\tan\phi - \tan\chi}{1 + \tan\chi\tan\phi}$$

Equation 2.20

A formulation describing the values of Θ' and ϕ' based on the pre-encounter conditions has been obtained; this will allow the prediction of the fly-by outgoing coordinates.

2.4.2 B-Plane Coordinates after the Fly-by

Equation 2.19 and Equation 2.20 describing the values of angles Θ and ϕ after the fly-by can be rewritten as [19]

$$\cos\Theta' = \frac{b^2 - c^2}{b^2 + c^2}\cos\Theta + \frac{2c\zeta}{b^2 + c^2}\sin\Theta$$

$$\sin\Theta' = \frac{\sqrt{[(b^2 - c^2)\sin\Theta - 2c\zeta\cos\Theta]^2 + 4c^2\xi^2}}{b^2 + c^2}$$

$$\cos\phi' = \frac{[(b^2 - c^2)\sin\Theta - 2c\zeta\cos\Theta]\cos\phi + 2c\xi\sin\phi}{\sqrt{[(b^2 - c^2)\sin\Theta - 2c\zeta\cos\Theta]^2 + 4c^2\xi^2}}$$

$$\sin\phi' = \frac{[(b^2 - c^2)\sin\Theta - 2c\zeta\cos\Theta]\sin\phi - 2c\xi\cos\phi}{\sqrt{[(b^2 - c^2)\sin\Theta - 2c\zeta\cos\Theta]^2 + 4c^2\xi^2}}$$

Considering the rotation of the velocity vector portrayed in Figure 2.7 and the transformation of coordinates in Equation 2.16, the b-plane coordinates after the fly-by expressed in the post-encounter b-plane can be written as

$$\xi' = \frac{\xi\sin\Theta}{\sin\Theta'} = \frac{\xi(b^2 + c^2)\sin\Theta}{\sqrt{[(b^2 - c^2)\sin\Theta - 2c\zeta\cos\Theta]^2 + 4c^2\xi^2}}$$

$$\zeta' = \frac{(b^2 - c^2)\zeta\sin\Theta - 2b^2c\cos\Theta}{\sqrt{[(b^2 - c^2)\sin\Theta - 2c\zeta\cos\Theta]^2 + 4c^2\xi^2}}$$

It is important to note how the definition of the planetocentric reference frame does not vary across the velocity vector rotation, as it is defined solely through the coordinates of the planet, which remain constant as the rotation is assumed to be instantaneous, whereas the post-encounter b-plane does not correspond to the one defined at the arrival of the small body to the planet, as its normal is defined by the direction of the planetocentric velocity vector.

2.5 Extended Öpik's Theory

Valsecchi et al. [19] introduced an extension of Öpik's original theory to near misses to obtain a closer correspondence of the results produced by the theory of close-approaches and those obtained through the propagation of the small body's coordinates in time. This formulation relaxes the hypothesis of complete superposition between the position of the small body and the planet at the time of the encounter by introducing

a set of correction factors linearised in the miss distance [19]. The obtained corrections are therefore more accurate for deeper encounters.

The extension of Öpik's theory to near misses considers the object as having a uniform rectilinear motion along the incoming and outgoing asymptotes [19]. The rotation from the incoming asymptote to the outgoing one is considered to take place in the point of minimum distance between the two bodies, which is not necessarily the Minimum Orbital Intersection Distance (MOID) and corresponds instead to the projection of the conditions at the entrance of the SOI on the b-plane, given the rectilinear motion, and is assumed to be instantaneous.

In the results obtained in the present thesis, only the linearised modelling of the fly-by of the aforementioned formulation will be implemented, as the orbit of the Earth will be considered as elliptical, differently from the assumption made in both Öpik's classical theory and its extension.

2.6 Resonant Returns

2.6.1 Resonant Return Circles

In order to witness a planetary encounter of the object, under the assumption of Keplerian motion between the two close-approaches, the following condition must be satisfied

$$k\mathrm{T}_P = h\mathrm{T}'$$

where T_P and T' are the periods of the planet and the object after the encounter respectively and k, h are integer numbers, not to be confused with the angular momentum used in section 2.1.2. If we consider the small body to be on an elliptical orbit and the planet to be on a circular orbit, the condition can be rewritten as

$$\overline{a}' = \frac{a'}{\rho} = \left(\frac{k}{h}\right)^{2/3}$$

For each value of the normalised semi-major axis, we can compute (Equation 2.18)

$$\cos\Theta' = \frac{1}{2\overline{U}'}\left(1 - \frac{1}{\overline{a}'} - \overline{U}'^2\right)$$

By rewriting Equation 2.19 to calculate $\cos\psi$ and introducing the previously calculated expressions for the present terms, the following equation can be written

$$\xi^2 + \zeta^2 - \frac{2c\sin\Theta}{\cos\Theta' - \cos\Theta}\zeta + \frac{c^2(\cos\Theta' - \cos\Theta)}{\cos\Theta' - \cos\Theta} = 0$$

which is none-other than the equation of a circle in the b-plane centred in D on the ζ-axis with radius R.

$$\xi^2 + (\zeta - D)^2 = R^2$$

$$\begin{cases} D = \dfrac{c \sin \Theta}{\cos \Theta' - \cos \Theta} \\ R = \left| \dfrac{c \sin \Theta'}{\cos \Theta' - \cos \Theta} \right| \end{cases}$$

Therefore, for each value of the normalised semi-major axis $\overline{a}'$, a circle on the b-plane can be drawn. These circles are referred to as resonance circles, as they represent the loci of orbits that will bring the object back to the planet after a certain amount of revolutions of both bodies.

A convenient notation for the resonant circles is "(h, k)", to represent the number of periods of the deflected small body and the planet necessary to obtain the return respectively. This notation can also be applied to the keyholes, described in seciton 2.6.2.

The formualtion described in this thesis is based on the assumption that the small body's position coincides with that of the planet with respect to the Sun, as per Öpik's classical theory. However, this simplification still provides a good approximation of the resonace conditions, as the the higher-order terms in ξ and ζ, which are present when relaxing the aforementioned hypothesis, is limited to a slight distortion of the circles [19]. Nevertheless, the conditions corresponding to a return of an object to the planet portrayed in the results of this thesis will be computed numerically in order to guarantee the expected returns (see section 2.8).

2.6.1.1 *Reachability of the Resonances*

Circles with a value of the radius $R < \xi_b$ are considered as unreachable, as ξ_b is the value of ξ of the incoming trajectory and it is the minimum value that the impact parameter can reach in the case that the two orbits are perfectly phased (i.e. it correponds to the MOID) [7].

Furthermore, resonant circles can theoretically be drawn for any couple of values (h, k). However, as the b-plane is built on the hypothesis of a two-body propagation, the circles corresponding to returns that would be very distant in time cannot be considered as representative of the real conditions. A value of $h = k = 10$ is a reasonable limit for the choice of resonant circles [21] [27].

2.6.2 Keyholes

The keyholes are the regions of the b-plane that will bring to a subsequent encounter were the asteroid to pass through one of them. They can represent either a hit, in which case they are none-other than the pre-images of the planet's cross-section on the b-plane, or more generally a subsequent close-encounter (for example the pre-image of the SOI's cross-section) [19]. The keyholes can therefore be considered as an extension of the resonant

circles, as they represent a set of possible return conditions corresponding to a target area, be it the Earth's cross-section or that of the SOI, whereas the resonant circles are the pre-image of a single return position: the one corresponding to the first encounter.

Per their nature, keyholes are linked to the semi-major axis of the asteroid after the first fly-by and thus are located in the vicinity of the resonant circles corresponding to their anticipated return. In the case of a purely Keplerian propagation between the encounters, the only b-plane coordinate to vary is ζ, as it is related to the timing of the encounter, whereas the geometry of the orbit (i.e. the MOID) is unaffected [19].

In particular, we have

$$\zeta'' = \zeta' - \left[\mathrm{mod}\left(v_P \cdot \Delta t + v_P \frac{\mathrm{T}_P}{2}, v_P \frac{\mathrm{T}_P}{2}\right)\right] \sin\Theta$$

where ζ'' and ζ' are the values of the ζ-coordinate at the resonant return and at the end of the first fly-by respectively and Δt is the time difference between the encounters.

2.6.2.1 *Secular Variation of ξ*

When considering a real case, the ξ component is bound to vary between encounters because of planetary perturbations on a short time scale and because of the Kozai cycle on a long time scale [19].

The short period variations are hard to model analytically, whereas the secular variation can be modelled through a linear term affecting ξ as

$$\xi'' = \xi' + \frac{d\xi}{dt}\Delta t$$

where ξ'' and ξ' are the values of the ξ-coordinate at the resonant return and at the end of the first fly-by respectively.

2.6.2.2 *Considerations on Keyhole Sizes*

The size of keyholes varies based on two main parameters: the distance from the ξ-axis and the number of periods connected with the relative resonant circle [21]. Keyholes that are situated further from the ξ-axis are larger, as the effect of the fly-by varies more significantly in space when closer to the planet, leading to very

different orbits. Keyholes connected to returns more distant in time are smaller, as the time difference at the encounter, due to a given difference in the period after the flyby, grows in time.

2.7 B-Plane Definition Considerations

The present section will describe a few characteristics of the b-plane concerning the practical implementation of the latter to analyse a close approach.

2.7.1 Coplanar Orbits

The first important consideration, even though relevant mainly for fictitious test cases, is that the b-plane cannot be employed for tangent coplanar encounters, as, in the tangency point, the planet velocity and the planetocentric velocity of the object are aligned, rendering the b-plane ill-defined. The b-plane can however be employed if the projection is considered in the point of entry of the small body in the planet's SOI, as the linearised local orbits do intersect each other, thus returning a correct result for the value of ξ (see section 2.7.2).

In the case of secant coplanar orbits, the ξ-component of the projection will always be equal to zero, as it will lie on the plane identified by the η and ζ versors. This condition is due to the fact that the two linearised orbits intersect each other and their geometric distance is therefore null (see section 2.7.3). The limitations of this approximation are prominent when studying two coplanar orbits that do not intersect, as the ξ-component on the b-plane will still be null, which is correct under the assumption that the orbits are locally straight, even though the real geometric distance is clearly greater than zero.

2.7.2 Effect of the SOI

The b-plane is usually plotted when the object being observed crosses the planet's SOI [7] and the registered point corresponds to the projection of said point on the b-plane. However, if we consider the motion of the object within the SOI and project the position of the object on a "local" b-plane defined at each instant (a similar consideration can be made projecting each step on the original b-plane), the figure appears changed; this difference can be related to the assumption that the two orbits are straight lines when the b-plane is drawn, but in reality follow a different curve. This effect is present also when assuming a pure two-body propagation for the object (see section 2.7.3), thus neglecting the effect of the fly-by.

This consideration is not relevant when applying the extended Öpik theory, as the object is assumed to move along its asymptotes during the flyby, resulting in the same b-plane.

2.7.3 Test Cases

Four test cases will now be presented to illustrate the effects detailed above. Test case A will be followed by three permutations of a second test case; B1, B2 and B3.

In the cases analysed in this section, the value of the η coordinate is not shown as it is not the focus of the present considerations. However the behaviour described in section 2.2 is still present: η is negative when analysing the b-plane before the point of minimum distance between the asteroid and the Earth and positive afterwards. It should be noted this is true even though no fly-by mechanics are implemented in these cases, which simply aim at observing the effects of the point of projection of the entry coordinates (i.e. the size of the SOI) on the b-plane.

2.7.3.1 *Case A*

This test case features two ad-hoc-created coplanar secant orbits that illustrate some of the considerations made above. The orbits have been propagated with a simple two-body method to avoid introducing other effects which would make the results less straight-forward to understand.

Figure 2.9 depicts a top-view of the orbits of the Earth and the NEO. In this case, the Earth is assumed to be on a circular orbit (blue line), whereas the NEO moves on an elliptical orbit (red line).

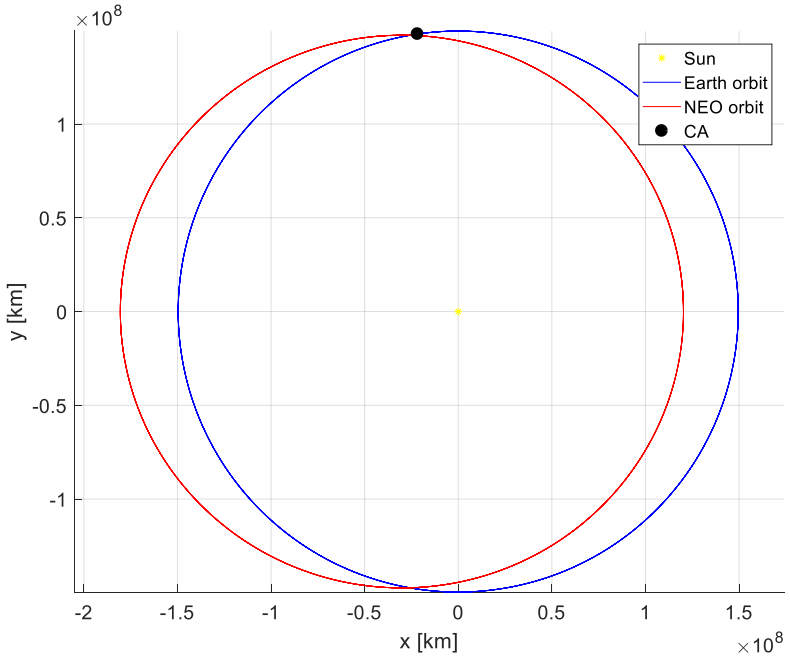

Figure 2.9: Case A - Orbits of the Earth and the NEO.

The close approach between the two bodies has been represented in several steps, from when the fictitious asteroid enters the planet's SOI, to when it leaves it. These steps are clearly visible in Figure 2.10 as, for every instant in which the NEO's distance from the Earth is smaller than the latter's SOI, it is assumed to be entering a fictitious SOI, to which corresponds a new b-plane. The passing of time is represented through colours, going from light-blue to yellow. It should be noted that no fly-by is performed in this fictitious case, as already stated.

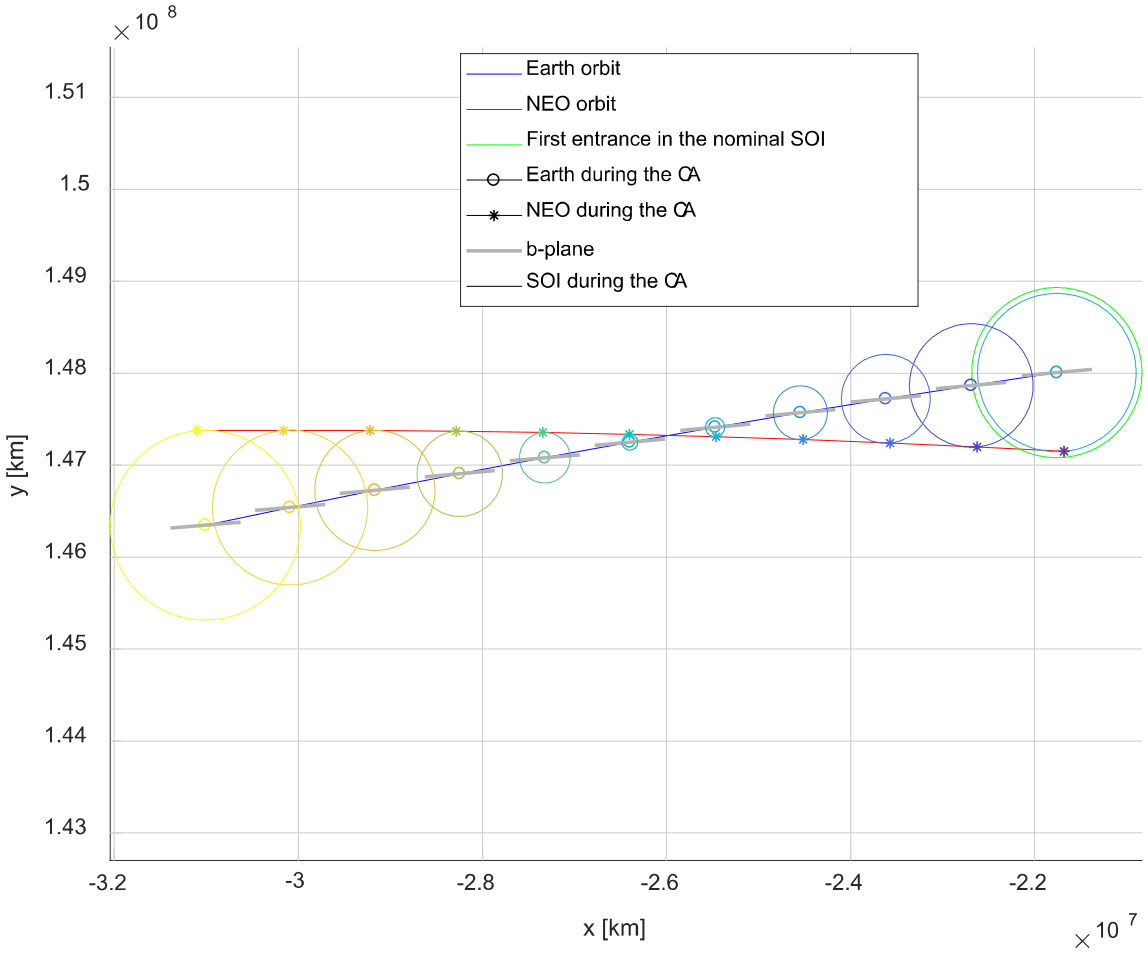

Figure 2.10: Case A - Close approach.

Figure 2.11 shows the b-plane representation of the encounter at the entrance in the SOI. The blue line represents the Earth's cross section on the b-plane. It is interesting to observe how the ξ-component is zero, as stated in section 2.7.1. Furthermore, it should be noted that this encounter would result in an impact of the NEO on the Earth's surface, as its projection on the b-plane is located within the region occupied by the planet's intersection with the plane.

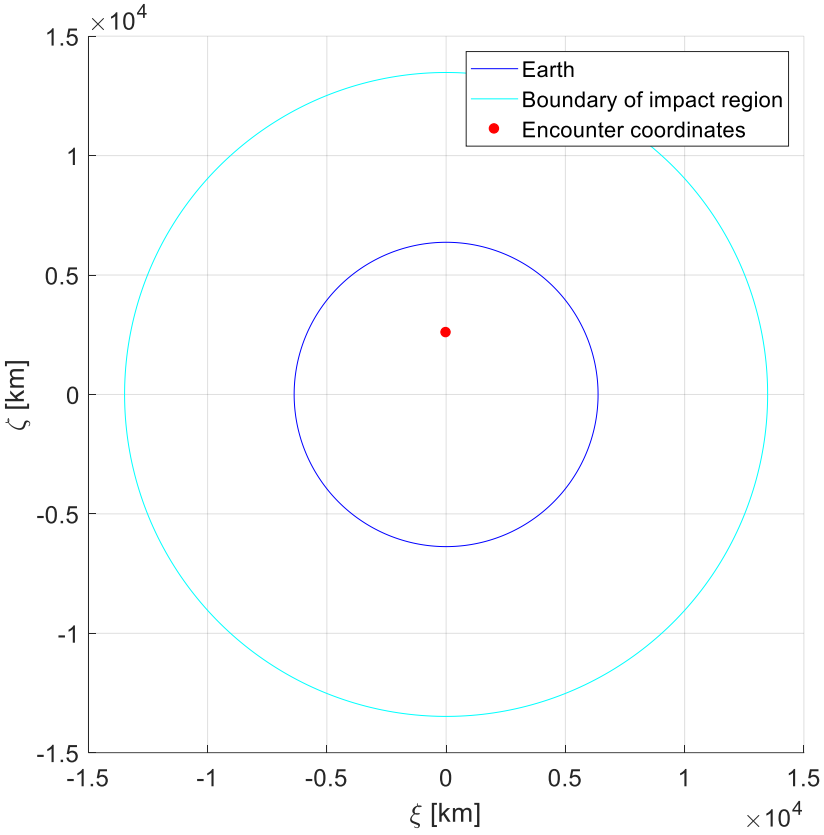

Figure 2.11: Case A - Close approach b-plane representation at the first entrance in the nominal SOI.

The variation of the ζ-component due to the projection of the asteroid's position on the local b-plane at each time step, represented by the modified Julian date ($\mathrm{mjd2000}$), can be seen in Figure 2.12; it should be noted that the variation is limited when considering the quantities at play.

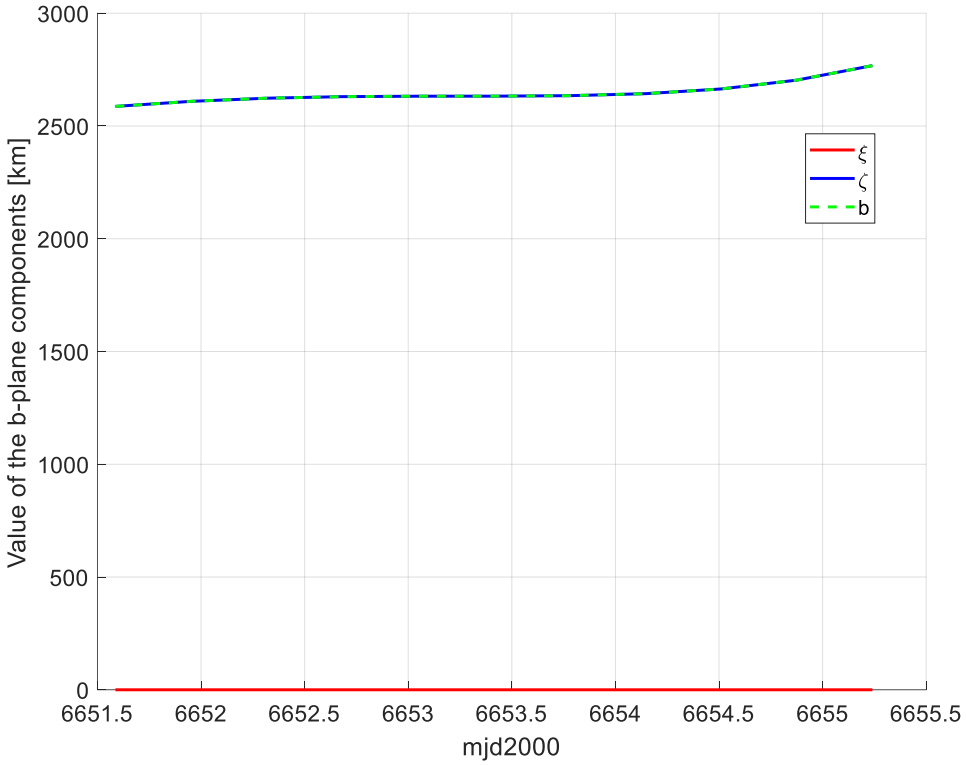

Figure 2.12: Case A - Close approach b-plane components evolution.

2.7.3.2 *Case B.1*

This test case features a perfectly circular orbit for the Earth, like in the previous example, whereas the NEO is on a non-coplanar elliptical orbit, which intersects the planet's in a single point. The propagation of the orbits is once more performed through the two-body approach. The depicted figures are the same as those in case A (see section 2.7.3.1), only applied to the case at hand. This is also valid for cases B.2 and B.3.

Figure 2.15 displays the effect of the SOI on the projection of the conditions at the entrance in the sphere on the b-plane; as for case A, the variations in the b-plane coordinates are relatively limited and the encounter between the two bodies would result in an impact. It can be noticed that the sign of the ξ coordinate is inverted across the flyby; this phenomenon can be understood by observing Equation 2.16 and considering the sign inversion that affects both X and Z.

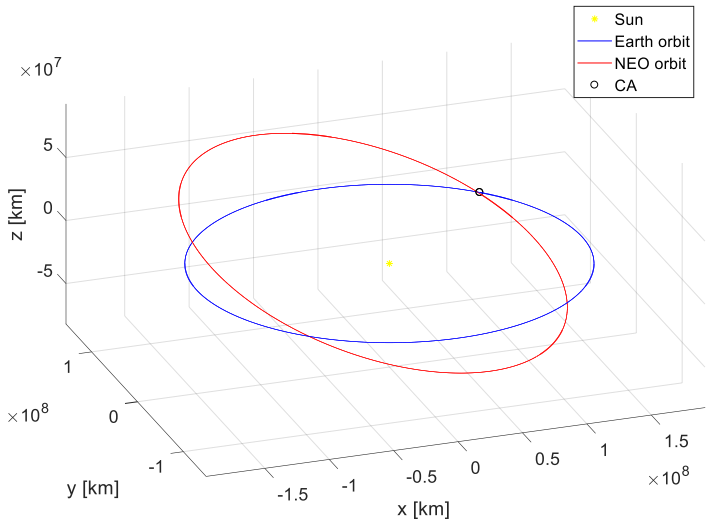

Figure 2.13: Case B.1 - Orbits of the Earth and the NEO.

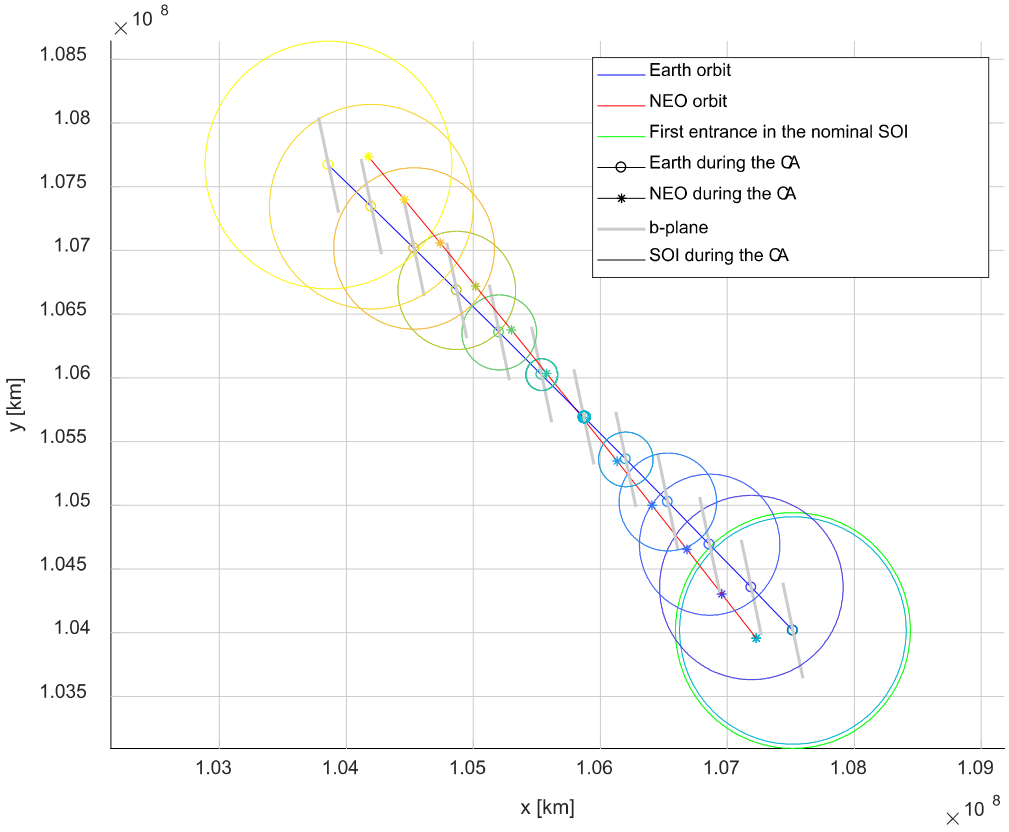

Figure 2.14: Case B.1 - Close approach.

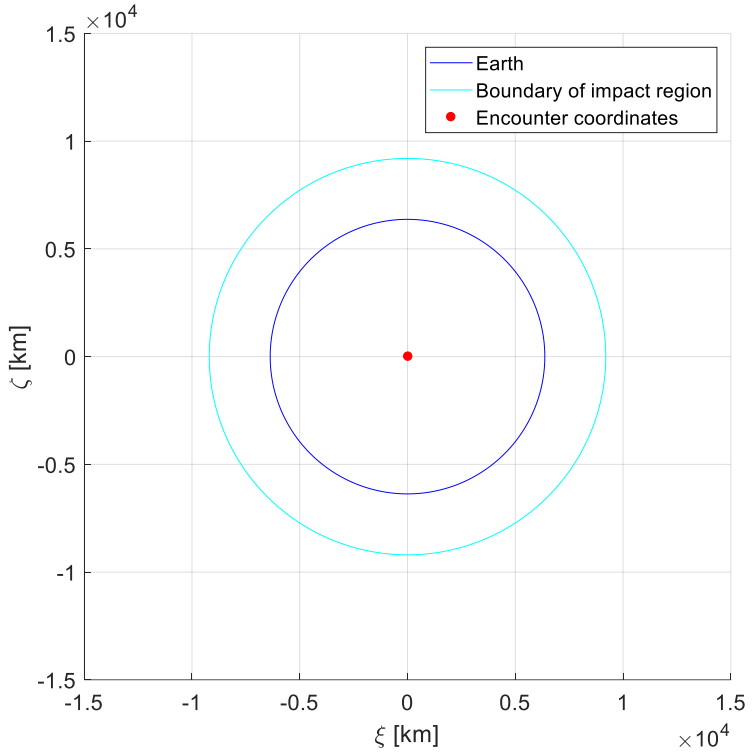

Figure 2.15: Case B.1 - b-plane representation of the close approach at the first entrance in the nominal SOI.

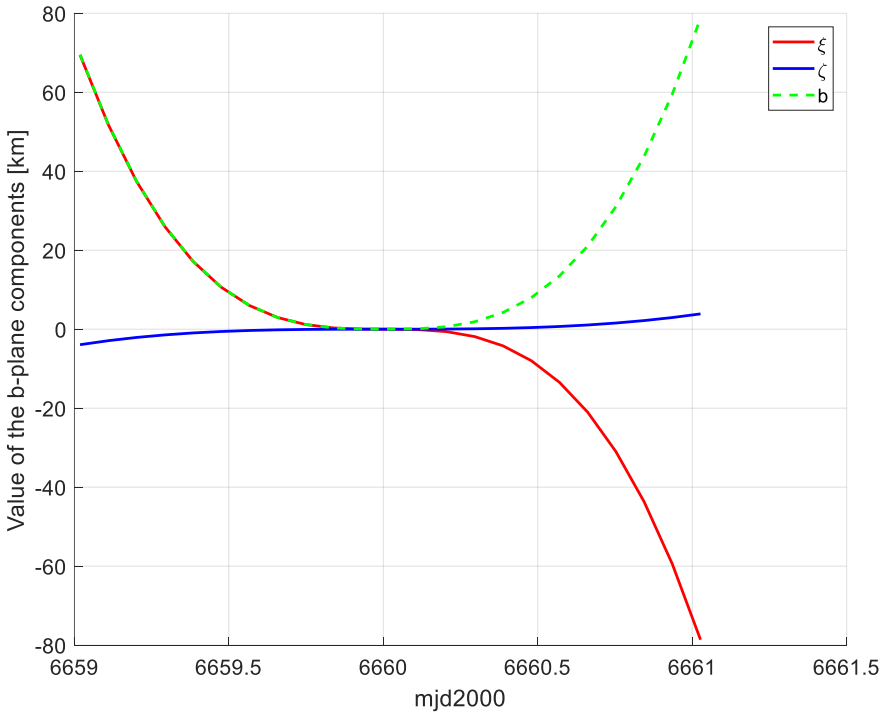

Figure 2.16: Case B.1 - b-plane components evolution.

2.7.3.3 *Case B.2*

Case B.2 presents the same orbits as case B.1 while introducing a delay of $10\ \mathrm{min}$ in the encounter: the NEO reaches the crossing between the two orbits when the Earth has already passed the MOID. The impact therefore becomes a close approach and a near miss in this case. As for the previous cases, the effect of the choice of the time at which to plot the b-plane has a relatively small effect on the magnitude of the coordinates. The change of sign of the ξ coordinate is still present in this case, as it is tied to the crossing of the ecliptic by the NEO.

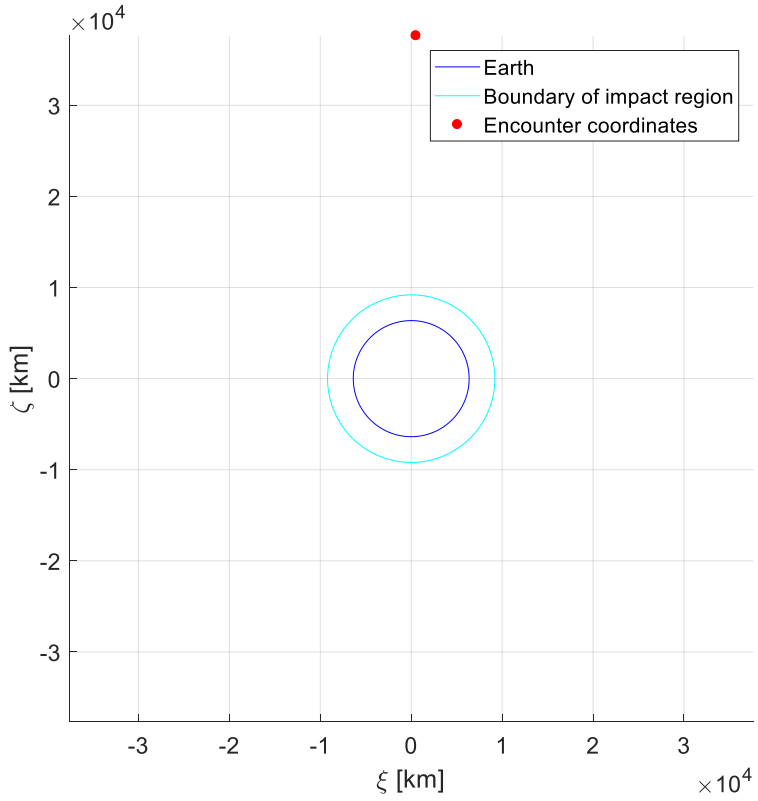

Figure 2.17: Case B.2 - b-plane representation of the close approach at the first entrance in the nominal SOI.

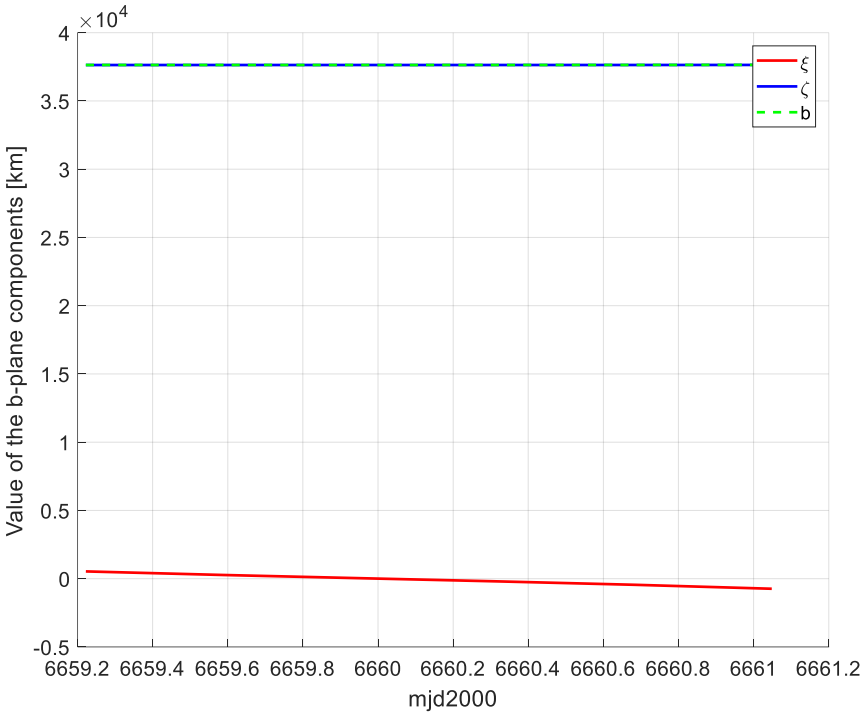

Figure 2.18: Case B.2 - b-plane components evolution.

2.7.3.4 *Case B.3*

Case B.3 inverts the concept of case B.2 replacing the delay with an advance of $10\ \mathrm{min}$ in the encounter: the NEO reaches the crossing before the Earth does, once again replacing the impact with a close approach. As in the previous cases, the effect of the timing of the projection on the b-plane is relatively limited. The most notable difference from the previous case stems from the opposite sign of the ζ coordinate of the encounter. This effect is in accordance with the definition of the b-plane axes in section 2.2 [21]. As in the previous case, the projection of the NEO coordinates along the ξ-axis features a sign inversion.

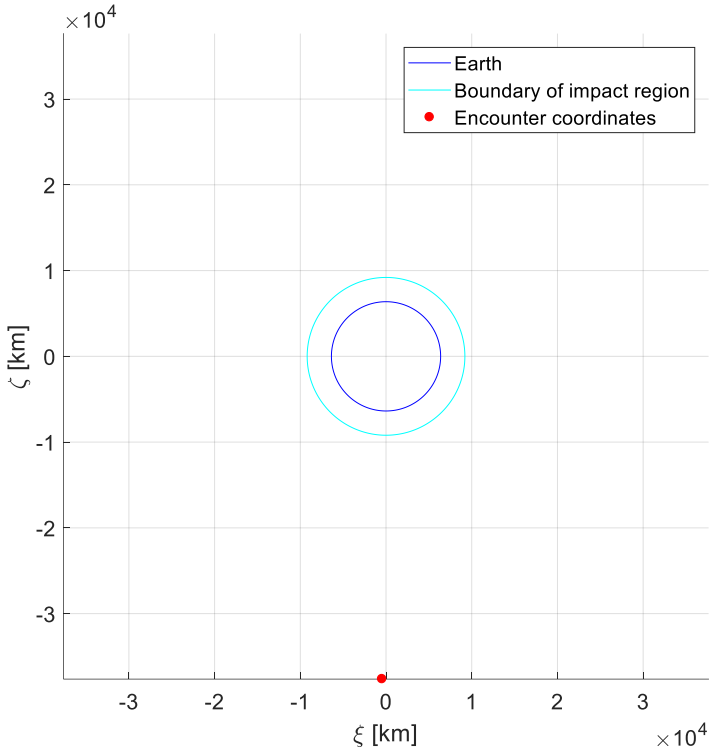

Figure 2.19: Case B.3 - b-plane representation of the close approach at the first entrance in the nominal SOI.

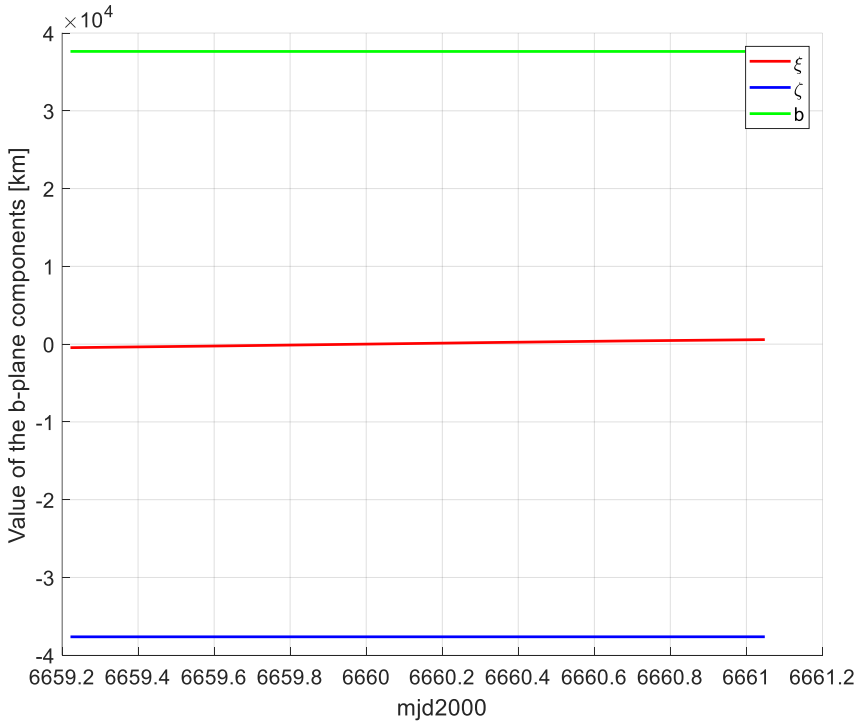

Figure 2.20: Case B.3 - b-plane components evolution.

2.8 Numerical Keyhole Definition

This section will show the effect of the passage of a NEO through a keyhole during a fly-by of the Earth. As some hypotheses made in defining the resonance circles and the relative keyholes in the framework of Öpik's theory have been relaxed, namely the circularity of the Earth's orbit and the coincidence of the NEO and the planet during the encounter with respect to the Sun, the effective keyholes have been computed numerically through the following algorithm developed in this work and inspired on what has already been done by Bourdoux [21]:

1. The nominal encounter between the asteroid and the planet is recorded (a two-body propagation is assumed for both the Earth and the NEO), based on the entrance of the asteroid in the planet's SOI
2. An array of values of ζ is explored to analyse the period of the corresponding orbit after the fly-by (modelled according to Valsecchi's extension of Öpik's theory, see section 2.5), while keeping the value of the ξ coordinate constant and equal to its nominal value (corresponding to a shift in time of the encounter); in other words, the post-encounter orbit of a series of synthetic points describing a segment parallel to the ζ-axis and passing through the nominal encounter conditions is analysed to determine whether or not they will lead to an encounter
3. If the resulting semi-major axis corresponds to a value of the period required for a resonant return after h periods of the NEO and k periods of the Earth, given a certain tolerance, the value of ζ is recorded as being part of the (h, k) keyhole

The reason for which the position and size of the keyhole is computed along the ζ direction stems for the knowledge that we have regarding the orbital parameters of the NEOs. In practice, small differences in the semi-major axis of an asteroid can have a very significant effect on the timing of an encounter when the coordinates are propagated for a long integration time [21]. Furthermore, as will be illustrated in chapter 3, in most cases, the deflection along the ζ-axis dominates over the one along the ξ-axis.

2.8.1 Extension of the Algorithm to the ξ-Axis

Despite the statement made at the end of the previous section (2.8), analysing the geometry of the keyholes along the ξ-direction can help describing the difference between the position of the analytical resonant circles and those computed numerically.

To this end, a "Monte Carlo"-like approach has been implemented in this thesis to analyse the post-encounter semi-major axis of a set of points in the area surrounding the nominal conditions of an encounter on the b-plane both in the ξ and in the ζ direction, practically extending the algorithm presented in section 2.8 to define keyholes numerically to the ξ-axis.

In particular, the following example features the September 2095 encounter of asteroid 2010 RF_{12} with the Earth (the conditions of the nominal encounter differ from the ones related to the actual ephemerides values taken from NASA's SPICE toolkit [30] as the pre-encounter propagation is carried out considering a two-body framework for both the NEO and the planet) and considers a circular area with a radius of $10000\ \mathrm{km}$ centred in the nominal encounter conditions on the b-plane. The sampling of the area is based on a radial step of $1\ \mathrm{km}$ and an angular discretisation with a point every $0.1°$; a qualitative scheme of the discretisation can be seen in Figure 2.21.

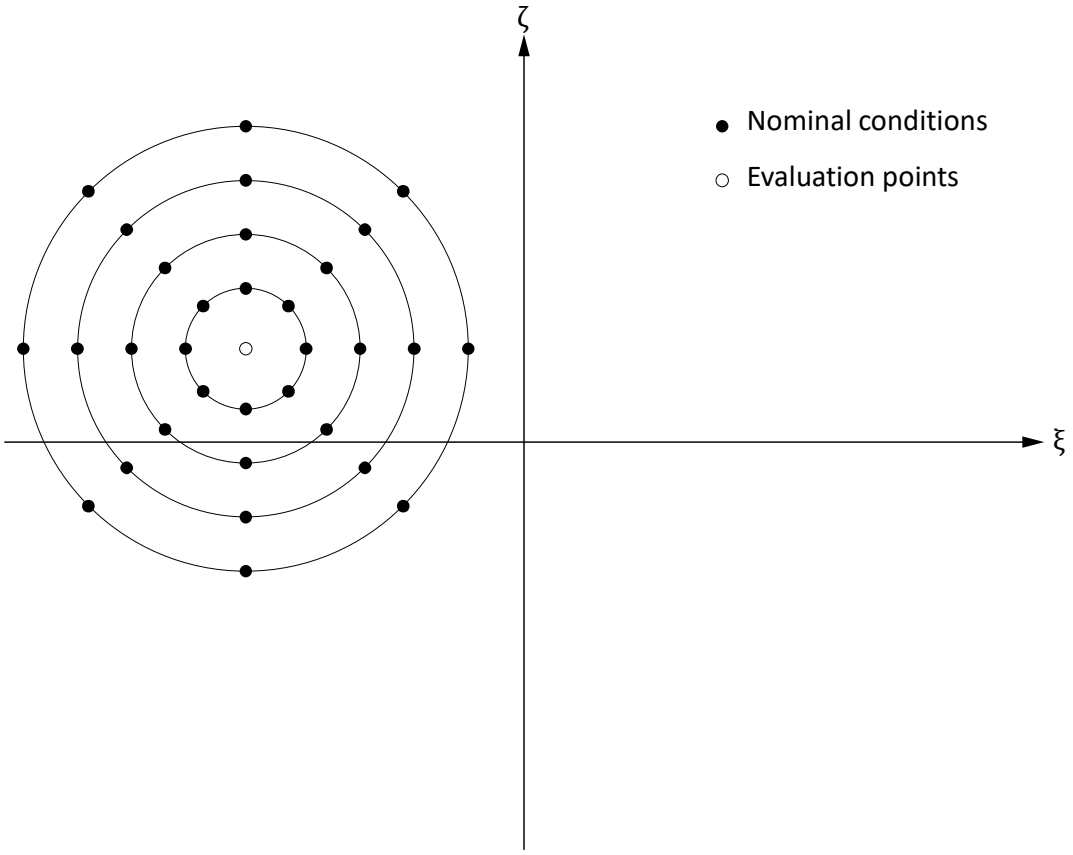

Figure 2.21: "Monte Carlo"-like method evaluation points qualitative scheme.

The tolerance selected for the return time difference in this application is $1\ \mathrm{h}$. Figure 2.22 and Figure 2.23 portray both the analytically-computed resonant circles (in the form of coloured lines ranging from dark blue to yellow, which have not been numbered to improve figure clarity) and the numerically-computed keyholes (in brown) relative to the nominal encounter conditions (also present in the figures as a purple asterisk). From Figure 2.23 it is apparent how, despite the fact that the analytical resonant circles and the numerical keyholes differ significantly in their positions (which is to be expected, given the different assumptions upon which they are based), the numerical keyholes retain the shape of the resonant circles even though they are based on different hypotheses, as stated in section 2.8.

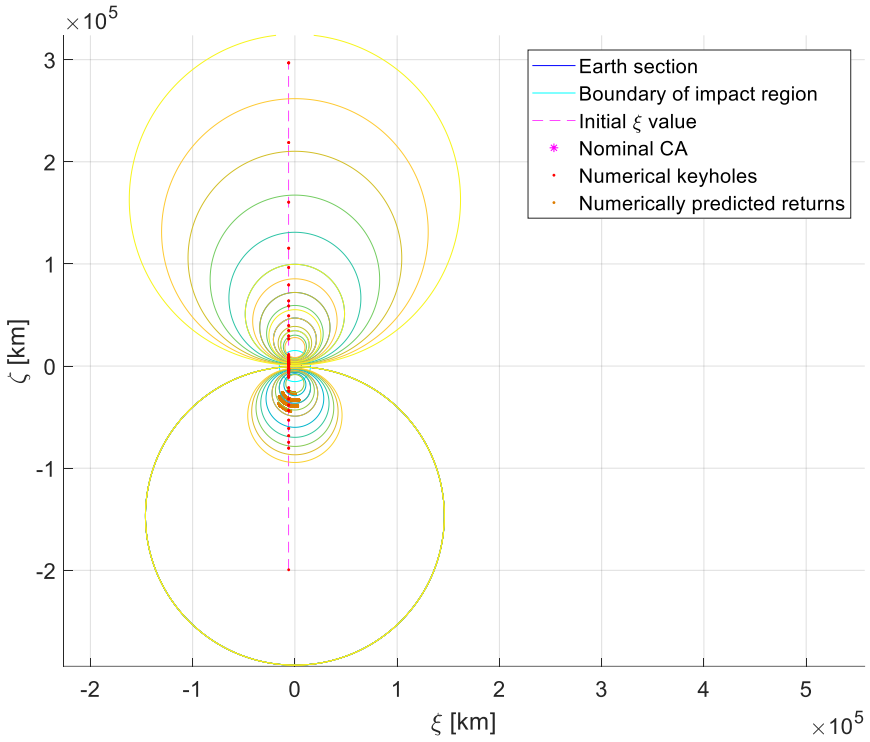

Figure 2.22: B-plane representation of the encounter between 2010 RF_{12} and the Earth.

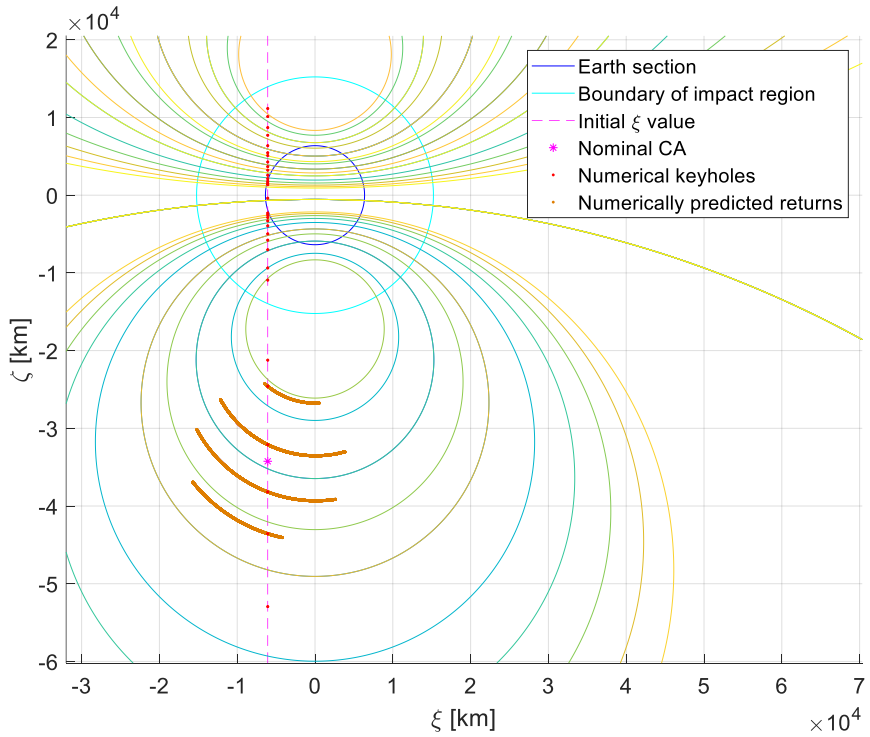

Figure 2.23: Zoom-in of Figure 2.22 focusing on the area featuring the analysed returns.

2.9 Effect of the Keyholes

This example analyses the encounter between asteroid 2010 RF_{12} and the Earth estimated around the 6th of September 2095. The choice of the NEO is based on 2010 RF_{12} currently having the highest probability of colliding with the Earth amongst the known PHAs, estimated around 6% for the selected encounter [5]. If it were to take place, the impact would liberate an energy of the order of magnitude the Hiroshima bomb [31].

The conditions of the nominal encounter differ from the ones that would be obtained relying on the SPICE ephemerides [30] values, as the pre-encounter propagation is carried out considering a two-body problem framework for both the NEO and the planet. Table 1 shows the Keplerian parameters assumed for this example (where $\mathrm{mjd2000}$ is the modified Julian date).

	$a\ [km]$	e	$i\ [rad]$	$\Omega\ [rad]$	$\omega\ [rad]$	$\theta\ [rad]$	$\mathrm{mjd2000}$
Earth	$1.4972 \cdot 10^8$	0.0164	$2.0800 \cdot 10^{-4}$	3.0488	4.9940	4.1319	$3.4942 \cdot 10^4$
2010 RF_{12}	$1.5739 \cdot 10^8$	0.1881	0.0160	2.8365	4.6594	4.6795	$3.4942 \cdot 10^4$

Table 1: Keplerian parameters of the Earth and the asteroid assumed for this example.

Three new initial synthetic conditions corresponding to different values of ζ on the pre-encounter b-plane are obtained by keeping the other quantities defining the b-plane unchanged (U, Θ, ϕ and ξ) with respect to the nominal encounter:

1. Centre of keyhole $(5,4)$, see Figure 2.24 and Figure 2.25 (red asterisk symbol)
2. Middle point between keyhole $(5,4)$ and keyhole $(6,5)$, see Figure 2.24 and Figure 2.25 (blue asterisk symbol)
3. Centre of keyhole $(6,5)$, see Figure 2.24 and Figure 2.25 (green asterisk symbol)

From Figure 2.24 and Figure 2.25 it is apparent how the difference between the analytical keyholes and those computed numerically is very significant, rendering this step necessary in order to obtain results leading to actual returns. This is especially true for the NEO deviation application (see sections 4.2 and 4.3), where the targets for the deviation must be such that a resonant return is avoided. The figures portray the analytical resonant circles as coloured lines (ranging from dark blue to yellow, as already done in section 2.8.1, only a subset of which is present in Figure 2.25) and the selected new synthetic initial conditions described above.

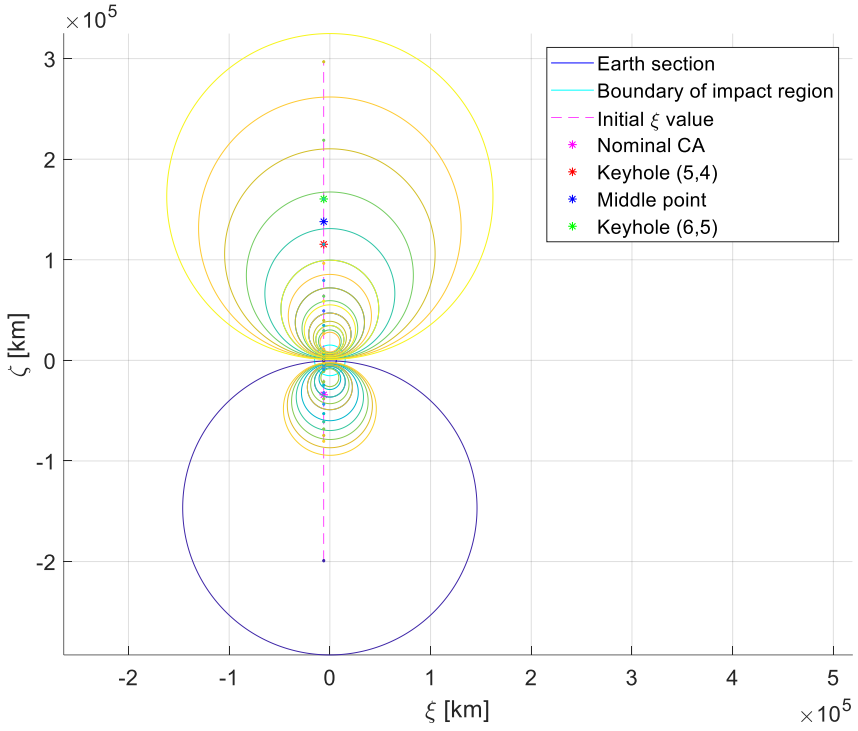

Figure 2.24: B-plane of the encounter between 2010 RF_{12} and the Earth showing the new synthetic initial conditions.

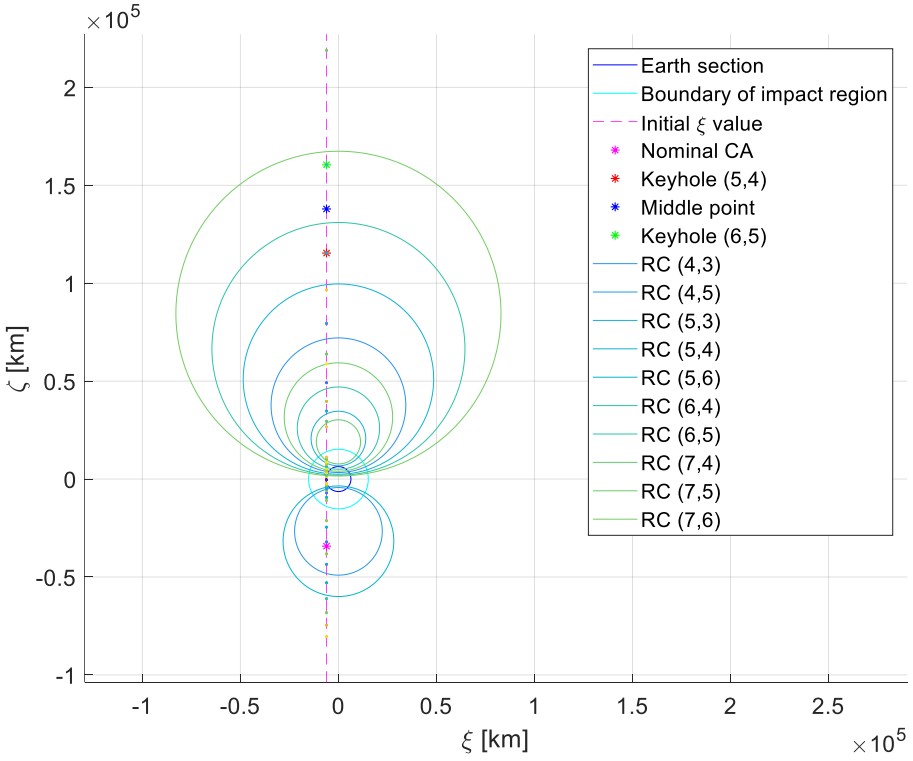

Figure 2.25: Zoom-in of Figure 2.24 showing only the neighbouring resonant circles.

The propagation of the synthetic initial conditions described in the previous figures is displayed in Figure 2.26 and Figure 2.27 (which more closely analyses the return conditions). As expected from the initial conditions, the encounters crossing the keyholes (red and green asterisk symbols in Figure 2.24 and Figure 2.25) feature returns after the corresponding numbers of periods of the asteroid and the Earth, whereas the point halfway between the considered keyholes (blue asterisk in Figure 2.24 and Figure 2.25) does not feature a return in the considered time-frame (based on the maximum resonant return considered when calculating the position and size of the keyholes). This condition is therefore *desirable* for the deviation of an incoming asteroid, as will be discussed in section 4.2.

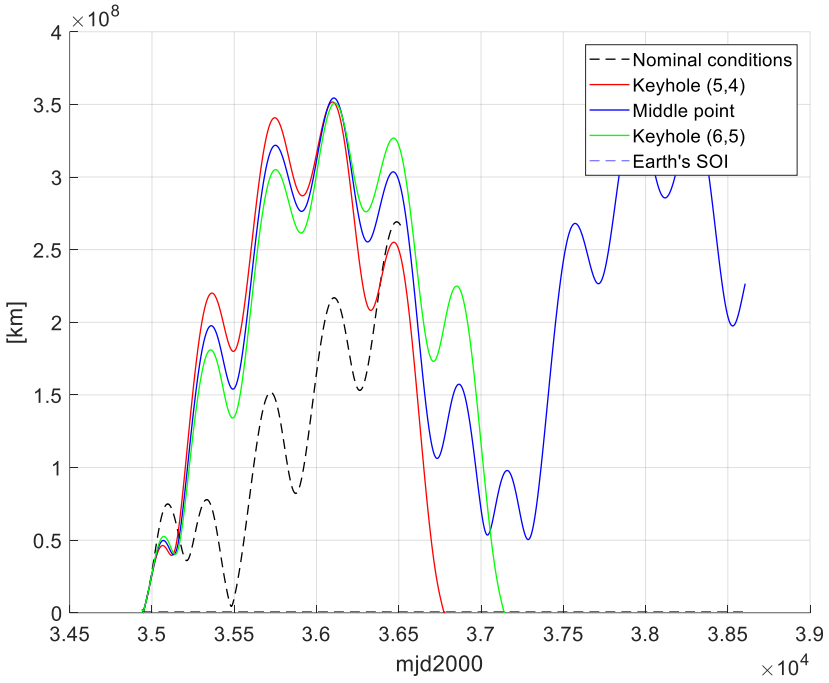

Figure 2.26: Distance between 2010 RF_{12} and the Earth for the considered initial conditions.

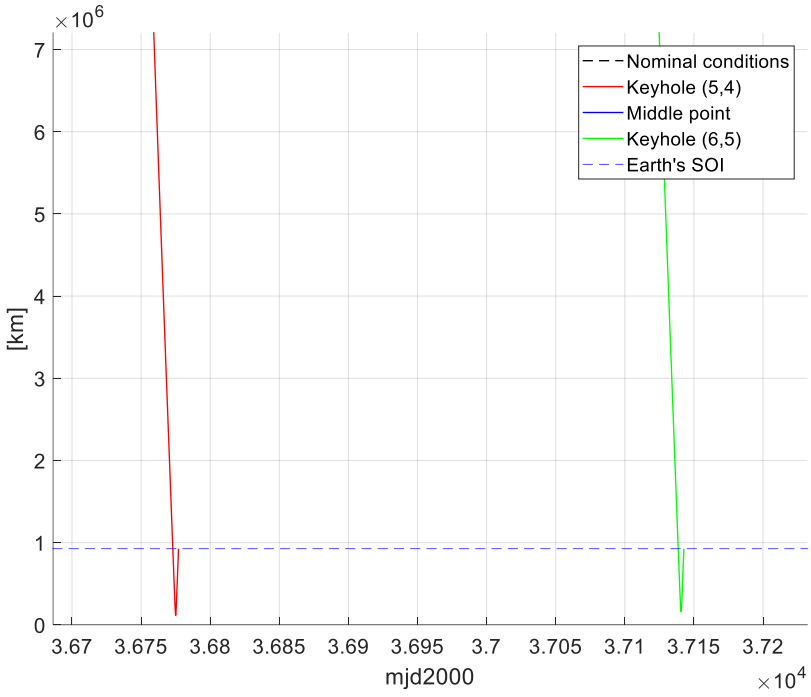

Figure 2.27: Zoom-in of Figure 2.26 showing the resonant returns corresponding to the keyholes.

It should be noted that the propagation of the conditions deriving from the keyholes is performed until their expected relative returns, as the second flyby would not be correctly represented in the two-body problem framework, and that the middle point conditions are only propagated for the number of years corresponding to the maximum considered circle ($10y$ in this case), as the point could correspond to a later keyhole (not drawn on the b-plane). The latter limitation could be counteracted by considering more keyholes, which would however be further from the real conditions due to the approximate nature of the propagation, as stated in chapter 2.6.1.1.

2.9.1 Validity of the Approach

We need to consider that the analysis performed so far is conducted in the linked-conics method of the Restricted Two-Body Problem (R2BP). In reality, NEOs' orbits need to be propagated in the n-Body Problem (nBP) considering the presence of the Solar System planets. The example in this section features an n-body propagation of the NEO's coordinates (considering all of the Solar System's planets) after the encounter with the planet; furthermore, the Earth's coordinates are obtained through SPICE ephemerides [30], as well as the NEO's up to the encounter.

This more accurate modelling of the effects of the encounter clearly highlights the limitations of a more complex model: the anticipated return is not obtained when considering the n-body propagation after a single year (the

keyholes are computed in the R2BP), while the R2BP return is affected by the non-perfectly-Keplerian motion of the Earth resulting from the ephemerides, as is evident from Figure 2.30. Nevertheless, the proposed simplified approach can be considered as a viable first approximation for the real case, as the results of the R2BP approximation are indicative of the real situation on the short period (up to $10y$ approximatively, as stated in section 2.6.1.1).

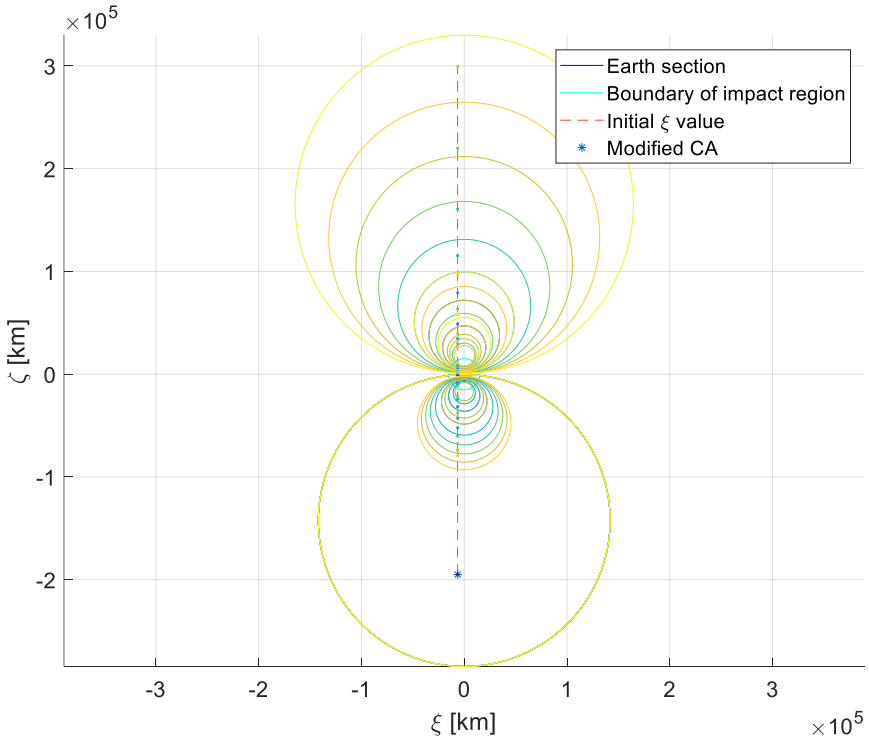

Figure 2.28: Ephemerides-derived b-plane for 2010 RF_{12}'s encounter with the Earth on 06/09/2095.

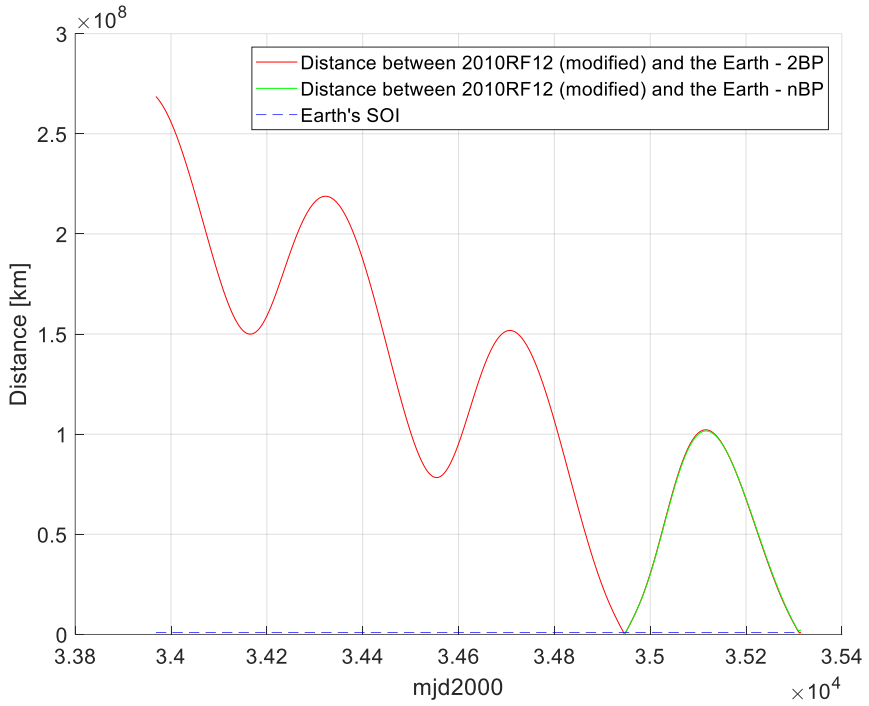

Figure 2.29: Distance of 2010 RF12 from the Earth considering both R2BP and nBP approaches.

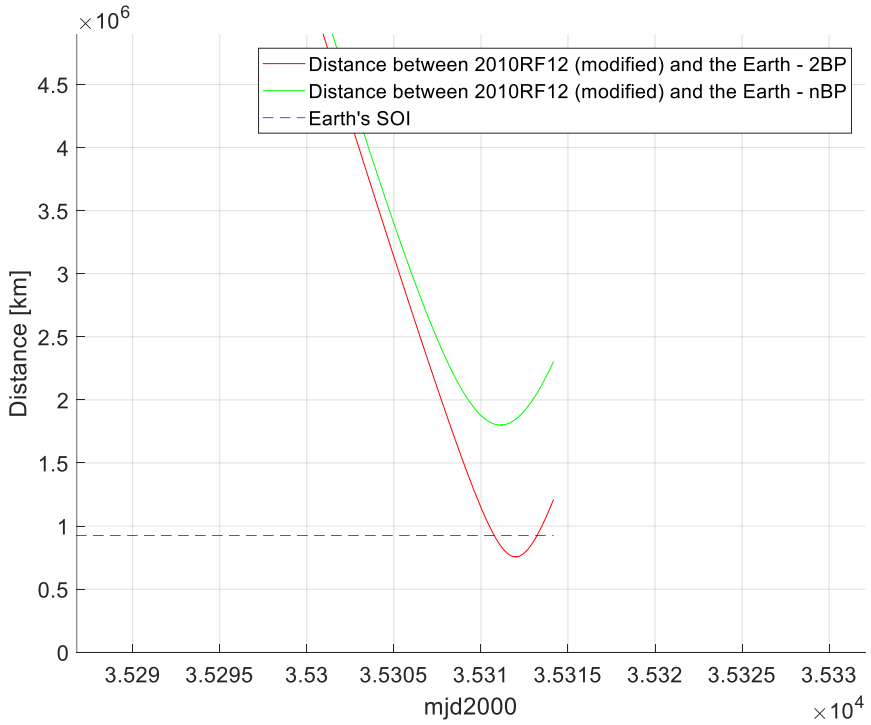

Figure 2.30: Zoom-in of Figure 2.29 showing the differences in the returns of both types of propagation after $1\ y$.

3 Near-Earth Object Deflection

The main topic of this chapter will be the description of the modelling of the deflection manoeuvre and the resulting displacement at the MOID. Further along the chapter, the maximisation of the deflection effect will be discussed considering different objectives, both purely geometrical and concerning the b-plane properties. Finally some results relative to the proposed techniques will be presented to corroborate the theoretical results.

The analytical correlation between the displacement on the b-plane, both generic and along each axis, as well as the application of the maximisation technique to the aformentioned correlation are innovative results based on the work of Vasile and Colombo [22] and developed during the thesis work.

3.1 Deflection Model

The objective of the deviation action is to cause a displacement of the NEO at the time of the close approach through an impulsive manoeuvre at a time t_d. The first step in defining the required optimisation strategy is to detail the equations applied to the modelling of the deflection. The approach used in this part of the work was proposed by Vasile and Colombo [22] and is here expanded to consider the projection of the deflection on the b-plane.

3.1.1 Proximal Motion Equations

As the perturbed orbit can be considered proximal to the original one, the position of the NEO after the deviation in the radial, transversal and perpendicular-to-the-orbit-plane directions (δs_r, δs_θ and δs_h) can be computed through the use of the proximal motion equations [22]

$$\delta s_r \cong \frac{r_{MOID}}{a}\delta a + \frac{ae\sin\theta_{MOID}}{\eta}\delta M - a\cos\theta_{MOID}\,\delta e$$

$$\delta s_\theta \cong \frac{r_{MOID}}{\eta^3}(1+e\cos\theta_{MOID})^2\delta M + r_{MOID}\delta\omega + \frac{r_{MOID}\sin\theta_{MOID}}{\eta^2}(2+e\cos\theta_{MOID})\delta e + r_{MOID}\cos i\,\delta\Omega$$

$$\delta s_h \cong r_{MOID}(\sin\theta^*{}_{MOID}\,\delta i - \cos\theta^*{}_{MOID}\sin i\,\delta\Omega)$$

Equation 3.1

where r_{MOID} is the distance of the NEO from the Earth at the MOID, $\theta^*{}_{MOID} = \theta_{MOID} + \omega$ is the argument of latitude of the NEO at the MOID and $\eta = \sqrt{1-e^2}$. The other quantities present in Equation 3.1 are the orbital parameters of the NEO, a is the semi-major axis, e is the eccentricity, i is the inclination, Ω is the right-ascension

of the ascending node, ω is the argument of the periapsis and M is the mean anomaly, and the variation of such parameters δa, δe, δi, $\delta\Omega$, $\delta\omega$ and δM.

3.1.2 Gauss Planetary Equations

The variation of orbital parameters can be determined through the Gauss planetary equations if an instantaneous perturbation of the NEO velocity vector (expressed in the tangent, normal and perpendicular-to-the-orbit-plane directions; δv_t, δv_n and δv_h in the following equations) is considered. The aforementioned correlation is expressed by the following formulas derived for finite differences [8]:

$$\delta a = \frac{2a^2 v_d}{\mu}\delta v_t$$

$$\delta e = \frac{1}{v_d}\left[2(e+\cos\theta_d)\delta v_t - \frac{r_d}{a}\sin\theta_d\,\delta v_n\right]$$

$$\delta i = \frac{r_d\cos\theta^*{}_d}{h}\delta v_h$$

$$\delta\Omega = \frac{r_d\sin\theta^*{}_d}{h\sin i}\delta v_h$$

$$\delta\omega = \frac{1}{ev_d}\left[2\sin\theta_d\,\delta v_t + \left(2e+\frac{r_d}{a}\cos\theta_d\right)\delta v_n\right] - \frac{r_d\sin\theta^*{}_d\cos i}{h\sin i}\delta v_h$$

$$\delta M_{t_d} = -\frac{b}{eav_d}\left[2\left(1+\frac{e^2 r_d}{p}\right)\sin\theta_d\,\delta v_t + \frac{r_d}{a}\cos\theta_d\,\delta v_n\right]$$

Equation 3.2

where the quantities denoted by the subscript d are computed at the deviation point.

As δM_{t_d} does not take the variation of the mean motion δn into account, but rather only considers the instantaneous change of geometry at time t_d; the following term needs to be added [22]

$$\delta M_n = \delta n\Delta t = \left(\sqrt{\frac{\mu}{a^3}} - \sqrt{\frac{\mu}{(a+\delta a)^3}}\right)(t_{MOID} - t_n) = -\frac{3}{2}\frac{\sqrt{\mu}}{a^{5/2}}\Delta t\delta a$$

$$\delta M = \delta M_{t_d} + \delta M_n = -\frac{b}{eav}\left[2\left(1+\frac{e^2 r}{p}\right)\sin\theta_d\,\delta v_t + \frac{r}{a}\cos\theta_d\,\delta v_n\right] - \frac{3}{2}\frac{\sqrt{\mu}}{a^{5/2}}\Delta t\delta a$$

Given the vector scheme in Figure 3.1, the aim of the problem becomes the maximisation of the objective function:

$$J = (\Delta s_r + \delta s_r)^2 + (\Delta s_\theta + \delta s_\theta)^2 + (\Delta s_h + \delta s_h)^2$$

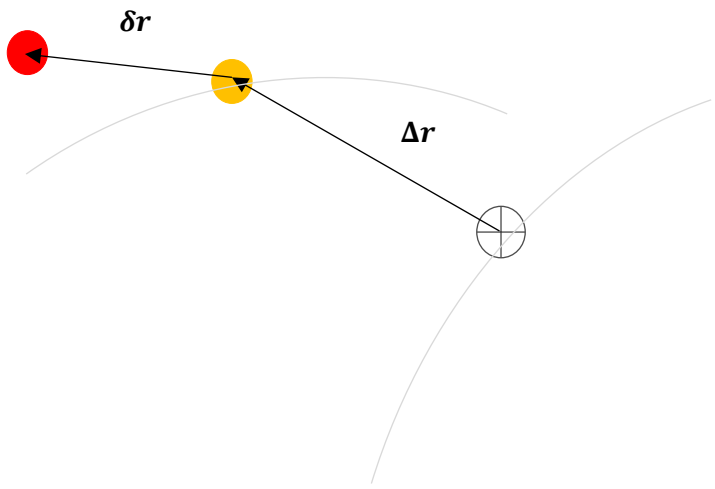

Figure 3.1: Distance vectors at the MOID (Earth in green, non-deviated NEO in orange and deviated NEO in red)

This method provides a relatively simple and computationally inexpensive strategy to determine the effect of a deviation [22].

By combining the proximal motion equations (Equation 3.1) and the Gauss planetary ones (Equation 3.2), the following matrix formulation linking the $\boldsymbol{\delta v}$ at the deflection point to the $\boldsymbol{\delta r}$ at the MOID can be obtained [22]:

$$\begin{cases} \boldsymbol{\delta r}_{MOID} = \boldsymbol{A}_{MOID}\boldsymbol{\delta\alpha}_d \\ \boldsymbol{\delta\alpha}_d = \boldsymbol{G}_d\boldsymbol{\delta v}_d \end{cases} \Longrightarrow \boldsymbol{\delta r}_{MOID} = \boldsymbol{A}_{MOID}\boldsymbol{G}_d\boldsymbol{\delta v}_d = \boldsymbol{T}\boldsymbol{\delta v}_d$$

Equation 3.3

$$\boldsymbol{A}_{MOID}{}^T = \begin{bmatrix} \frac{r_{MOID}}{a} - \frac{3}{2}\frac{e\sin\theta_{MOID}}{\eta}\frac{\sqrt{\mu}}{a^{3/2}}\Delta t & -\frac{3}{2}\frac{r_{MOID}}{\eta^3}(1+e\cos\theta_{MOID})^2\frac{\sqrt{\mu}}{a^{5/2}}\Delta t & 0 \\ -a\cos\theta_{MOID} & \frac{r_{MOID}\sin\theta_{MOID}}{\eta^2}(2+e\cos\theta_{MOID}) & 0 \\ 0 & 0 & r_{MOID}\sin\theta^*{}_{MOID} \\ 0 & r_{MOID}\cos i & -r_{MOID}\cos\theta^*{}_{MOID}\sin i \\ 0 & r_{MOID} & 0 \\ \frac{ae\sin\theta_{MOID}}{\eta} & \frac{r_{MOID}}{\eta^3}(1+e\cos\theta_{MOID})^2 & 0 \end{bmatrix}$$

$$\boldsymbol{G}_d = \begin{bmatrix} \frac{2a^2 v_d}{\mu} & 0 & 0 \\ \frac{2}{v}(e+\cos\theta_d) & -\frac{r}{a v_d}\sin\theta_d & 0 \\ 0 & 0 & \frac{r_d \cos\theta^*{}_d}{h} \\ 0 & 0 & \frac{r_d \sin\theta^*{}_d}{h \sin i} \\ \frac{2\sin\theta_d}{e v_d} & \frac{2e + {}^{r_d}/_{a}\cos\theta_d}{e v_d} & -\frac{r_d \sin\theta^*{}_d \cos i}{h \sin i} \\ -\frac{2b}{e a v_d}\left(1+\frac{e^2 r_d}{p}\right)\sin\theta_d & -\frac{b}{e a v_d}\frac{r_d}{a}\cos\theta_d & 0 \end{bmatrix}$$

where $\boldsymbol{\delta\alpha}_d = \{\delta a \quad \delta e \quad \delta i \quad \delta\Omega \quad \delta\omega \quad \delta M_{t_d}\}^T$.

It should be noted that the equations presented in this formulation are consistent with a keplerian motion of the involved bodies along elliptical and quasi-circular orbits [8].

Even though the deviation is evaluated at the MOID, the formulas presented in this section (and applied in the following sections) remain valid in the case the encounter is not correctly phased and therefore does not take place at the exact MOID; this is due to the fact that the encounter is assumed to take place at the MOID in the present formulation, but no related restriction is applied to the formulas (i.e. the MOID represents the close-encounter conditions).

3.2 Maximisation of the Deflection

3.2.1 Geometric Deviation

As proposed and applied by Colombo [8] to NEO deflection missions, a convenient formulation to maximise the relative deviation $\|\boldsymbol{\delta r}_{MOID}\|$ is based on maximising the quadratic form $\boldsymbol{T}^T\boldsymbol{T}$ associated with Equation 3.3. This can be achieved by choosing an impulse velocity vector $\boldsymbol{\delta v}_d$ parallel to the direction of the eigenvector of the matrix $\boldsymbol{T}^T\boldsymbol{T}$ conjugated to its maximum eigenvalue. This method only constrains the direction of $\boldsymbol{\delta v}_d$ while its sign can be chosen to determine the direction of the corresponding displacement [22]. The sign is therefore selected such that the deviation increases the distance of the asteroid from the Earth at the time of the encounter.

3.2.2 Deviation on the b-Plane

The method applied to the maximisation of the geometric deviation is extended in this thesis to maximise both the deviation of the impact parameter $\|\boldsymbol{\delta b}_{MOID}\|$ and the single components on the b-plane $\|\boldsymbol{\delta\xi}_{MOID}\|$ and

$\|\boldsymbol{\delta\zeta}_{MOID}\|$. In order to use the previously described procedure, the quantities must be taken as vectors in space and expressed as the product of a matrix and the impulse velocity vector.

The effectiveness of these methods is later proven in section 3.3 through a comparison with a numerical maximisation.

3.2.2.1 *Deviated Impact Parameter*

Let us consider the achieved deviation in the impact parameter b on the b-plane. To do so, the first step must be the computation of the deflection vector in the b-plane:

$$\boldsymbol{\delta b}_{MOID} = \boldsymbol{\delta r}_{MOID} - \left(\boldsymbol{\delta r}_{MOID} \cdot \boldsymbol{e_\eta}\right)\boldsymbol{e_\eta}$$

Equation 3.4

where $\boldsymbol{e_\eta}$ is the versor of the η-axis of the b-plane and $\boldsymbol{\delta b}_{MOID}$ is a vector identifying δb_{MOID}, the deviation on the b-plane as represented in Figure 3.2.

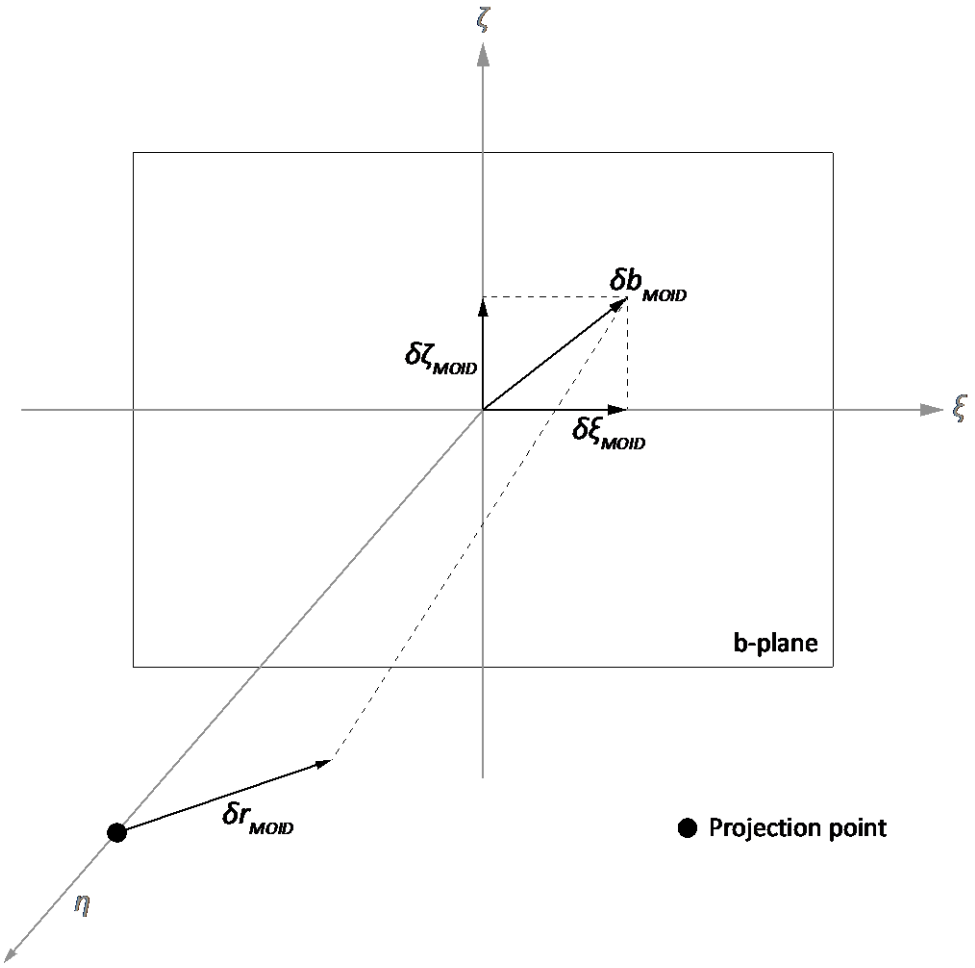

Figure 3.2: Deviation components on the b-plane.

Considering the vector triple product identity, we have

$$\boldsymbol{e_\eta} \times (\boldsymbol{\delta r}_{MOID} \times \boldsymbol{e_\eta}) = (\boldsymbol{e_\eta} \cdot \boldsymbol{e_\eta})\boldsymbol{\delta r}_{MOID} - (\boldsymbol{\delta r}_{MOID} \cdot \boldsymbol{e_\eta})\boldsymbol{e_\eta} = \boldsymbol{\delta r}_{MOID} - (\boldsymbol{\delta r}_{MOID} \cdot \boldsymbol{e_\eta})\boldsymbol{e_\eta}$$

We can therefore re-write Equation 3.4 as

$$\boldsymbol{\delta b}_{MOID} = \boldsymbol{\delta r}_{MOID} - \boldsymbol{\delta r}_{MOID} + \boldsymbol{e_\eta} \times (\boldsymbol{\delta r}_{MOID} \times \boldsymbol{e_\eta}) = \boldsymbol{e_\eta} \times (\boldsymbol{\delta r}_{MOID} \times \boldsymbol{e_\eta})$$

The previous expression can also be written in the compact form

$$\boldsymbol{\delta b}_{MOID} = \boldsymbol{M}_{\boldsymbol{\delta b}} \boldsymbol{\delta r}_{MOID}$$

$$\boldsymbol{M}_{\boldsymbol{\delta b}} = \begin{bmatrix} {e_{\eta_2}}^2 + {e_{\eta_3}}^2 & -e_{\eta_1} e_{\eta_2} & -e_{\eta_1} e_{\eta_3} \\ -e_{\eta_1} e_{\eta_2} & {e_{\eta_1}}^2 + {e_{\eta_3}}^2 & -e_{\eta_2} e_{\eta_3} \\ -e_{\eta_1} e_{\eta_3} & -e_{\eta_2} e_{\eta_3} & {e_{\eta_1}}^2 + {e_{\eta_2}}^2 \end{bmatrix}$$

where e_{η_i} are the components of the versor.

The deviation on the b-plane $\boldsymbol{\delta b}_{MOID}$ can now be mapped back to the deviation manoeuvre $\boldsymbol{\delta v}_d$:

$$\boldsymbol{\delta b}_{MOID} = \boldsymbol{M}_{\boldsymbol{\delta b}} \boldsymbol{T} \boldsymbol{\delta v}_d = \boldsymbol{T}_{\boldsymbol{\delta b}} \boldsymbol{\delta v}_d$$

Equation 3.5

We have obtained an analytical formulation to describe the deviation on the b-plane at the MOID in function of the deflection action, which can be used to obtain the direction of the maximum deviation on the b-plane through the optimisation technique of section 3.2.1. This is the first innovative result continuing Vasile and Colombo's work [22], which relied on a numerical computation of δb_{MOID}.

3.2.2.2 *Components on the B-Plane (ξ and ζ)*

Let us now compute the single components of $\boldsymbol{\delta b}_{MOID}$ (from Equation 3.5) on the b-plane:

$$\boldsymbol{\delta \xi}_{MOID} = \boldsymbol{\delta b}_{MOID} - (\boldsymbol{\delta b}_{MOID} \cdot \boldsymbol{e_\zeta})\boldsymbol{e_\zeta}$$

$$\boldsymbol{\delta \zeta}_{MOID} = \boldsymbol{\delta b}_{MOID} - (\boldsymbol{\delta b}_{MOID} \cdot \boldsymbol{e_\xi})\boldsymbol{e_\xi}$$

where $\boldsymbol{e_\xi}$ and $\boldsymbol{e_\zeta}$ are the versors of the ξ and ζ axes of the b-plane respectively.

Through the same procedure applied for the impact parameter in section 3.2.2.1, we can write

$$\boldsymbol{\delta \xi}_{MOID} = \boldsymbol{M}_{\boldsymbol{\delta \xi}} \boldsymbol{\delta b}_{MOID}$$

$$\boldsymbol{\delta \zeta}_{MOID} = \boldsymbol{M}_{\boldsymbol{\delta \zeta}} \boldsymbol{\delta b}_{MOID}$$

$\boldsymbol{\delta\xi}_{MOID}$ and $\boldsymbol{\delta\zeta}_{MOID}$ are the vectors representing the deflection along the respective axes on the b-plane, as seen in Figure 3.2.

$$\boldsymbol{M}_{\boldsymbol{\delta\xi}} = \begin{bmatrix} {e_{\zeta_2}}^2 + {e_{\zeta_3}}^2 & -e_{\zeta_1}e_{\zeta_2} & -e_{\zeta_1}e_{\zeta_3} \\ -e_{\zeta_1}e_{\zeta_2} & {e_{\zeta_1}}^2 + {e_{\zeta_3}}^2 & -e_{\zeta_2}e_{\zeta_3} \\ -e_{\zeta_1}e_{\zeta_3} & -e_{\zeta_2}e_{\zeta_3} & {e_{\zeta_1}}^2 + {e_{\zeta_2}}^2 \end{bmatrix}$$

$$\boldsymbol{M}_{\boldsymbol{\delta\zeta}} = \begin{bmatrix} {e_{\xi_2}}^2 + {e_{\xi_3}}^2 & -e_{\xi_1}e_{\xi_2} & -e_{\xi_1}e_{\xi_3} \\ -e_{\xi_1}e_{\xi_2} & {e_{\xi_1}}^2 + {e_{\xi_3}}^2 & -e_{\xi_2}e_{\xi_3} \\ -e_{\xi_1}e_{\xi_3} & -e_{\xi_2}e_{\xi_3} & {e_{\xi_1}}^2 + {e_{\xi_2}}^2 \end{bmatrix}$$

where e_{ξ_i} and e_{ζ_i} are the components of the respective versors (see Figure 3.2).

The components of $\boldsymbol{\delta b}_{MOID}$ in the b-plane can therefore be written in a compact form as:

$$\boldsymbol{\delta\xi}_{MOID} = \boldsymbol{M}_{\boldsymbol{\delta\xi}}\boldsymbol{T}_{\boldsymbol{\delta b}}\boldsymbol{\delta v}_d = \boldsymbol{M}_{\boldsymbol{\delta\xi}}\boldsymbol{M}_{\boldsymbol{\delta b}}\boldsymbol{T}\boldsymbol{\delta v}_d = \boldsymbol{T}_{\boldsymbol{\delta\xi}}\boldsymbol{\delta v}_d$$

$$\boldsymbol{\delta\zeta}_{MOID} = \boldsymbol{M}_{\boldsymbol{\delta\zeta}}\boldsymbol{T}_{\boldsymbol{\delta b}}\boldsymbol{\delta v}_d = \boldsymbol{M}_{\boldsymbol{\delta\zeta}}\boldsymbol{M}_{\boldsymbol{\delta b}}\boldsymbol{T}\boldsymbol{\delta v}_d = \boldsymbol{T}_{\boldsymbol{\delta\zeta}}\boldsymbol{\delta v}_d$$

Equation 3.6

3.2.3 Maximisation of the Components in the B-Plane

The same method used by Colombo [8] to maximise the relative deviation $\|\boldsymbol{\delta r}_{MOID}\|$ based on maximizing the quadratic form $\boldsymbol{T}^{\boldsymbol{T}}\boldsymbol{T}$ associated with Equation 3.3 can now be extended to maximise $\|\boldsymbol{\delta b}_{MOID}\|$, $\|\boldsymbol{\delta\xi}_{MOID}\|$ or $\|\boldsymbol{\delta\zeta}_{MOID}\|$. This can be achieved by chosing an impulse velocity vector $\boldsymbol{\delta v}_d$ parallel to the direction of the eigenvector of the matrix $\boldsymbol{T_{sel}}^{\boldsymbol{T}}\boldsymbol{T_{sel}}$ (where $\boldsymbol{T_{sel}}$ is the matrix mapping the desired vector on the b-plane with the deflection action $\boldsymbol{\delta v}_d$, as described in sections 3.2.2.1 and 3.2.2.2) conjugated to its maximum eigenvalue. This method only constrains the direction of $\boldsymbol{\delta v}_d$ while its sign can be chosen to determine the direction of the corresponding displacement [22]. The sign is therefore selected such that the deviation increases the value of the selected coordinate (b, ξ or ζ) of the projection of the deflected encounter conditions on the b-plane.

Indeed, this method is used to compute the optimal direction of the deflection to be imparted to the asteroid as a function of the Δt time before the possible impact. Once the deflection direction has been defined, the magnitude of the velocity vector $\boldsymbol{\delta v}_d$ can be increased as much as possible to further deviate the NEO, but the optimal direction of deviation does not change.

3.3 Validation of the Eigenvector Method Extension

From this section forward, the indication of the point of application of the deflection manoeuvre and the conditions at which the deflection is observed (i.e. the "d" and "MOID" suffixes) will be omitted from the notation to provide a clearer explanation. The deflection is always to be considered as taking place in the deviation point and the resulting displacement as taking place at the encounter coordinates, as previously stated in section 3.1.

In this section, the results obtained by maximising the deviation of the different components on the b-plane explained in section 3.2.2 are compared with the outcomes of a classical numerical optimisation, performed with MATLAB®'s *fmincon* optimiser (an optimiser based on the "interior point" algorithm). The numerical maximisation problem is handled by maximising the equation correlating between the deflection velocity vector and the desired displacement component on the b-plane (Equation 3.5 or Equation 3.6) in function of the velocity vector $\boldsymbol{\delta v}_d$, which is taken as an array of unknown components constrained to have a unitary norm.

For example, in the case of the maximisation of δb, the function to maximise will be:

$$f = \boldsymbol{T}_{\boldsymbol{\delta b}} \boldsymbol{\delta v}_d$$

The result of this operation is therefore the direction of maximum displacement δb, $\delta\xi$ or $\delta\zeta$.

3.3.1 Comparisons Between the Analytical and the Numerical Methods

In this section, the analytical maximisation method illustrated in section 3.2.3 and its numerical counterpart defined above are implemented for the same conditions to prove their equivalence.

Apophis was chosen as the reference object to be deflected for this comparison. The directions of optimal deviation are computed over a time of up to $1200\,\mathrm{d}$ before the close-approach, with a step of $4\,\mathrm{d}$ and a magnitude of $\boldsymbol{\delta v}$ of $7\ \mathrm{m/s}$ is considered.

3.3.1.1 *Maximisation of the Impact Parameter Deviation (δb)*

Figure 3.3 portrays the effect of a deviation along a specific direction on the impact parameter. The tangent deviation result (the dashed dark-blue line), the normal deviation result (the dashed-dotted blue line) and the out-of-plane deviation result (the dotted blue line) are included for reference. The effects of the deflection in the direction of maximum δb deviation, computed according to the analytical and numerical optimisation techniques are represented by the red line and the dashed green line respectively.

Figure 3.4 depicts instead the weight of each of the components (i.e. the value of the components of the normalised vector) of the optimal δb deflection direction in the tangent, normal and out-of-plane (tnh) reference

frame (calculated in the position of the asteroid at the time of deflection), to characterise the direction of optimal deviation and compare the results returned by each method.

Finally, Table 2 features the computational time required for the present implementation of the two optimisation methods for comparison purposes.

This structure will be repeated for the deflection aimed at maximising $\delta\xi$ and $\delta\zeta$ in sections 3.3.1.2 and 3.3.1.3 respectively. A set of conclusions applicable to all three deviation targets will then be illustrated in section 3.3.2.

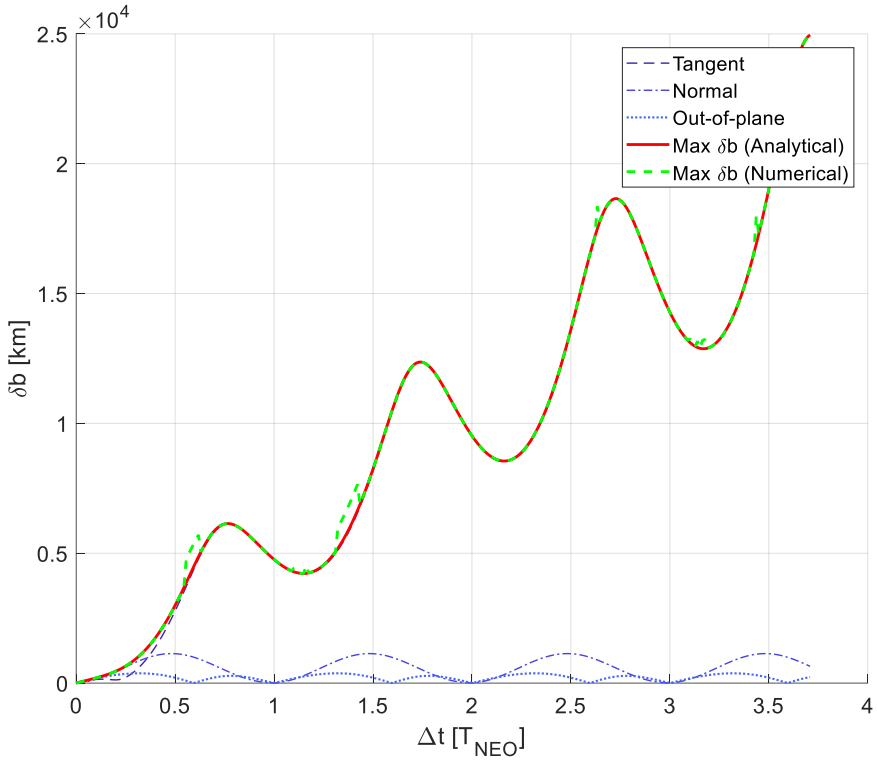

Figure 3.3: Deviation of the impact parameter.

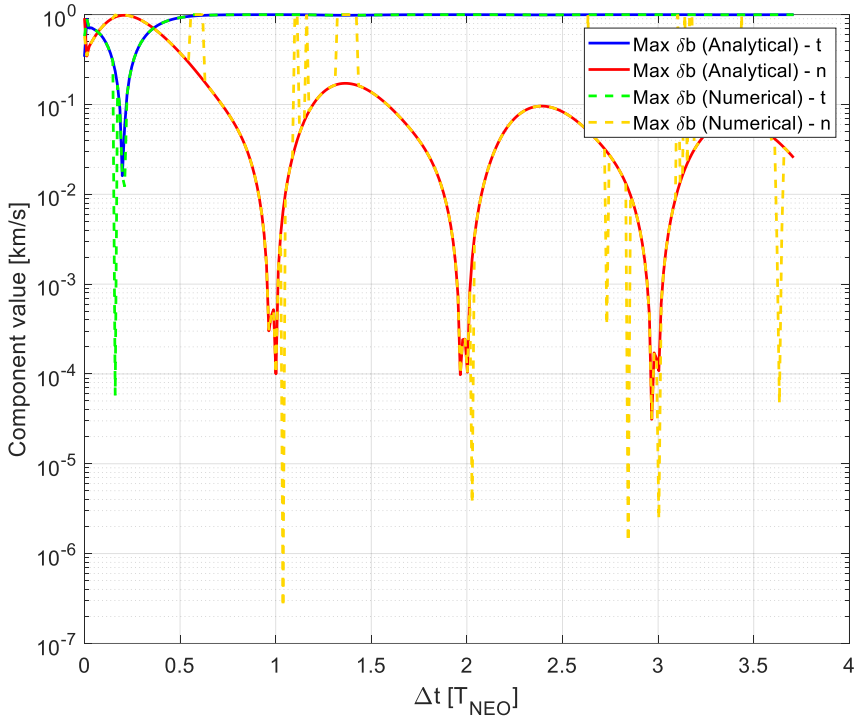

Figure 3.4: Maximum δb deviation direction.

Eigenvalue Method	Numerical Method
$0.1033s$	$70.9133s$

Table 2: Computational time for the maximum b deviation.

3.3.1.2 *Maximisation of the ξ Coordinate Deviation ($\delta\xi$)*

The structure of the results displayed in this section is equivalent to the one detailed in section 3.3.1.1.

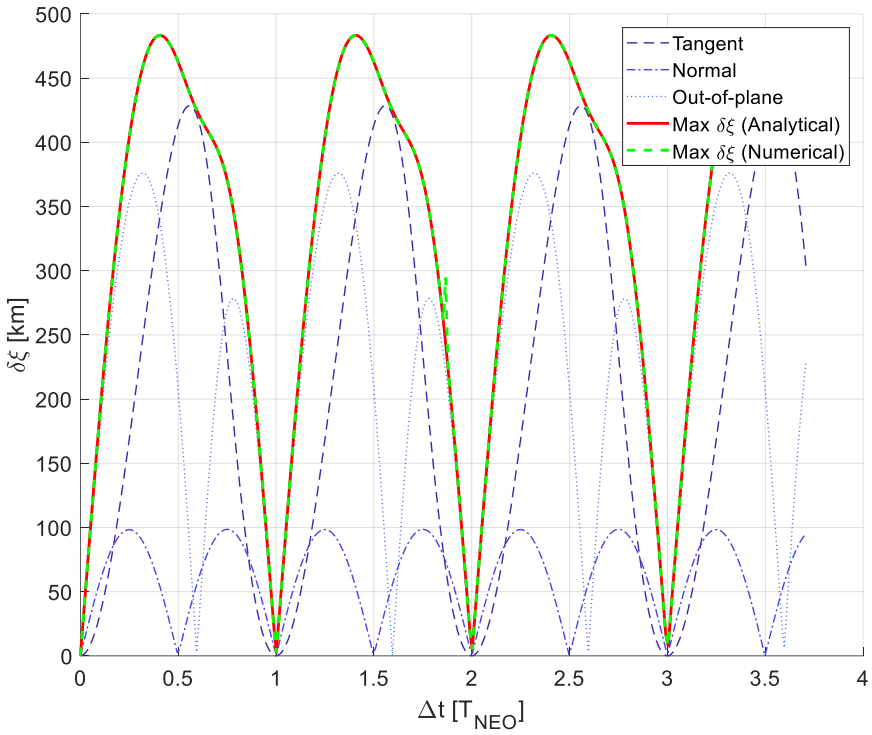

Figure 3.5: Deviation of the ξ component.

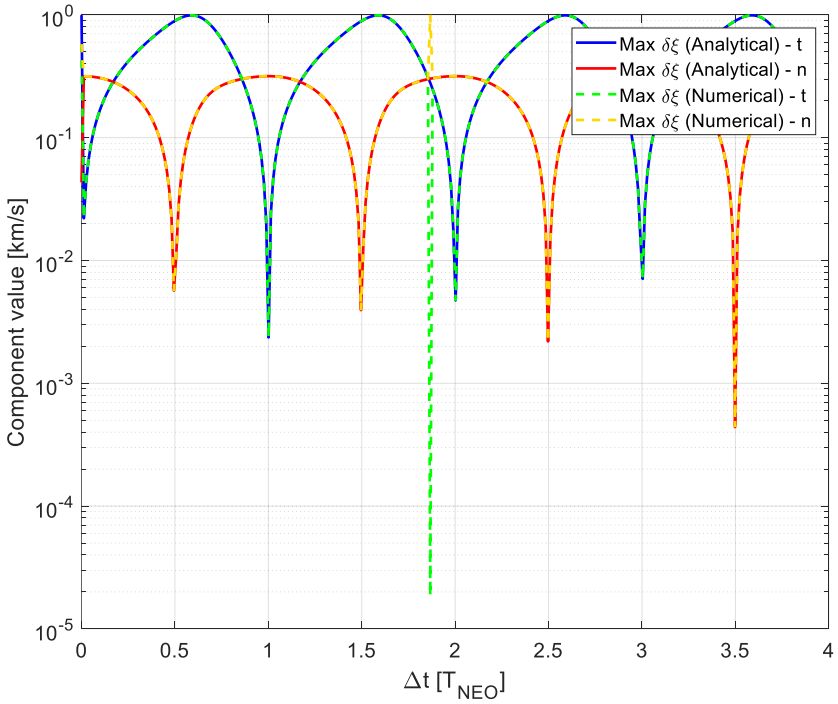

Figure 3.6: Maximum δξ deviation direction.

Eigenvalue Method	Numerical Method
$0.1435s$	$15.6473s$

Table 3: Computational time for the maximum ξ deviation.

3.3.1.3 *Maximisation of the ζ Coordinate Deviation ($\delta\zeta$)*

The structure of the results displayed in this section is equivalent to the one detailed in section 3.3.1.1.

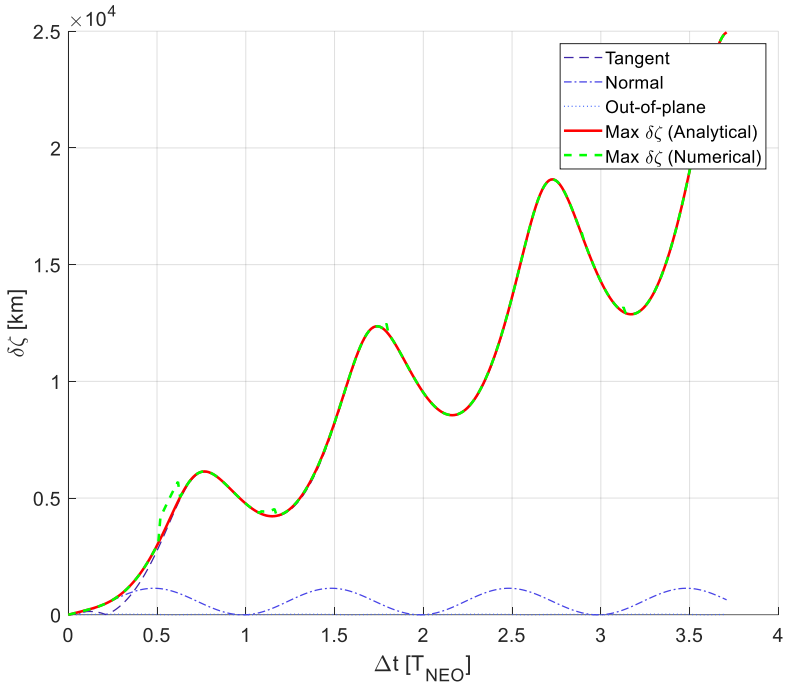

Figure 3.7: Deviation of the ζ component.

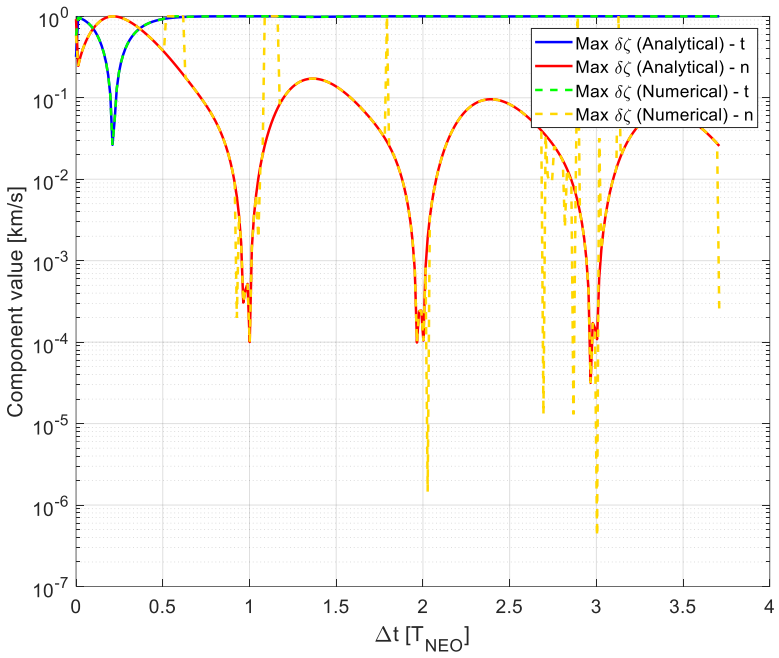

Figure 3.8: Maximum $\delta\zeta$ deviation direction.

Eigenvalue Method	Numerical Method
$0.1783s$	$56.6891s$

Table 4: Computational time for the maximum ζ deviation.

3.3.2 Considerations

As it can be seen in the figures in section 3.3.1, the methods exploiting the maximum eigenvalue technique are equivalent to the numerical method ones; indeed the lines relative to the analytical method and those relative to the numerical one are coincident, apart from some points in which the numerical optimisation did not converge with the applied settings, which do not compromise the point of this comparison.

One of the advantages of the analytical approach is the drastic reduction in the time required to perform the computations when using the eigenvalue method compared to the numerical optimiser, as shown in Table 2, Table 3 and Table 4. Furthermore, the difference would be even greater if a higher number of evaluations were to be introduced in the numerical optimisation to reduce the problem of non-converging points or if the proposed approach were to be coupled to the trajectory design for the spacecraft to reach the NEO and deflect it, as done by Vasile and Colombo [22], given that it would require embedding this formulation into a global optimisation procedure integrating the transfer trajectory and the deflection phase.

The second and main advantage lies in the possibility of defining an analytical technique to identify the optimal direction to obtain a maximisation of each of the parameters, as already done in the case of the maximum geometric deviation [22]. This property helps in giving a better insight into the deflection problem.

3.4 Optimal Deflection Direction

Asteroids 2010 RF_{12} and 1979 XB were chosen as test subjects for their difference in orbital parameters to represent two relatively different cases. In particular, asteroid 1979 XB features an orbit with a large value for the period, as well as significant eccentricity and inclination values, whereas 2010 RF_{12} is characterised by an orbit closer to the Earth's, as can be seen in Table 5 (the ephemerides data has been obtained by SPICE [30]).

	a	e	i
2010 RF_{12}	$1.05AU$	0.19	$0.91°$
1979 XB	$2.35AU$	0.73	$25.4°$

Table 5: Orbital parameters of the chosen NEOs.

The analysis of the deflection is carried out at the entrance of the unperturbed asteroid in the SOI. It should be noted that the configuration of the close approaches determined by the simplified propagation will result in minor differences with the real optimal directions for the deviations on the b-plane (corresponding to a more accurate propagation); the underlying general rules described in the following subsections (3.4.2, 3.4.3, 3.4.4) remain valid.

Furthermore, the representation of the b-plane components is shown on the b-plane computed considering the unperturbed encounter of the NEO with the Earth, instead of the one relative to the perturbed relative velocity of the asteroid with respect to the Earth. This approach does not impair the outcome of the study as the plane perpendicular to the nominal relative velocity and the one perpendicular to the perturbed relative velocity are very close to each other [22].

This study considers a possible deviation starting from 1 d before the encounter up to 6000 d to examine the effects of the Δt value, i.e. the time between the deflection and the expected close approach, on the direction of optimal deviation, as already done by Vasile and Colombo [22].

3.4.1 Maximum Geometric Deviation

Figure 3.9 and Figure 3.10 show the components of the optimal deviation direction (i.e. the $\boldsymbol{\delta v}$ that maximises the corresponding deviation at the MOID) for each NEO in function of the deflection time Δt (i.e. the time between the deflection and the close-approach), expressed as multiples of the NEO's orbital period. As already done in section 3.3.1, the values of the components are expressed on a total norm of 1 (i.e. a normalised

deflection vector is considered); this approach is equivalent to considering the dimensional velocity vector, as stated in section 3.2.3. The normal component is the preferred one for low values of Δt until a deviation time that differs for each asteroid, but is lower than the value of its orbital period. From this point earlier (i.e. for longer deviation times), the tangent component is the most effective one [22]. It should be noted that a deviation in the normal direction would yield practically no result if performed at $\Delta t = kT_{NEO}$. The out-of-plane component's value is not shown, as it is below 10^{-13}.

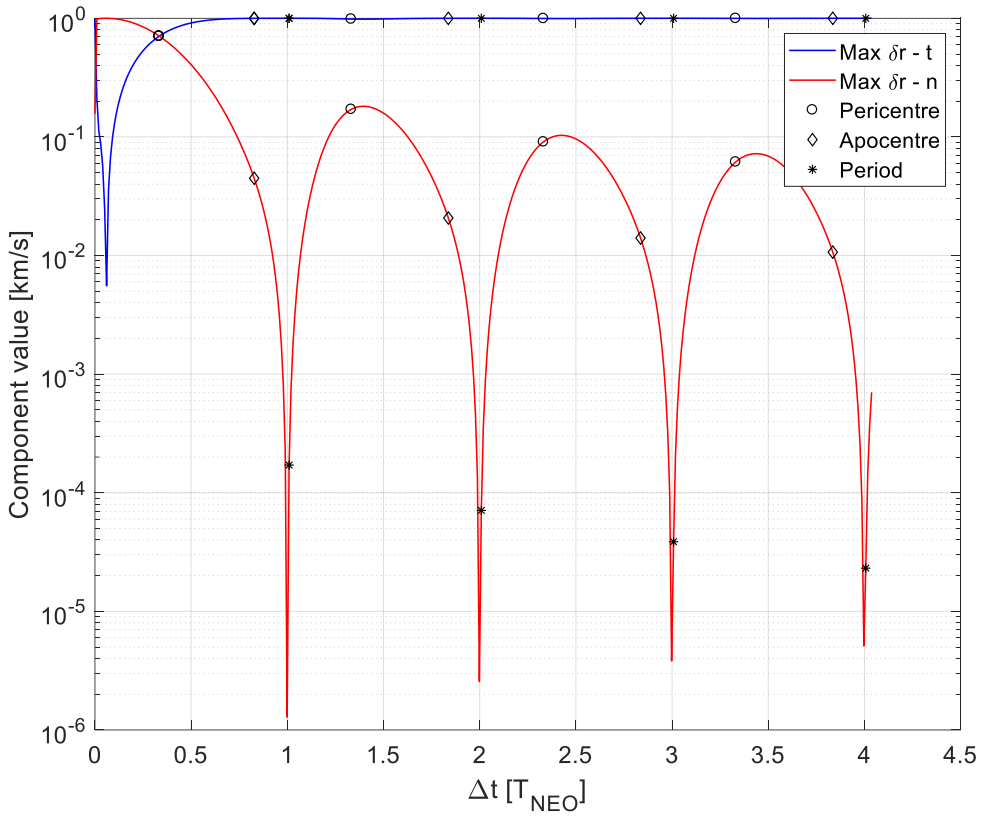

Figure 3.9: Components of the maximum δr deviation direction for 2010 RF_{12}.

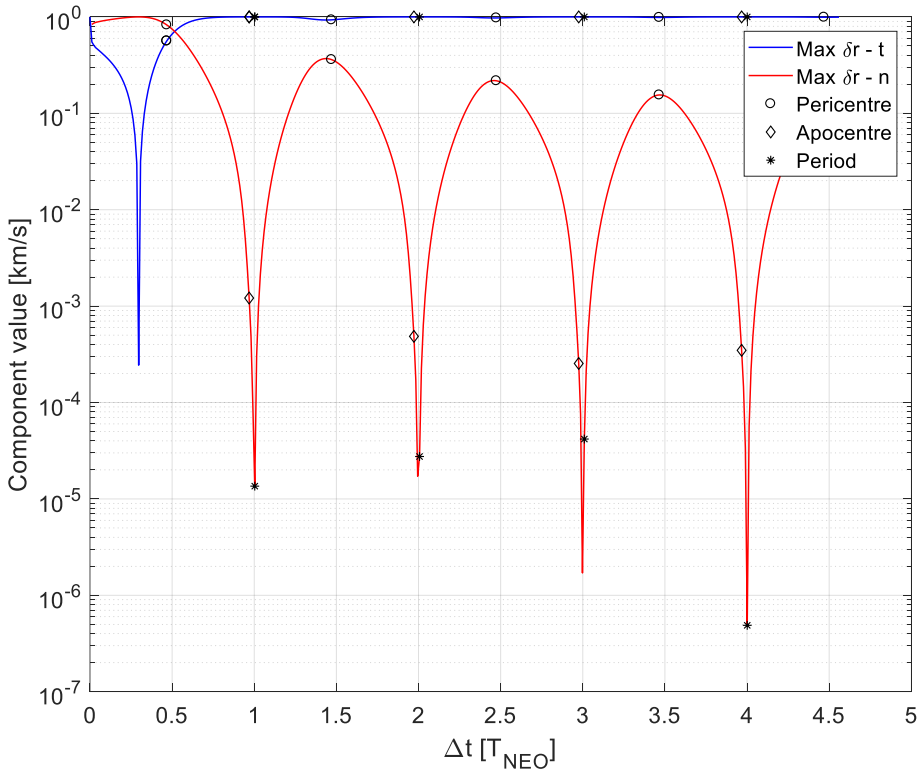

Figure 3.10: Components of the maximum δr deviation direction for 1979 XB.

As the orbital velocity is higher at the pericentre, this condition will correspond to a local maximum in the deviation magnitude, whereas a deflection at the apocentre gives a displacement close to the local minimum [8].

3.4.2 Maximum Impact Parameter Deviation

We can now compare the maximisation of the geometric deviation (see Figure 3.9 and Figure 3.10) to the maximisation of the deviation on the b-plane.

The direction of maximum δb increase is different compared with the strategy to maximise the geometric distance deviation for small values of $\Delta t < T_{NEO}$. This aspect can be appreciated in Figure 3.12 and Figure 3.13, which show how the tangent and out-of-plane components dominate the deviation early on for 2010 RF_{12} and 1979 XB respectively, later (for larger values of Δt, i.e. for earlier deflections) to be replaced by the normal component and finally by the tangent component, aligning with the maximum δr behaviour (i.e. the tangent component of the deflection velocity vector prevails for Δt values above a given threshold, see section 3.4.1).

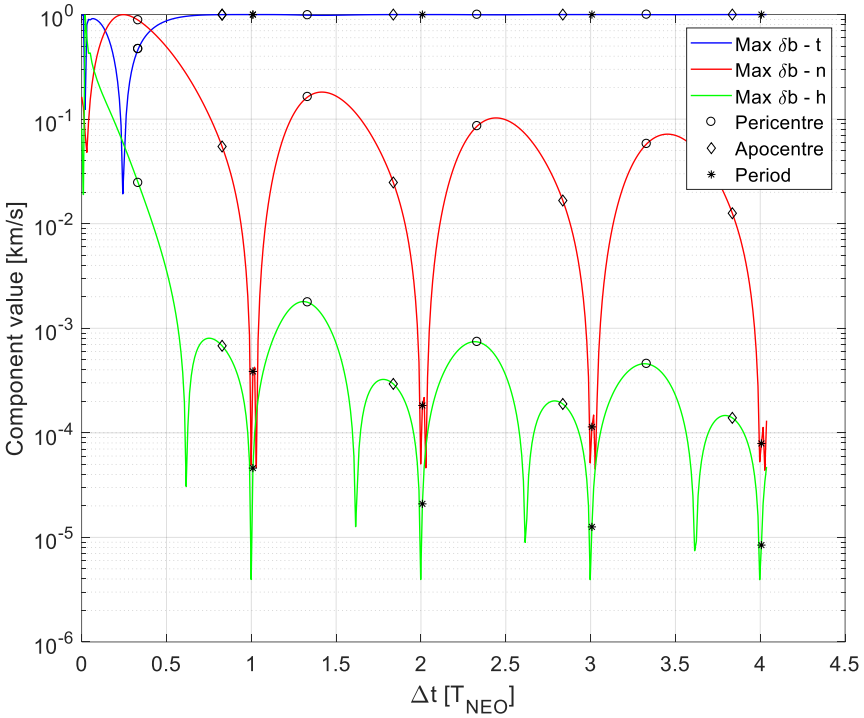

Figure 3.11: Components of the maximum δb deviation direction for 2010 RF₁₂.

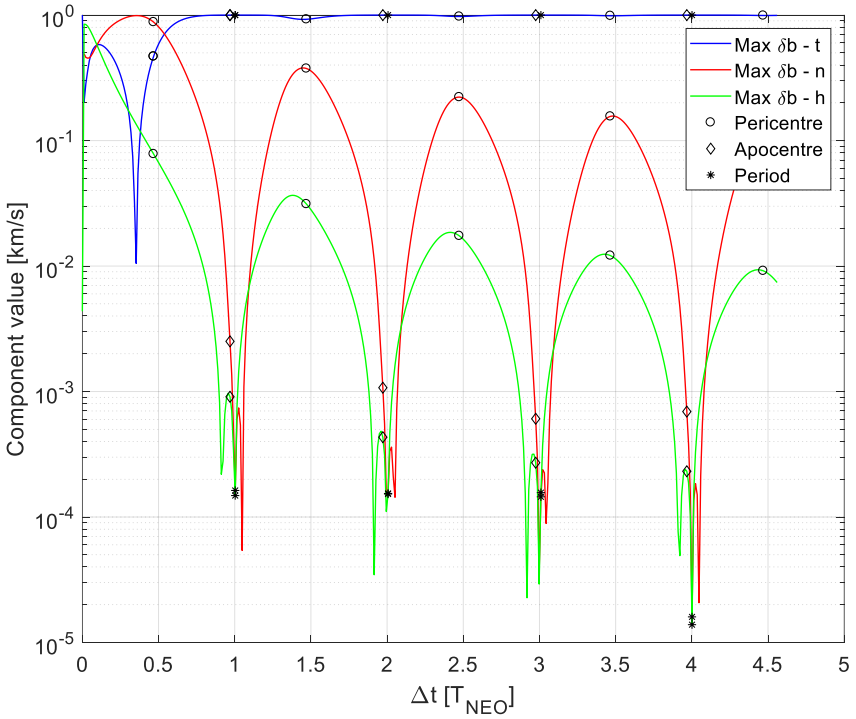

Figure 3.12: Components of the maximum δb deviation direction for 1979 XB.

The oscillations of the normal and out-of-plane components in the neighbourhood of $\Delta t = kT_{NEO}$ stem from the sign change of those components (which translate to oscillations in the logarithmic representation) and vary for each asteroid.

3.4.3 Maximum ξ Deviation

In the present section, the direction of $\boldsymbol{\delta v}$ is optimised in order to maximise the deviation of the ξ component.

In the case of the asteroid 2010 RF_{12}, the maximum $\delta\xi$ deviation direction alternates between out-of-plane and tangent throughout the period, whereas in the case of asteroid 1979 XB the tangent direction is dominant most of the time, with a contention between the normal and the out-of-plane components at the beginning of each period. Furthermore, the deviation proves very ineffective if performed along the tangent direction at $\Delta t = kT_{NEO}$, along the normal direction at $\Delta t = kT_{NEO} + T_{NEO}/2$ and along the out-of-plane direction for a value of Δt which varies for each NEO. These patterns can be observed in Figure 3.13 and Figure 3.14.

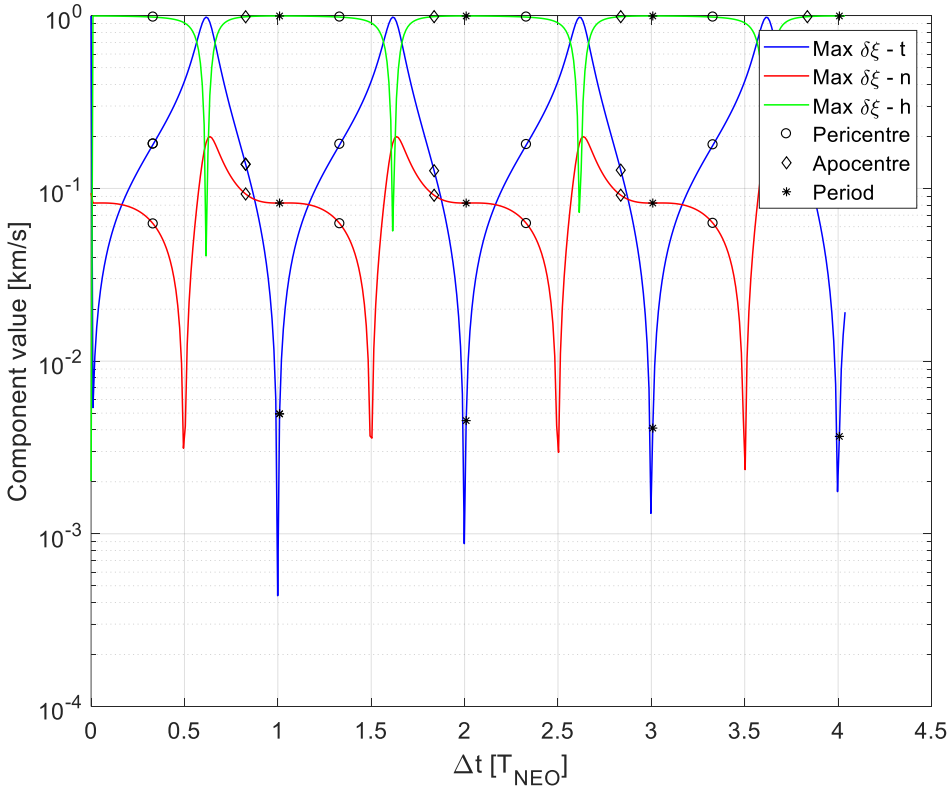

Figure 3.13: Components of the maximum $\delta\xi$ deviation direction for 2010 RF_{12}.

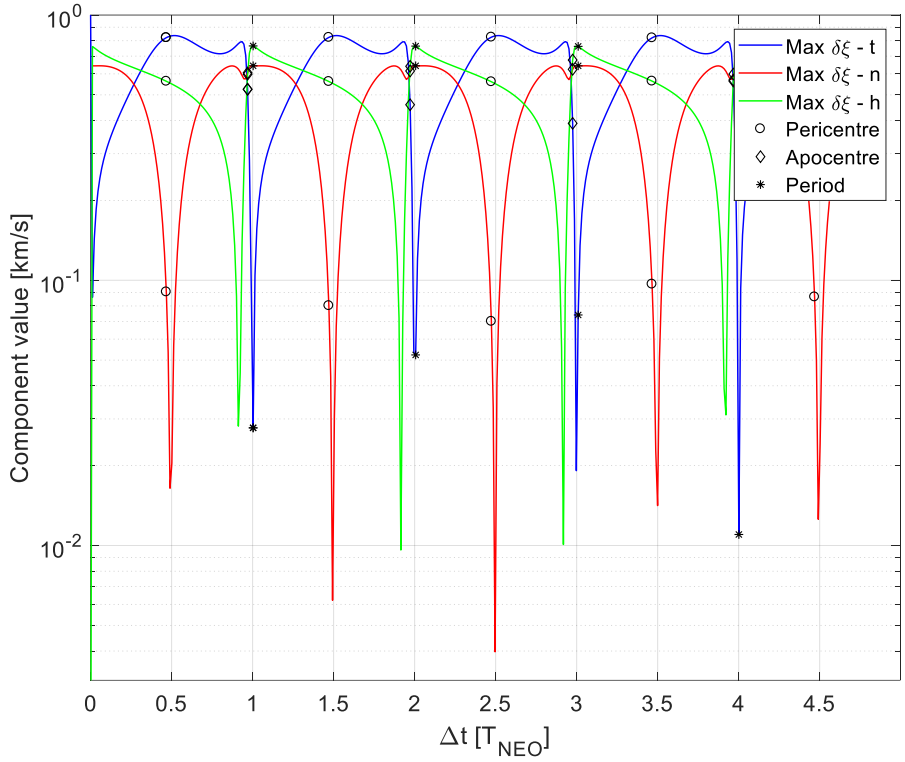

Figure 3.14: Components of the maximum $\delta\xi$ deviation direction for 1979 XB.

It is important to notice how the maximisation of the $\delta\xi$ component is the only one not featuring a cumulative effect with the number of periods of the asteroid, as it can be seen in Figure 3.6. This is to be expected, as the maximisation of δr and δb follow the tangent direction beyond $\Delta t = T_{NEO}$, which is expected to mainly cause a shift in the time the asteroid reaches the MOID.

3.4.4 Maximum ζ Deviation

Figure 3.15 and Figure 3.16 show how the direction of maximum ζ deviation follows similar rules as the δb maximisation (see section 3.4.2). This result is consistent with the limited effect of the $\delta\xi$ maximisation beyond $\Delta t = T_{NEO}$, beyond which the optimal δb direction practically coincides with the $\delta\zeta$ one, as the ζ direction is related to the phasing, which is more easily modified than the ξ-related MOID [21].

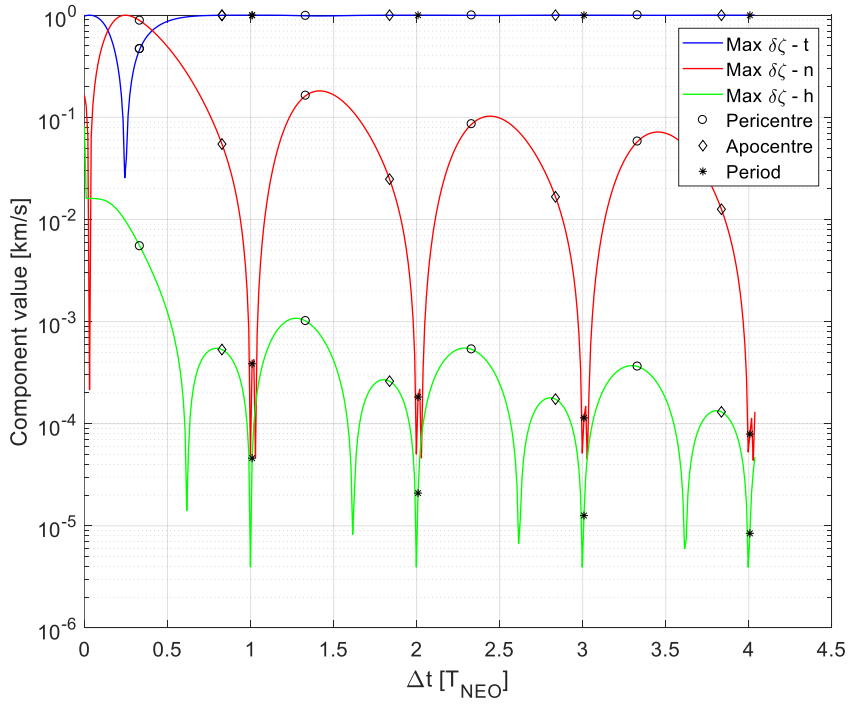

Figure 3.15: Components of the maximum $\delta\zeta$ deviation direction for 2010 RF_{12}.

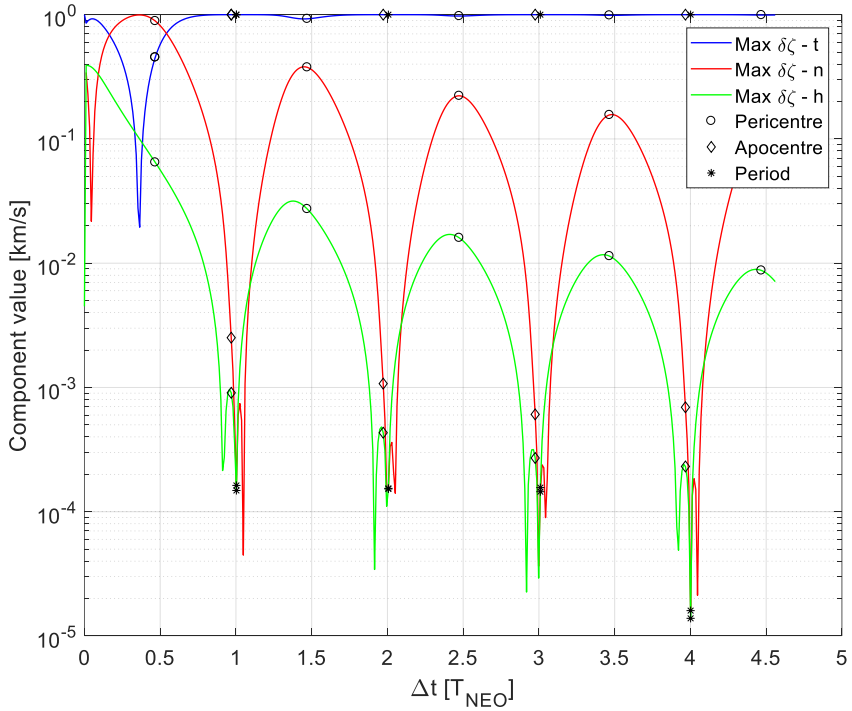

Figure 3.16: Components of the maximum $\delta\zeta$ deviation direction for 1979 XB.

3.5 Deflection Strategy to Avoid the Keyholes

An effective strategy to prevent a resonant return could be to deflect a NEO in such a way that its trajectory crosses the encounter b-plane far from any of the calculated keyholes; the distance from the keyholes is aimed at providing some robustness to the deflection action towards real-world effects, such as the real deflection not corresponding to the expected one. Assuming the asteroid could be deflected a sufficient amount of time before the first close approach, a deviation along the ζ-axis would be very convenient, as is detailed in chapter 3.4. For this reason, a target value of ζ can be selected based on the following criteria:

- Nominal encounter within a keyhole: the target ζ value is located halfway between the keyhole in question and the following one in the direction of increasing modulus of ζ; this direction is selected considering the fact that deflecting the NEO away from the Earth rather than towards it would be a safer manoeuvre in the case the result of the manoeuvre did not correspond to the desired one
- Nominal encounter between two keyholes: the middle point between the two keyholes is selected as the target ζ value

Figure 3.17 illustrates some examples of the criteria described above. The black circles correspond to nominal encounter conditions on the b-plane and the arrows connect them with the associated target ζ values.

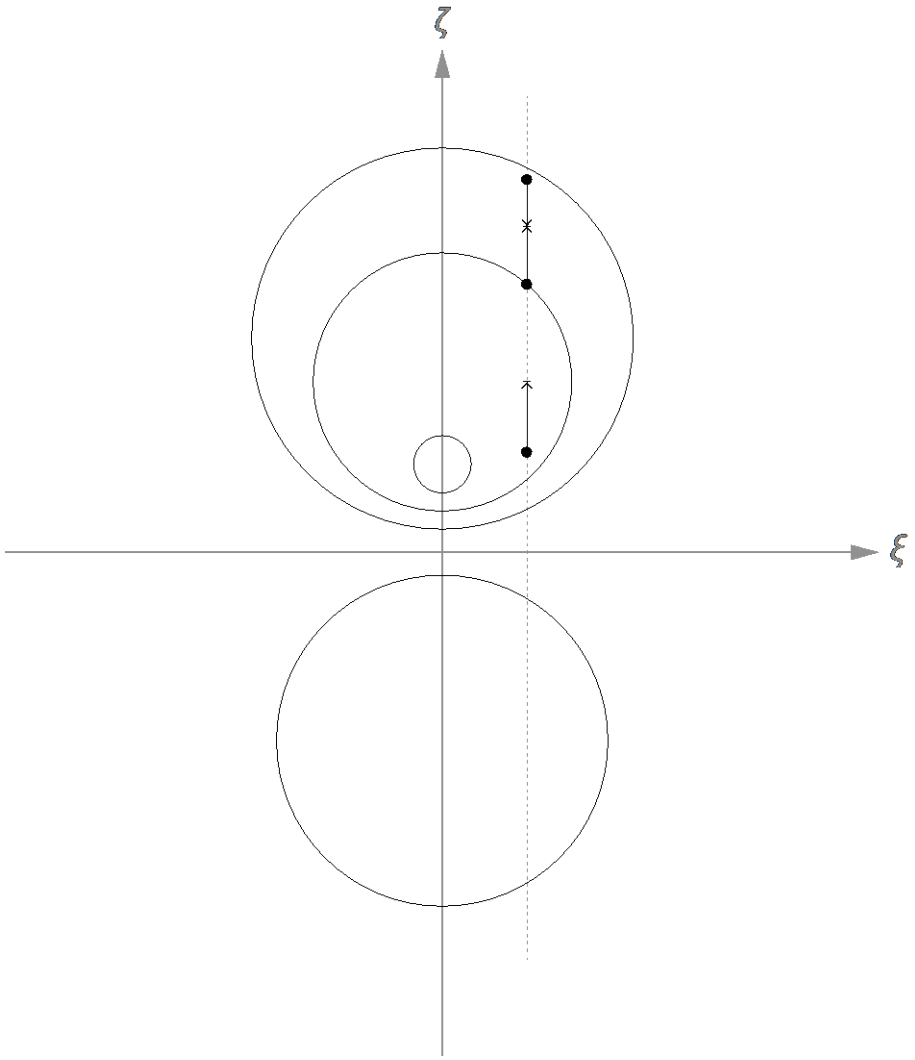

Figure 3.17: Target ζ values for conditions on the b-plane qualitative example.

The formulas presented in section 3.2.2.2 can be used to determine the $\boldsymbol{\delta v}$ vector to be applied to the asteroid at the deflection coordinates to obtain the desired $\delta\zeta$ deviation on the b-plane through the following procedure:

1. Determination of the direction of maximum $\delta\zeta$ variation through the eigenvector method
2. Multiplying the modulus of the unitary $\boldsymbol{\delta v}$ vector by a factor $\delta\zeta / \delta\zeta_{eig}$, where $\delta\zeta_{eig}$ is the displacement along the ζ-axis obtained with the unitary $\boldsymbol{\delta v}$ vector (resulting from the eigenvector method)

It should be noted that the presented technique features some displacement along the ξ-axis (i.e. a change in the MOID) in addition to the desired one along the ζ-axis (i.e. a change in the encounter phasing), as the selected direction only guarantees the conditions to obtain the maximum value of $\delta\zeta$ for a given modulus of $\boldsymbol{\delta v}$ and value of Δt. The displacement along ξ can however be disregarded, as it is considerably smaller with respect to the one along ζ (see section 3.4.4).

A convenient strategy to determine the optimal deflection direction would be represented by the inversion of Equation 3.6, which would determine the exact $\boldsymbol{\delta v}$ associated with a given $\delta\zeta$. This technique can however not be applied, as the invertibility of matrix $\boldsymbol{T}_{\boldsymbol{\delta\zeta}}$ is not guaranteed. The best way to solve the problem at hand therefore remains the procedure detailed in this chapter.

3.5.1 Comparison with the Maximisation Strategies

The algorithm presented in this chapter is based on a different concept compared to what has been done in the previous optimisation strategies (see sections 3.2.3 and 3.4). The aim of the previous optimisations was the maximisation of the relative quantity on the b-plane (b, ξ or ζ), whereas the present technique aims for specific positions on the b-plane, as specified above.

In the case that a limited modulus of $\boldsymbol{\delta v}$ is available, the outcome of the maximisation strategies and of the keyhole-avoiding method could coincide if the latter features a target ζ value with a greater absolute value than the nominal encounter's; this is the case in the example from section 4.3.

4 Results for the Avoidance of Resonant Encounters

A fundamental premise to the application in this chapter is that the results featured in this section are obtained through a Two-Body Problem (2BP) propagation of the coordinates of both the asteroid and the Earth since their initial conditions, provided by SPICE's ephemerides data [30], and are therefore not fully representative of the real conditions, all the while maintaining their general validity. This is done to better highlight the theoretical value of the theory derived in chapter 3 as a preliminary design tool for a mission to subsequently be refined in the framework of the n-body problem (nBP); this could therefore be a possible extension of the present work.

4.1 Propagation Considerations

While the gravitational effects determining the trajectories of both the celestial bodies and the spacecraft featured in this dissertation are based on a patched two-body approach (the gravity of the Sun and the Earth are considered one at a time), with the exception of the n-body propagation used in section 2.9.1, several types of propagators have been examined during the thesis work:

- Heliocentric Keplerian two-body motion
- Patched two body approach exclusively considering the gravitational effect of the Earth inside its SOI and the one of the Sun when outside of it
- n-body approach based on the sum of the gravitational effects of the Solar System planets

The comparison between the results obtained by means of these propagators as well as the ephemerides data provided by the SPICE toolkit [30] have brought to light a very significant problematic when integrating the position of a body undergoing a fly-by of a planet, as already highlighted by many authors [12] [32].

As can be observed in Figure 4.1, the post-fly-by coordinates of 2010 RF_{12} obtained with the different propagators diverge significantly between each other, leading to very different patterns in the distance of the asteroid from the Earth. A different behaviour is present after the first flyby in Figure 4.2, while the previously described phenomenon takes place after the second flyby. This effect is mainly due to the fly-by perturbing the orbit of the NEO differently in function of the pre-encounter conditions, which vary between the cases as the different types of propagations slowly diverge starting from the same initial conditions. The first flyby in Figure 4.2 does not exhibit a very significant difference between the post-fly-by trajectories, as the limited propagation time since the initial conditions has not allowed for a sufficient differentiation between the encounter conditions of the different propagators.

It should be noticed that the divergence of the propagated nBP conditions up to the fly-by in Figure 4.1 is sufficient to cause the asteroid not to enter the Earth' SOI at the close approach; thus the encounter is only registered in the case of the SPICE ephemerides.

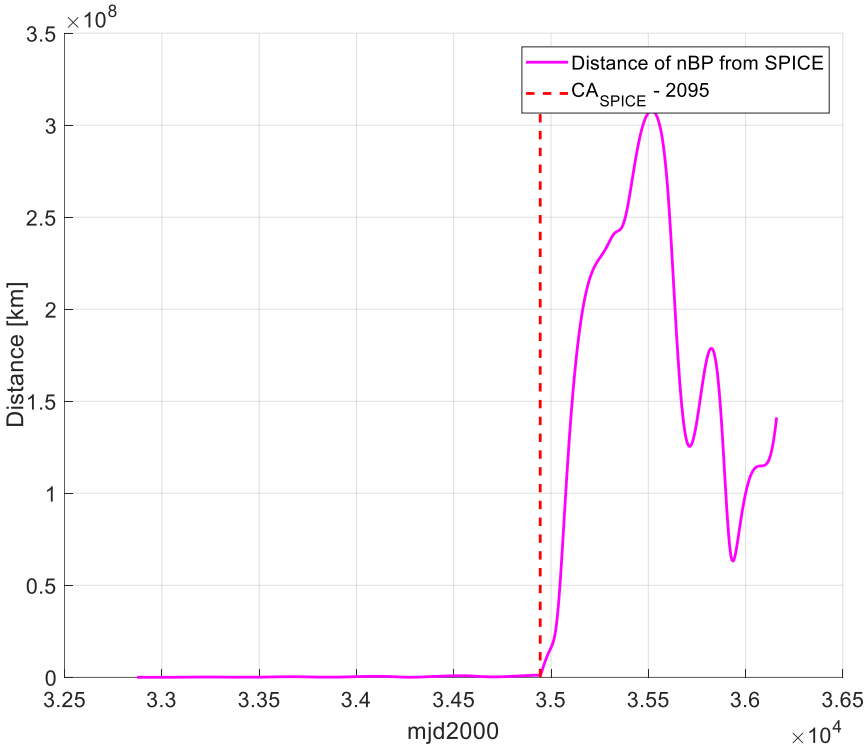

Figure 4.1: Comparison between the different methods of propagation in the case of a late fly-by.

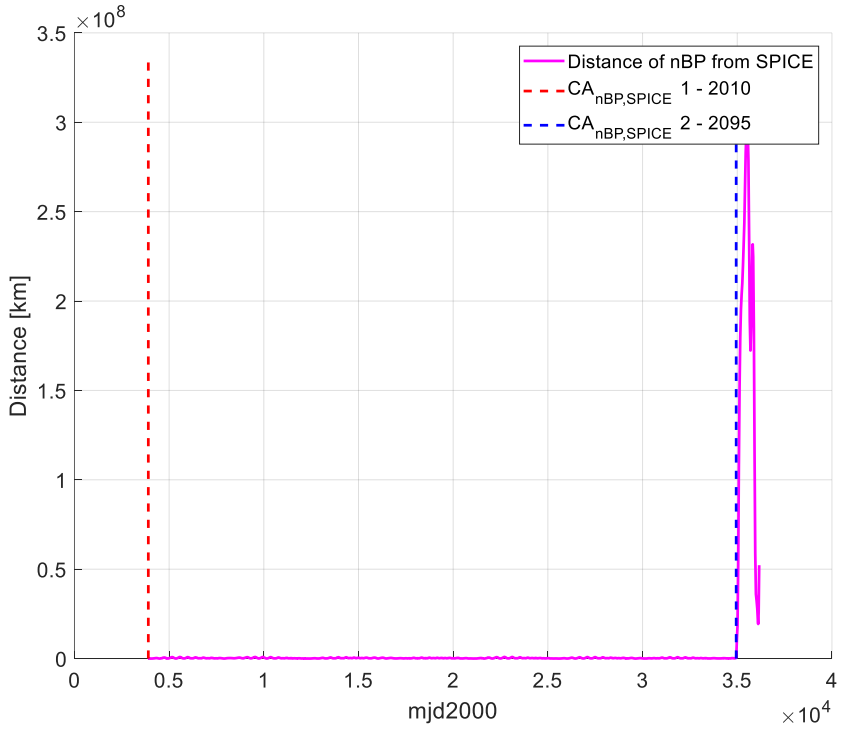

Figure 4.2: Comparison between the different types of propagation in the case of an early fly-by.

On the one hand, these results corroborate what has been stated in section 2.9.1, as the propagation between encounters does not exhibit large discrepancies between the methods in the short term. On the other hand the fine differences between the propagation methods can produce significant changes when analysing close-approaches and this phenomenon should be taken into consideration if trying to expand the present work to consider a more realistic n-body propagation aimed at obtaining the accurate return coordinates of an asteroid to Earth. In the following sections of this chapter, as already stated, the optimisation will be performed in the patched two-body problem framework.

4.2 Optimal Deflection

4.2.1 Optimal Deflection of 2010 RF_{12}

Let us consider a fictitious situation in which the 2095 encounter of 2010 RF_{12} with the Earth takes place in one of the b-plane's keyholes, specifically the $(6,5)$ one, leading to a potential dangerous return of the NEO in the year 3001. This condition would clearly be highly undesirable and a deflection mission to the asteroid would be recommended. The values of the Keplerian parameters assumed for both the Earth and the NEO are the ones previously detailed in Table 1.

An effective strategy to prevent the expected resonant return could be to deflect 2010 RF_{12} in such a way that its trajectory crosses the 2095 encounter b-plane far from any of the calculated keyholes. For the scope of this example, the asteroid is assumed to be deflected 400 d before the first close approach, allowing to apply the strategy described in chapter 3.5. The target deflection will therefore be a $\delta\zeta$ value equal to half the distance between the current keyhole $(6,5)$ and the next one in the direction of increasing ζ $(7,6)$.

Figure 4.3 depicts the orbits of the Earth and the modified NEO (corresponding to the fictitious encounter conditions, i.e. modified compared to the original NEO), before and after the deviation. Figure 4.4 portrays the b-plane of the encounter; the resonant circles in the figure are computed analytically and therefore do not correspond with the numerical keyholes. The coordinates of the keyholes considered for the optimal deflection strategy, as well as the chosen target ζ value are shown as asterisk symbols. Finally, Figure 4.6 displays the propagation of the post-fly-by conditions corresponding to the nominal conditions for the fictitious encounter and the deviated conditions obtained through the optimisation strategy in the form of the distance of the NEO from the Earth. The line corresponding to the nominal conditions clearly exhibits a return of the asteroid to the Earth, whereas the propagation of the deviated NEO suggests that the following encounter has been avoided.

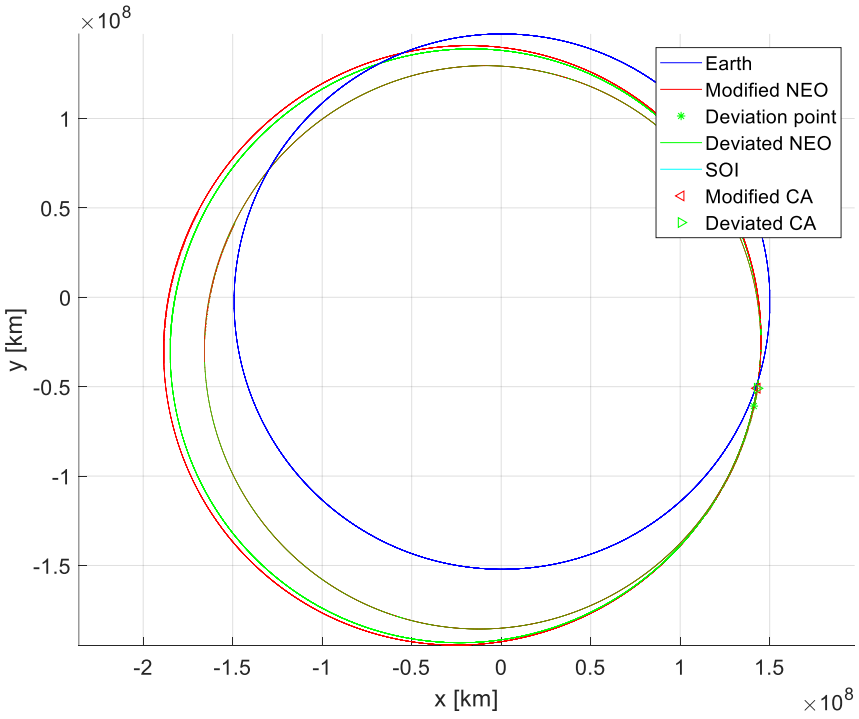

Figure 4.3: Orbits of the Earth and the asteroid (modified and deviated).

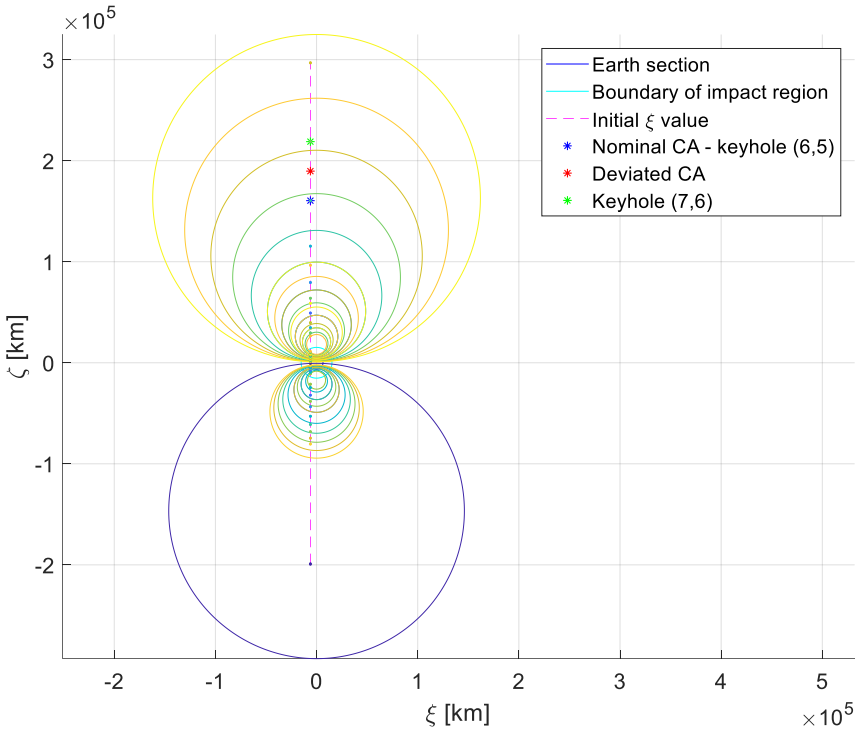

Figure 4.4: B-plane of the 2095 close approach of 2010 RF_{12} with the Earth featuring the initial and deviated conditions.

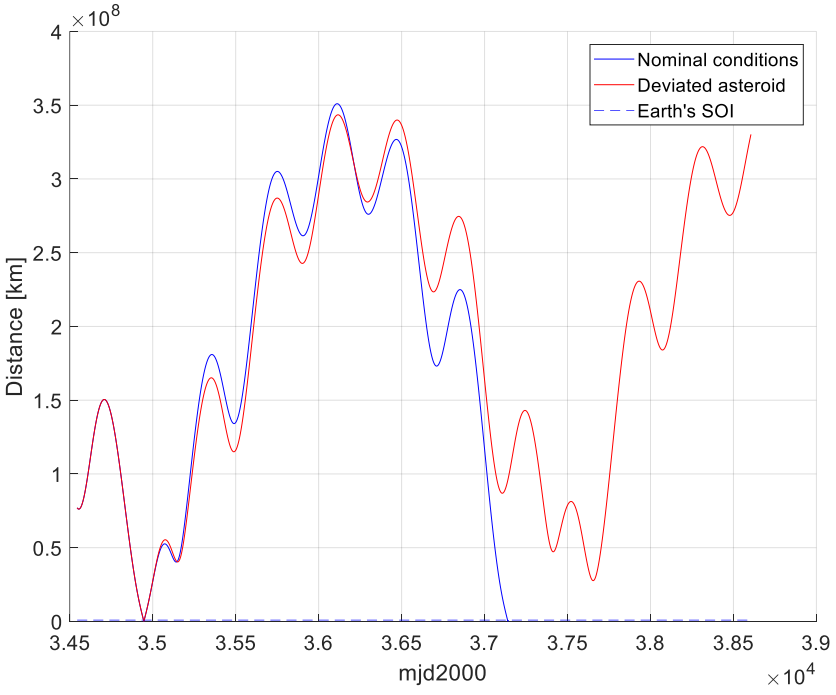

Figure 4.5: Distance of the nominal and deviated 2010 RF_{12} from the Earth.

The optimal deviation, based on the procedure presented in this section and the assumed data, is obtained for

$$\boldsymbol{dv_{tnh}} = \begin{Bmatrix} 2.7284 \\ 0.0012 \\ -0.0002 \end{Bmatrix} \cdot 10^{-1} \ \mathrm{m/s}$$

(expressed in the tangent-normal-out-of-plane frame of the asteroid) even though a weaker deflection could be sufficient to avoid the following encounter. The computed value should be considered as having an "ideal" magnitude to provide a degree of robustness to the obtained result to face the disturbances due to effects that have not been considered; in particular the perturbation of the Keplerian heliocentric motion due to the presence of the other planets or the effects of the non-ideal deflection of the asteroid.

It should be noted that, even though the current ephemerides values do not anticipate the return featured in this example, the uncertainty associated with the orbital parameters of the NEO resulting from their determination through astronomical observations is such that a condition similar to the one presented here could potentially arise.

4.2.2 Influence of the Deflection Time on the Optimal Deflection

The modulus of the $\boldsymbol{dv}$ vector required to deviate the asteroid in the desired position along the ζ-axis on the b-plane strongly varies in time, as the deviation along the aforementioned axis is a cumulative effect in time, as can be appreciated in Figure 3.8. For this reason, the cost (in terms of $\boldsymbol{dv}$) of the deviation generally decreases with the value of Δt; with the exception of a periodic effect that however features a limited magnitude and therefore does not change the validity of this consideration. Figure 4.6 illustrates the norm of the $\boldsymbol{dv}$ vector required to obtain the optimal deflection from section 4.2.1 considering a time span going from 1 d to 5 y.

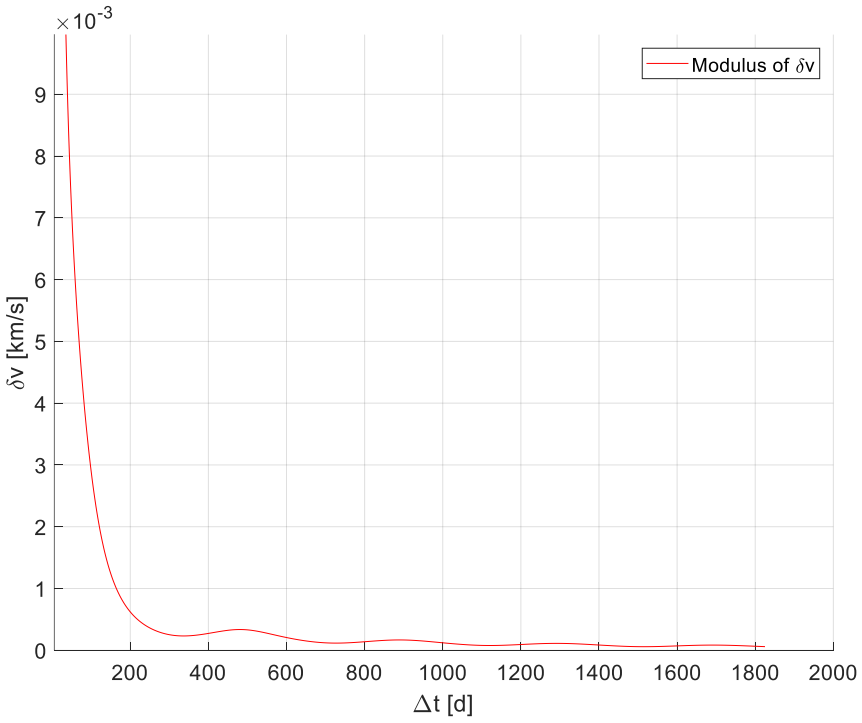

Figure 4.6: Cost of the deviation to obtain a given $d\zeta$ in function of the deviation time.

A further consideration on the combination of $\boldsymbol{dv}$ and the deflection timing can be made observing Figure 4.7, which represents the deflection on the b-plane corresponding to a fixed $\boldsymbol{dv}$ vector over an arc of time. In this case the deflection resulting from the optimal $\boldsymbol{dv}$ for a deflection 400 d before the first encounter (as featured in section 4.2.1) is applied to deflections up to 5 y before the close approach. It can be noted how, for a value of Δt in the $600 - 800$ km range, the deviation results in moving the encounter from the $(6,5)$ keyhole to the $(7,6)$ one, thus only postponing the possibility of an impact.

The simple maximisation of the deviation along a given direction is therefore not always the most convenient deflection strategy in the long run, as it could inadvertently place the NEO in a keyhole (as is the case in Figure 4.7). A deviation aimed at minimising the risk of a resonant return must therefore be controlled in the magnitude of the deviation itself, in addition to the direction of deviation. A notable exception is the deflection of an asteroid very close in time to an impact, for which the deviation cannot take advantage of the growth of the displacement along the ζ-axis in time and the NEO must be distanced from the impact conditions as much as possible, disregarding resonance concerns if necessary.

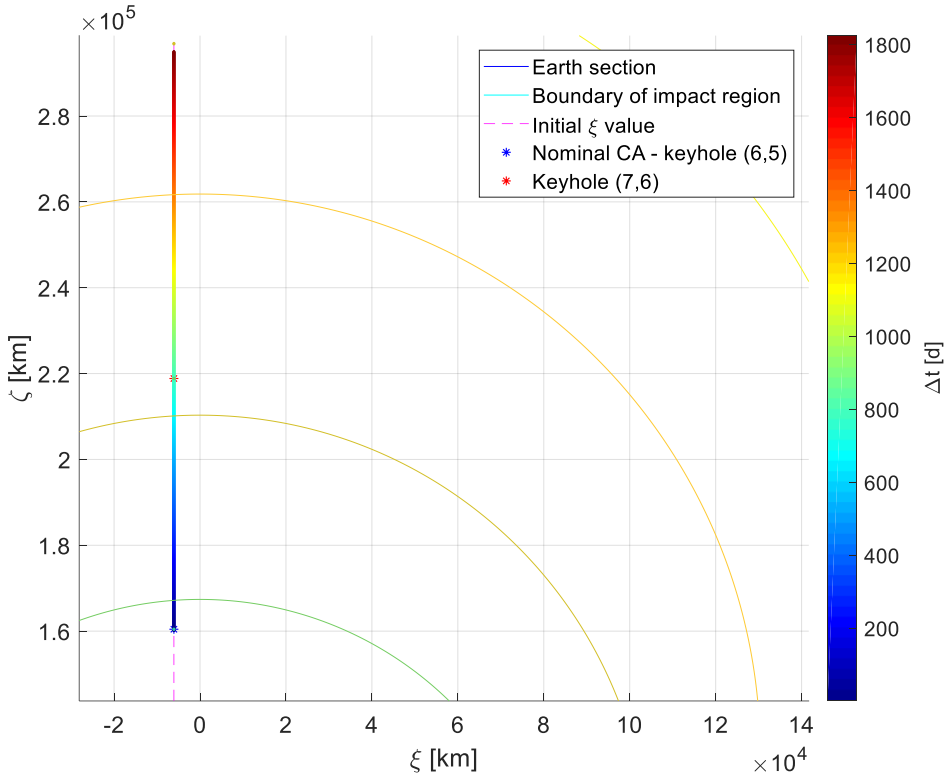

Figure 4.7: Deviation on the b-plane for a fixed $\boldsymbol{dv}$ and varying Δt.

4.3 Deflection Mission Preliminary Design

In this section, a fictitious mission to deflect an incoming asteroid will be analysed, based on what has been done by Colombo et al. [31]. As already done in section 4.2, the 2095 encounter of 2010 RF_{12} with the Earth will be taken into consideration and a two-body propagation will be employed for this study. The same initial Keplerian parameters as those featured in Table 1 are considered in this simulation.

To this purpose, a set of parameters concerning the NEO, the impactor spacecraft and the boundaries of the mission parameters are assumed in accordance with the choices made by Colombo et al. [31]. Such parameters are detailed in Table 6, Table 7 and Table 8 respectively.

The mission is assumed to be composed by the escape of the impactor from the Earth, followed by a Deep-Space Manoeuvre (DSM) to place it on an impact trajectory with the hazardous body. The first section, as stated at the beginning of this study, is obtained by simple Keplerian propagation of the heliocentric coordinates at the departure from Earth, whereas the orbit arc connecting the location of the DSM and the position of the NEO is the result of the Lambert problem solution.

The earliest possible departure from Earth is limited by the warning time; the trajectory between the departure and the arrival to the asteroid is limited by the maximum Time Of Flight (TOF), during which the DSM can be performed. The DSM is considered to take place instantaneously and the same assumption holds true for the deviation of the asteroid. In particular, the latter is modelled as

$$\boldsymbol{dv} = \frac{m_{S/C}}{m_{NEO}}\left(\boldsymbol{v_{S/C}} - \boldsymbol{v_{NEO}}\right)$$

where $m_{S/C}$, m_{NEO}, $\boldsymbol{v_{S/C}}$ and $\boldsymbol{v_{NEO}}$ are the mass of the spacecraft, the mass of the NEO, the velocity vector of the spacecraft and the velocity vector of the NEO at the time of the impact respectively.

The mass of the spacecraft before hitting the asteroid is given by the formula

$$m_{S/C} = m_{S/C_0} \cdot e^{-\Delta v_{DSM}/I_{sp} g_0}$$

where m_{S/C_0} is the initial mass of the spacecraft, Δv_{DSM} is the norm of the DSM, I_{sp} is the spacecraft engine's specific impulse and g_0 is the Earth's gravitational acceleration at sea level.

NEO mass	$1.3614 \cdot 10^9$ kg

Table 6: NEO parameters.

Spacecraft specific impulse	300 s
Spacecraft initial mass	300: 8000 kg
Launcher excess velocity	3 km/s

Table 7: Spacecraft parameters.

Warning time	9 y
Maximum Time Of Flight (TOF)	$1 \cdot \mathrm{T}_{NEO}$

Table 8: Mission parameters.

The results of the problem at hand are obtained through a multi-objective optimisation aimed at achieving the maximisation of the distance of the deviated point from the closest keyholes while minimising the spacecraft initial mass required for the mission. The optimiser returns the results corresponding to different mission parameters amongst the possible combinations allowed by the initial data (departure time, TOF, departure mass, DSM timing) during its search for the optimal condition. These values will be displayed in the following figures alongside the resulting optimal mission ones.

Figure 4.8 presents an overview of the trajectory of the spacecraft resulting from the multi-objective optimisation. Figure 4.9 and Figure 4.10 portray the results of the deflections on the b-plane (represented by

circle symbols ranging from dark blue to yellow) alongside the numerical keyholes; the two keyholes closest to the nominal and deflected coordinates on the b-plane are highlighted by two red circle symbols. A colour-bar flanks the figures to express the distance of the deflected points from the nearest keyhole for each of the computed conditions (the same colour-bar will be present in the flowing figures). Figure 4.11 shows the distribution of the deflection between the ξ and ζ components; it is important to note the difference in the axes' scales. Figure 4.12 describes the correlation between the initial spacecraft mass and the deflection result, in the form of the distance from the nearest keyhole, for each of the deflection conditions returned by the optimiser. Finally, Figure 4.13 depicts the minimum warning time required for the mission (i.e. the difference between the encounter time and the departure time for each of the considered mission parameters combination) as well as the corresponding spacecraft mass before the collision with the NEO.

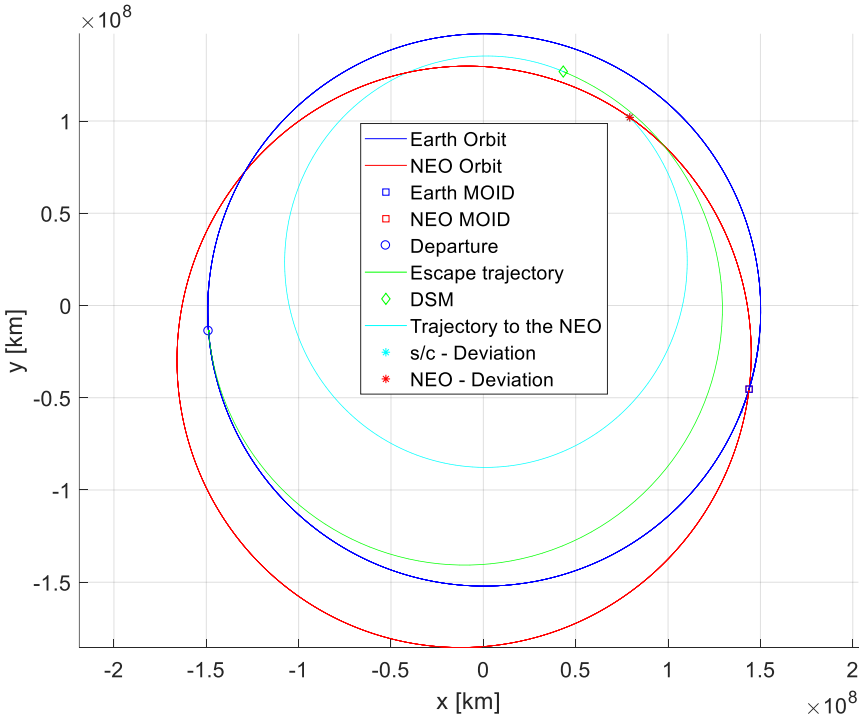

Figure 4.8: Optimal trajectory combination for the deflection mission.

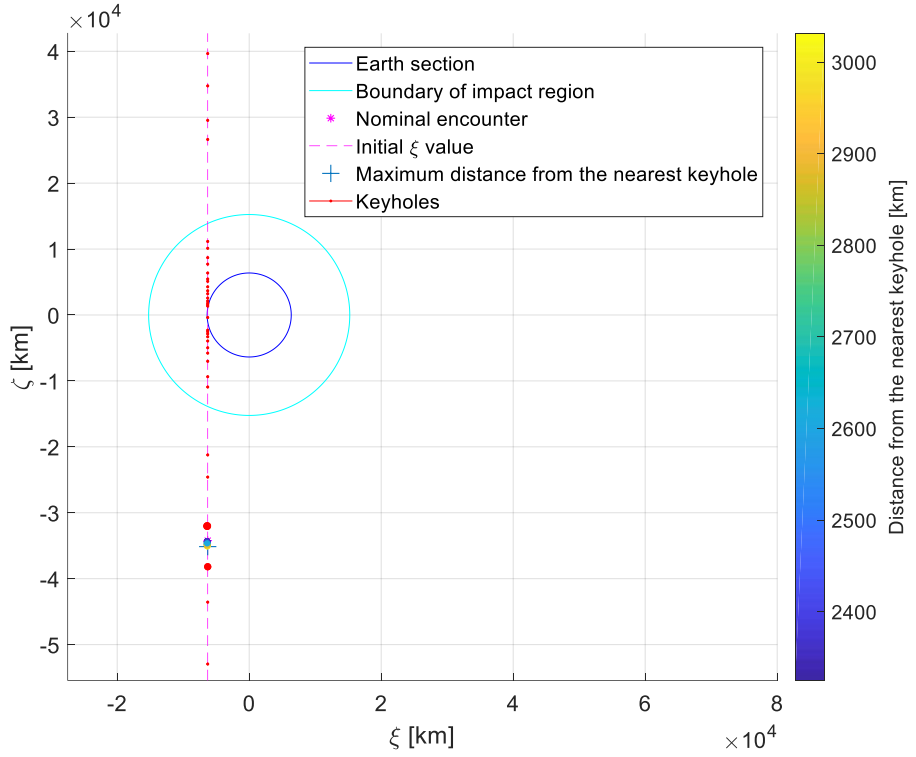

Figure 4.9: B-plane of the encounter containing the points corresponding to the possible deflections.

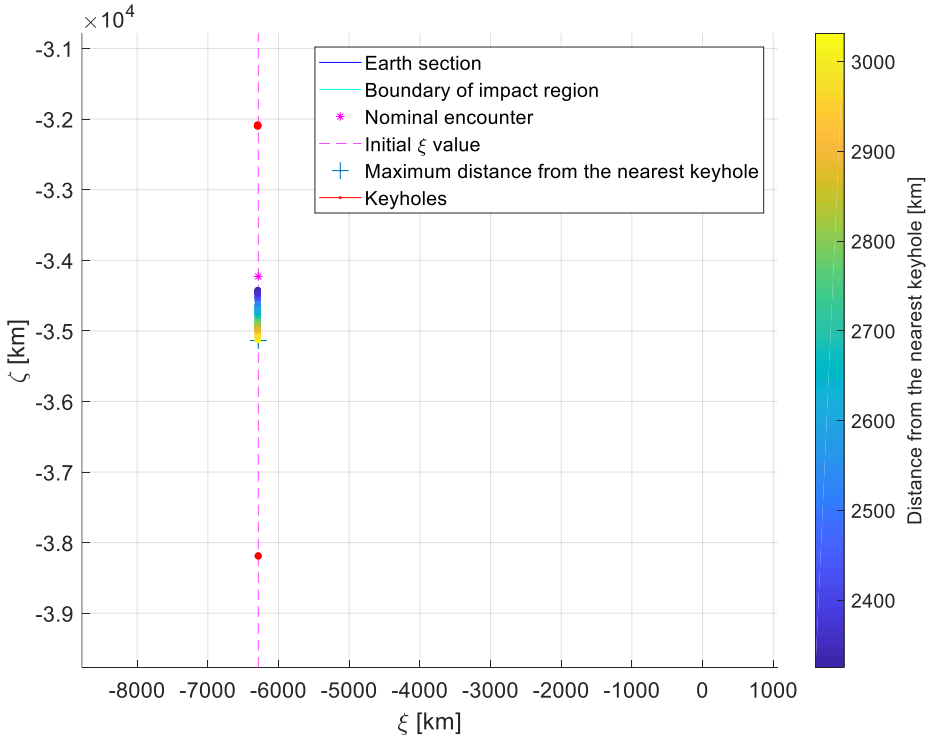

Figure 4.10: Zoom-in of Figure 4.9.

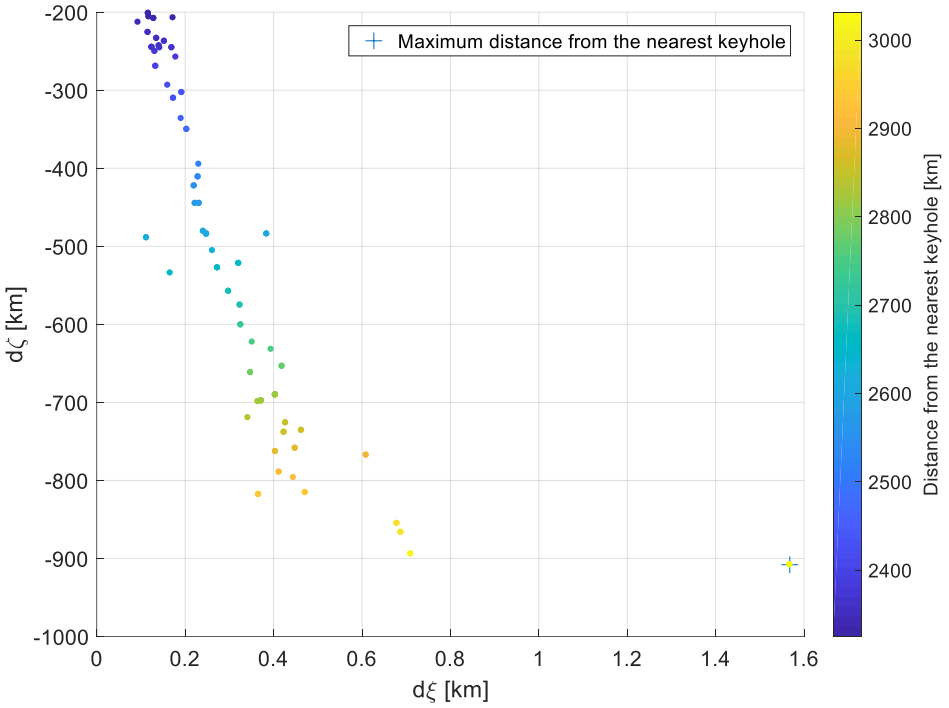

Figure 4.11: Deviation along the ξ and ζ axes of the b-plane.

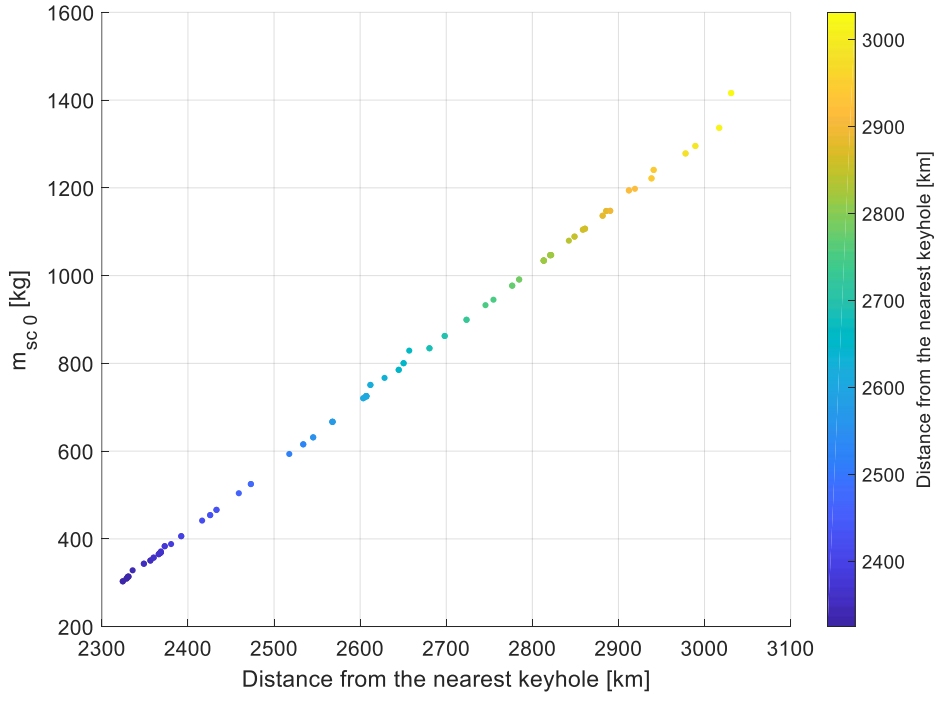

Figure 4.12: Correlation between the initial spacecraft mass and the deflection result.

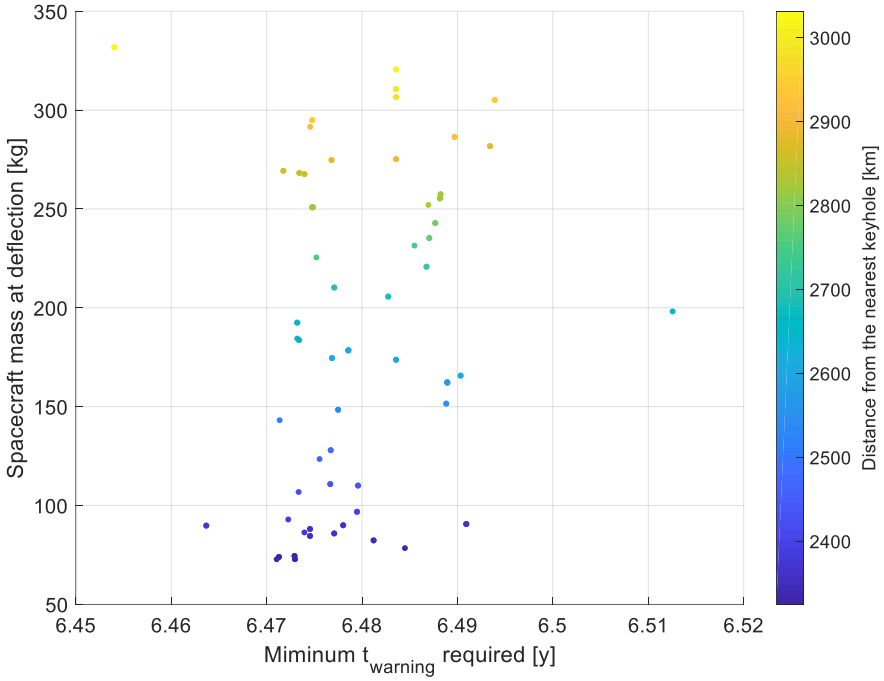

Figure 4.13: Correlation between the spacecraft mass at the deflection point and the warning time required for the deflection mission.

From Figure 4.10 it can be seen how the most effective strategy for the deflection aimed at maximising the distance from the nearest keyhole corresponds to a displacement along the ζ-axis in the direction of the second nearest keyhole. This result corroborates what has been stated in section 3.4, according to which most of the deviation for values of Δt in excess of the NEO's orbital period happens along the ζ-axis. It should be noted that the monotone nature of the results featured in this section depends on a multitude of parameters, which, in this case, do not allow for a deviation beyond the middle point between the two keyholes. For this reason, the outcome of the application of the maximisation of the distance from the nearest keyhole can be compared to the maximisation of the distance from the planet under the assumed conditions.

The deflection applied to the asteroid in the case of the selected optimal deflection is

$$\boldsymbol{dv_{tnh}} = \begin{Bmatrix} -1.4581 \\ -1.3736 \\ -0.0637 \end{Bmatrix} \cdot 10^{-3} \ {}^{\mathrm{m}}/_{\mathrm{s}}$$

(expressed in the tangent-normal-out-of-plane frame of the asteroid), as returned by the optimiser. It can be noted how the tangent and normal components feature the same order of magnitude despite the deviation occurs at $\mathrm{mjd2000} = 3.2807 \cdot 10^4$, around 5.4 periods of the NEO before the encounter, a sign that the more realistic mission profile cannot guarantee the optimal deviation direction based on what has been detailed in section 3.4.4. Furthermore the magnitude of the deviation is considerably lower than the one corresponding to

the optimal deflection of the same asteroid in section 4.2.1, which is to be expected considering the difference in the value of Δt, as is apparent in Figure 4.6.

5 Conclusions

In this thesis, the theory behind the b-plane has been presented in detail, as derived by Tisserand [24], Öpik [26] and Valsecchi et al. [19]. A numerical technique to compute the b-plane keyholes was then introduced and applied to the case of an elliptical Earth orbit and non-coincident position of a NEO with the planet's.

The deflection problem was modelled through the use of proximal motion equations and Gauss' planetary equations, providing a convenient analytical maximisation technique, following what had already been done by Vasile and Colombo [22]. The maximisation technique was then extended to the impact parameter and the single axes of the b-plane and an analytical correlation between the deflection velocity vector and the displacement on the b-plane was presented. The correlation between the deflection and the resulting displacement along the ζ-axis of the b-plane was employed to define an optimisation strategy aimed at avoiding the keyholes, thus reducing the probability of a resonant return of the NEO to the Earth.

These tools have later been applied in the case of the optimal deflection of asteroid 2010 RF_{12} aimed at avoiding the keyhole positions and for the preliminary design of a mission aimed at providing the optimal deflection of the aforementioned NEO considering the limitations imposed by a possible deflection mission. It has been found that the deflection, if performed sufficiently in advance (see section 3.4), is most effective if aligned with the direction tangent to the asteroid velocity and results in a displacement on the b-plane predominantly in the direction of the ζ-axis (corresponding to a variation in the close-encounter phasing). This result has been used to define the optimal deflection strategy aimed at avoiding a future resonant return, which has proven effective in the ideal, unbounded case (see section 4.2.1) and viable in the preliminary mission design (see section 4.3). Indeed the displacement obtained along the ζ-axis in the realistic case would be sufficient to avoid a keyhole in the case the nominal encounter coordinates on the b-plane were near it.

It should be noted that a two-body approach has been considered to model the gravitational effects for the scope of this thesis, as stated throughout the present report. Such an approximation poses an obvious limitation to the validity of the obtained results, especially when considering a long-term propagation of the predicted effects. This approach was necessary in order to obtain some of the closed-form solutions presented in this paper, such as the aforementioned optimisation techniques and the exact return in the case of an encounter taking place in a keyhole. Nevertheless, the presented results retain their general validity, as discussed in the respective results sections, and can serve as a starting point from which to start analysing a real close approach situation, comparing the obtained results with a more accurate propagation technique. Another important limitation affecting the correlation between the results presented in this thesis and the real parameters of the encounters between asteroids and our planet concerns the reliability of our knowledge of the orbital parameters of the

NEOs. These are in fact hard to determine through telescope observation and more accurate measurements are only possible when they get closer to the Earth.

To tie to one of the limitations of the presented formulation of the problem, future developments of this work could feature the development of a numerical approach to precisely determine the shape and position of keyholes in the case of an n-body propagation. A second possible addition to this thesis could be represented by the propagation of a set of initial conditions instead of a single set of coordinates to account for the probability factor associated with the determination of an asteroid's orbital parameters. Furthermore, the definition of a more comprehensive strategy to determine the optimal deviation on the b-plane could be developed, possibly taking into consideration the timing of the expected returns associated to each keyhole, as well as the cost of each of the manoeuvres required to safely avoid them. Lastly, the modelling of the impact between the spacecraft and the NEO could be improved by considering the uncertainty due to the lack of precise knowledge about its shape, rotation and composition, giving rise to a breadth of possible resulting deviations.

Bibliography

[1] "NASA CNEOS - NEO Basics," [Online]. Available: https://cneos.jpl.nasa.gov/about/basics.html. [Accessed 6 July 2018].

[2] "ESA - History of Cometary Missions," [Online]. Available: http://www.esa.int/Our_Activities/Space_Science/Rosetta/History_of_cometary_missions. [Accessed 6 July 2018].

[3] "NASA JPL - Discovery Statistics," [Online]. Available: https://cneos.jpl.nasa.gov/stats/totals.html. [Accessed 6 July 2018].

[4] C. R. Chapman and D. Morrison, "Impacts on the Earth by asteroids and comets: assessing the hazard," *Nature,* vol. 327, no. 6458, pp. 33-40, 1994.

[5] "NEODyS-2 - 2010RF12 - Close Approaches," [Online]. Available: http://newton.dm.unipi.it/neodys/index.php?pc=1.1.8&n=2010RF12. [Accessed 8 July 2018].

[6] "ESA Cosmos - Space Mission Planning Advisory Group," [Online]. Available: https://www.cosmos.esa.int/web/smpag. [Accessed 6 July 2018].

[7] F. Letizia, C. Colombo, J. P. J. P. Van den Eynde and R. Jehn, "b-Plane Visualisation Tool for Uncertainty Evaluation," vol. 16, no. 438, 2016.

[8] C. Colombo, "Optimal trajectory design for interception and deflection of Near Earth Objects, PhD Thesis," Glasgow Theses Service, 2010.

[9] "UN Office for Outer Space Affairs - Treaty on Principles Governing the Activities of States in the Exploration and Use of Outer Space, including the Moon and Other Celestial Bodies," [Online]. Available: http://www.unoosa.org/oosa/en/ourwork/spacelaw/treaties/introouterspacetreaty.html. [Accessed 6 July 2018].

[10] J. P. Sanchez, C. Colombo, M. Vasile and G. Radice, "Multicriteria comparison among several mitigation strategies for dangerous near-Earth objects," *Journal of Guidance, Control, and Dynamics,* vol. 32, no. 1, pp. 121-142, 2009.

[11] M. Vetrisano, C. Colombo and M. Vasile, "Asteroid rotation and orbit control via laser ablation," *Advances in Space Research,* vol. 57, pp. 1762-1782, 2016.

[12] C. Bombardelli, H. Urrutxua, M. Merino, J. Pelaez and E. Ahedo, "The ion beam shepherd: A new concept for asteroid deflection," *Journal of Guidance, Control and Dynamics,* vol. 34, no. 4, pp. 1270-1272, 2011.

[13] "ESA Cosmos - SMPAG - Statement on Asteroid Orbit Deflection Demonstrations," [Online]. Available: https://www.cosmos.esa.int/web/smpag/statement-on-asteroid-orbit-deflection-demonstration. [Accessed 8 July 2018].

[14] "ESA - Asteroid Impact Deflection & Assessment Mission," [Online]. Available: http://www.esa.int/Our_Activities/Space_Engineering_Technology/Hera/Asteroid_Impact_Deflection_Assessment_mission. [Accessed 7 July 2018].

[15] "NASA Planetary Defense - DART," [Online]. Available: https://www.nasa.gov/planetarydefense/dart. [Accessed 7 July 2018].

[16] I. Carnelli, A. Gàlvez and D. Izzo, "Don Quijote: a NEO deflection precursor mission," ESA.

[17] A. Carusi, G. B. Valsecchi and R. Greenberg, "Planetary close encounters: Geometry of approach and post-encounter orbital parameters," *Celestial Mechanics and Dynamical Astronomy,* no. 49, pp. 111-131, 1990.

[18] R. H. Battin, An Introduction to the Mathematics and Methods of Astrodynamics, Revised Edition, AIAA, 1999.

[19] G. B. Valsecchi, A. Milani, G. F. Gronchi and S. R. Chesley, "Resonant returns to close approaches: Analytical theory," *Astronomy & Astrophysics,* pp. 1179-1196, 2003.

[20] A. Milani, S. R. Chesley, P. W. Chodas and G. B. Valsecchi, "Asteroid Close Approaches: Analysis and Potential Impact Detection".

[21] A. Bourdoux, "Characterization and hazard mitigation of resonant returning Near Earth Objects," ESA, 2005.

[22] M. Vasile and C. Colombo, "Optimal Impact Strategies for Asteroid Deflection," vol. 31, no. 4, 2008.

[23] H. D. Curtis, Orbital Mechanics for Engineering Students, Elsevier, 2014.

[24] F. F. Tisserand, Traité de mécanique céleste, Paris: Gauthier-Villars et fils, 1889-1896.

[25] D. Menzio and C. Colombo, "The Combined Lambert-Tisserand Method Applied to the Single Flyby Problem," in *68th International Astronautical Congress*, Adelaide, Australia, 2016.

[26] E. J. Öpik, Interplanetary Encounters, New York: Elsevier, 1976.

[27] F. Letizia, J. Van den Eynde and C. Colombo, "SNAPPshot ESA planetary protection compliance verification software, Final report," 2016.

[28] M. Ross, S.-Y. Park and S. D. V. Porter, "Gravitational Effects of Earth in Optimizing ΔV for Deflecting Earth-Crossing Asteroids," vol. 38, no. 5, 2001.

[29] G. B. Valsecchi, E. M. Alessi and A. Rossi, "An analytical solution for the swing-by problem," no. 123, pp. 151-166, 2015.

[30] "NASA - JPL - NAIF - SPICE," [Online]. Available: https://naif.jpl.nasa.gov/naif/toolkit.html. [Accessed 9 July 2018].

[31] C. Colombo, M. Albano, R. Bertacin, M. M. Castronuovo, A. Gabrielli, E. Perozzi, G. Valsecchi and E. Vellutini, "Mission analysis for two potential asteroids threat scenarios: optimal impact strategies and thechnology evaluation," in *68th International Astronautical Congress*, Adelaide, Australia, 2017.

[32] M. Romano, C. Colombo and J. M. Sánchez Pérez, "Efficient Planetary Protection Analysis for Interplanetary Missions," in *68th International Astronautical Congress*, Adelaide, Australia, 2018.

[33] B. A. Conway, "Near-Optimal Deflection of Earth-Approaching Asteroids," vol. 24, no. 5, 2001.

[34] A. Carusi, G. B. Valsecchi, G. D'Abramo and A. Boattini, "Deflecting NEOs in Route of Collision with the Earth," no. 159, pp. 417-422, 2002.

[35] A. Carusi, G. D'Abramo and G. B. Valsecchi, "Orbital and mission planning contraints for the deflection of NEOs impacting on Earth," no. 194, pp. 450-462, 2008.

[36] R. Kahle, G. Hahn and E. Kührt, "Optimal deflection of NEOs en route of collision with the Earth," no. 182, pp. 482-488, 2006.

[37] J. P. Sanchez and C. Colombo, "Impact Hazard Protection Efficiency by a Small Kinetic Impactor," vol. 50, no. 2, 2013.

[38] G. Vardaxis and B. Wie, "Near-Earth object intercept trajectory design for planetary defense," no. 101, pp. 1-15, 2014.

[39] G. Vardaxis and B. Wie, "Impact Risk Assessment of a Fragmented Asteroid in Earth Resonant Orbits," no. 4300, 2014.

[40] D. Yeomans, S. Bhaskaran, S. Chesley, P. Chodas, D. Grebow, D. Landau, S. Petropoulos and J. Sims, "Report on Asteroid 2011 AG5 Hazard Assessment and Contingency Planning," 2012.

[41] D. K. Yeomans, S. Bhaskaran, S. B. Broschart, S. R. Chesley, P. W. Chodas, T. H. Sweetser and R. Schweickart, "Deflecting a Hazardous Near-Earth Object," in *1st IAA Planetary Defense Conference*, Granada, Spain, 2009.

[42] "ESA - Near-Earth Objects - NEO Segment," [Online]. Available: https://www.esa.int/Our_Activities/Operations/Space_Situational_Awareness/Near-Earth_Objects_-_NEO_Segment. [Accessed 6 July 2018].

[43] R. Greenberg, J. F. Wacker, W. K. Hartmann and C. R. Chapman, "Planetesimals to planets: Numerical simulation of collisional evolution," *Icarus,* vol. 35, no. 1, pp. 1-26, 1978.

[44] C. Bombardelli and G. Baù, "Accurate analytical approximation of asteroid deflection with constant tangential thrust," *Celestial Mechanics and Dynamical Astronomy,* no. 114, pp. 279-295, 2012.